Johannes Gutenberg University Mainz

Master Thesis

Construction of a test setup and characterisation of wavelength shifting fibres and opaque scintillator properties for NuDoubt^{++}

presented to
the department of Physics, Mathematics and Computer science (FB08)

Author:
Miriam Weigand

Reviewers:
Prof. Dr. Alfons Weber
Dr. Stefan Schoppmann

07.01.2026

Abstract

The *NuDoubt*$^{++}$ experiment is planning to use Optimised Wavelength-shifting (OWL) fibres in combination with slow-hybrid, opaque liquid scintillator technology to perform ultra-low noise measurements on one of the rarest decays: double beta plus decays. As the name suggests, OWLs are specialised WLS (wavelength-shifting) fibres that have been recently developed. In contradiction to commercial WLS fibres, the WLS molecules are deployed solely to the exterior of the fibre, as this configuration is anticipated to optimise the fibre's capture efficiency. The purpose of this thesis is the characterisation of OWL fibres in opaque liquid scintillator. As the research progressed, the fibre concept was refined to encompass the so-called 'Bubo fibres'. The term signifies the configuration of an OWL within a hollow tube.

The present study employed a table-top light yield backscatter setup to facilitate a comparative analysis between Bubo prototypes and commercially available wavelength-shifting fibres. This investigation was conducted utilising transparent and opaque liquid scintillators. In a relative comparison, one Bubo candidate demonstrated superior performance in comparison to commercial fibres.

Furthermore, Geant4 Simulations of OWL fibre, in addition to the setup, were executed to test different material combinations and to confirm the measurement results.

Acknowledgment

First of all I want to thank Alfons Weber for offering me this Master project and inviting me into his group. Further a great thanks to Stefan Schoppmann for the supervision and his careful leadership of the *NuDoubt*$^{++}$ collaboration. Within the *NuDoubt*$^{++}$ collaboration I am grateful for the warm welcome and nice company.
Quirin Weitzel, Fabian Piermaier and Steffen Schönfelder from the PRISMA Detector Lab I want to thank for hosting the experiment in their labs, material providence, custom made 3D prints as well as an open ear and good suggestions. Bastian Kessler I wish to thank for sharing his expertise on wavelength shifting fibres and OWLs with me as well as for the production of the OWL fibres. Further I want to appreciate that Lea Schlickmann helped me glueing in the PMTs in an older version of the setup.
After about three/quarters of this projects' time, it became eminent that a few changes in the setup and the data readout were required and I wish to comment on the generosity of the AG Wurm and Dorina Zundel for borrowing equipment and providing an alternative location for the experiment. Dorina Zundel further deserves a huge thank you for spending quite some time in the lab with me, helping by the down tracking of noise sources and calibrations. Her clear vision, decisiveness, and generous offers of help were of great use for me.
I enjoyed my time with all the members of the AG Weber group, especially I want to thank Ioana Caracas for the nice and quiet time we shared in the office and Asa Nehm for caring advise.
Last but not least I want to thank my family and friends for their support, fun activities. Last thanks goes to my parents for financing my university degrees and living costs.

Acronyms

APD Avalanche photodiode.

Bis-MSB 4-Bis-(2-methyl-styryl)-benzene.

BPEA 9,10-Bis(phenylethynyl)anthracene.

DIN Di-isopropylnaphthalene.

LAB Linear alkyl benzene.

NoWaSH New opaque wax scintillator, Heidelberg.

OWL Optimised Wavelength-shifting Fibre.

PEMA Poly(ethyl methacrylate).

PMMA Poly(methyl methacrylate).

PMT Photomultiplier tube.

PPO 2,5-Diphenyloxazole.

PTFE Polytetrafluoroethylene.

QT Quartz tube.

SiPM Silicon photomultiplier.

TIR Total internal reflection.

WLS Wavelength shifting / wavelength shifter.

Contents

Chapter 1

Introduction

NuDoubt^{++} (**Neu**trino **Dou**ble **be**ta **plus plus**) is a planned experiment dedicated to the study of double beta plus decays [1]. Two of the three decay modes predicted by the Standard Model involve positron emission and, to date, have not been experimentally observed. As *NuDoubt*$^{++}$ will be sensitive to these modes, the objective is to detect these rare processes, which have an expected lifetime of over 10^{26} years.
Another goal is to make advances in the search for neutrinoless double beta decays. Such decays would provide the most sensitive means of probing the Dirac or Majorana nature of neutrinos [2],[3]. Observing this process would verify the Majorana nature of neutrinos, provide access to the absolute neutrino mass scale, and confirm lepton-number violation [4].

In response to the challenges posed by the rarity of these processes, the *NuDoubt*$^{++}$ collaboration proposed an innovative detector concept combining two novel liquid scintillator techniques. Firstly, hybrid-slow scintillators to discriminate the Cherenkov-to-scintillation light ratio [5],[6]. Secondly, opaque scintillators to provide event topology information at a sub-centimetre scale [7]. This dual approach enhances the capabilities of background suppression. Isotope loading of this combined liquid scintillator enables a significant quantity of a double-beta decaying isotope to be deposited directly inside the detector with minimal impact on the scintillation output and therefore no significant effect on the energy resolution. The extraction of light will be facilitated by a dense grid of optimised wavelength-shifting fibres, which will be introduced into the detector volume.

The central objective of this thesis is to verify and test light collection with OWL fibres in opaque liquid scintillator (LS). As the course of this thesis progressed, the concept of OWLs was advanced to the so-called Bubo fibres (see section 4.2). A tabletop backscatter light yield setup was designed and utilised to conduct a relative light yield measurement between commercial Y11 fibres from Kuraray and Bubo prototypes. A Geant4 simulation was utilised to assess the efficacy of various OWL types. An additional simulation was conducted, emulating the table-top experiment, thereby facilitating the cross-checking of the measured results.

The structure of this thesis is as follows: The chapter 2, entitled 'Theoretical Background', commences with an examination of the fundamental principles of scintillation, followed by a discussion of both inorganic and organic liquid scintillators. Novel approaches in the field of organic LS are put forward. The working principle and features of PMTs and SiPMs are reviewed. The discussion commences with a comprehensive examination of wavelength-shifting optical fibres, followed by a concise review of gamma spectroscopy. The chapter 3, entitled "NuDoubt^{++}" is dedicated to the *NuDoubt*$^{++}$ experiment and the process of double beta decay. The configuration of the table-top backscatter light yield setup is addressed in chapter 4. In chapter 5, the LS-fibre detector and scintillators employed in the measurements are examined. In addition, the triggering, event filtering, and the results are presented. In chapter 6, the two Geant4 simulations are presented and discussed.

Chapter 2

Theoretical Background

In this chapter the theoretical background relevant to this master thesis is presented. Further materials and concepts of relevance are introduced.

The following sections are inspired by [8].

2.1 Working Principle of Scintillators

The key point of scintillation is the conversion of kinetic energy of an incident particle into detectable light. The amount of produced scintillation light is in good approximation linear to the kinetic energy, allowing the reconstruction of the deposited energy.

High energetic initial particles traversing the scintillation material ionize or excite the molecules along their path and lose parts of their kinetic energy. This process happens directly for charged incident particles and indirectly. In the indirect case the ionization process is realized through energy transfer to a charged particle inside the material, for electrically neutral particles such as gammas.

Scintillation light is emitted when the ionized or excited molecules return into their ground state and can be understood as luminescence. Luminescence can be subdivided into the processes of fluorescence and phosphorescence by the means of the life time of the excited states and the type of electronic transition.

In the simplest model of a scintillator, the scintillation light creating decay of an excited electron state is given by a double exponential relation [9]:

$$N(t) = A_f exp(-\frac{t}{\tau_f}) + A_s exp(-\frac{t}{\tau_s}), \tag{2.1}$$

where N is the number of emitted photons per time t. The time constants τ_f and τ_s represent the fast component, mostly related to the prompt fluorescence and the slow component, attributed to the delayed fluorescence and phosphorescence. The weight factor of each component is given by A_f and A_s, generally the fast component weighs more, but the numbers are material specific. The overall pulse shape of an event is determined by the time components and by the weight factors. In practice, depending on the scintillator composition, more than two exponential functions might be needed.

An important characteristic of scintillators is the Light yield, defined as:

$$Light\ Yield = \frac{\#\ scintillation\ photons}{deposited\ energy}\ . \tag{2.2}$$

In an ideal case, where self interaction between excited or ionized molecules can be neglected, the number of photons emitted in the scintillating material is proportional to the energy of the incident particle. But in reality, there are various forms of (energy-dependent) loss in deposited energy, referred to as quenching, that decrease the fluorescence. For example, in the context of liquid scintillators, ionization quenching, i.e.

the energy loss via non-radiating de-excitation after self interactions between excited or ionized molecules, plays the biggest role. This effect depends on the density of ionised particles and is stronger if the energy loss per path length dE/dx of the incident particle is large. Further absorbed oxygen decreases the light output.

The light yield per path length dL/dx as a function of dE/dx caused by ionization quenching is given by Birks' law [10]:

$$\frac{dL}{dx} = S\frac{\frac{dE}{dx}}{1 + k_B\frac{dE}{dx}} \ , \tag{2.3}$$

with S being the light yield constant and k_B denoting a material dependent quenching parameter.

Furthermore, the light is attenuated via absorption or scattering as it traverses the scintillator material. The intensity I of a one-dimensional light beam decreases as a function of the optical path length x exponentially with the attenuation length Λ:

$$I(x) = I_0 \cdot exp(\frac{x}{\Lambda}) \ . \tag{2.4}$$

The Absorbance $A(x)$ is defined via:

$$A(x) = Log_{10}(\frac{I(0)}{I(x)}) \tag{2.5}$$

and can be simplified to the Bouguer–Beer–Lambert law

$$A(x) = \epsilon c x \ , \tag{2.6}$$

relating the absorption to the attenuation coefficient ϵ and the concentration c [11]. Generally, the attenuation length is wavelength dependent and can be decomposed into a sum of absorption length Λ_{abs} and scattering length Λ_{scat}:

$$\frac{1}{\Lambda} = \frac{1}{\Lambda_{abs}} + \frac{1}{\Lambda_{scat}} \tag{2.7}$$

Since the absorbance of a multi-component medium can be calculated by summing over all i absorbance contributions from individual components, we can calculate the total attenuation length via:

$$\frac{1}{\Lambda_{tot}} = \sum \frac{1}{\Lambda_i} \tag{2.8}$$

As the deposited energy per unit length dE/dx depends on the type of ionizing radiation traversing the scintillator material, the time components and weight factor, the pulse shape is characteristic for each type of incident particle. Therefore, one can use the method of pulse shape discrimination to differentiate between particle types.

Over the years, multiple types of scintillators were developed: inorganic and organic crystals, plastic scintillators, inorganic and organic liquids and gaseous scintillators. All have their own benefits and challenges.

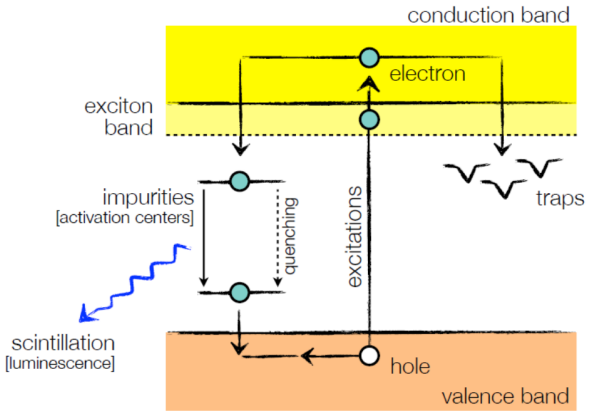

Figure 2.1: Band structure of an inorganic scintillation crystal with an activator site. Figure illustrates the excitation of a electron-hole pair and further the process of luminescence photon emission, quenching and trapping. Adapted from [12].

Keypoints on the wish list for a good scintillation material are:

- high light yields
- linearity between produced photons to deposited energy over a wide spectral range
- good energy resolution
- the majority of the light coming from luminescence rather then phosphorescence
- short decay times for a fast time response
- good time resolution
- optical transparency to the wavelength of own emission, in order to minimize reabsorption losses
- emission wavelength matching the sensitive wavelength of the used photodetector

But some materials are also more prone to problems due to ageing, radiation damage, hygroscopy, scaleability issues and rentability production costs.

2.2 Inorganic Crystal Scintillators

The scintillation property of inorganic crystal scintillator comes from the energy states determined by lattice structure of the crystal. In the simplest model of a crystal, the electron orbits of the individual orbits overlap due to the closure of the atoms in the lattice, resulting in an energy band structure. The electrons are only allowed to exist within that band, the regions in between are forbidden. All electronic transitions happen between the highest occupied band - the valence band - and the lowest empty band - the conduction band. Between the valence and the conduction band is a material and crystal structure specific energy gap E_g, that is usually around 3-4 keV, high enough that at room temperatures nearly no transitions occur. When an electron is excited to the Valence band, a vacancy - a so-called hole - is created in the valence bands. Holes are the

charge carriers of the valence band. Within a band, electrons or holes are free to move around without a change in energy. The recombination of electron-hole pairs is the source of light creation in a crystal lattice.

Some crystals are intrinsic scintillators, i.e. the luminescence is produced by a part of the crystal lattice itself. Those materials are called self-scintillating. But in most scintillating crystals, the scintillation capability arises from lattice defects. In this case activator ions - typically thallium (Tl) or cerium (Ce) - are introduced into the lattice structure. They create so-called activation or luminous sites in the lattice, where the band structure is modified in a way that more energy levels within the band gap appear. Being closer together they enhance the chance of recombination. One typically chooses activation ions, that modify the band structure in such a way, that the recombination photon is in the range of visible light. Further, the modified band structure improves the transparency of the crystal towards those recombination photons.

The scintillation process in an inorganic crystal happens as followed: A charged initial particle will create a large number of electron-hole pairs by exciting electrons to the conduction band. As shown in figure 2.1 those pairs then migrate towards activation sides to recombine - either via emission of a photon or via radiation-less transfer. The first process is called luminescence, the second is refereed to as quenching. Both processes happen at fast time scaler in order of ns. Other lattice defects can act as traps, from which the electron can't easily de-excite. Those traps lead to delayed phosphorescence with time scales ranging from ms to s.

The crystal materials, as well as the choice of activation ions, effect the emission spectra as well as the time components. This happens as higher temperatures excite more lattice vibrations (phonons) that lower the light yield, called thermal quenching.

Usually, the crystals contain elements with high atomic number Z and have high densities, which makes them superior in gamma spectroscopy. Further, most anorganic scintillator crystals feature desirable properties like high light yield (several 10000 photons per MeV) and excellent energy resolution. Some Crystals also exhibit sub-μs decay times. Challenging is the growth of the crystal, which is costly and limits the affordable size. Further they can be very prone for hygroscpoy and their response is temperature dependent.

2.3 Organic Liquid Scintillators (LS)

Energy Levels and Excitation of Organic Scintillators

In organic scintillators the benzene ring structures, referred to as phenyl groups, exhibit unique electron structures that allow for scintillation - independent of the physical phase the material is in.

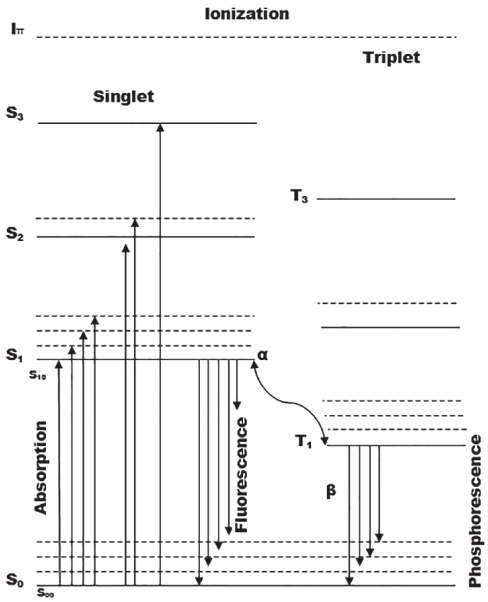

Figure 2.3: Typical energy level scheme of a π-electron in an organic molecule. Adapted from [14].

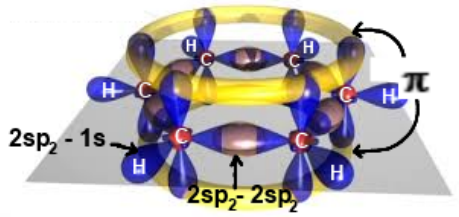

Figure 2.2: Orbital structure of a benzene ring. The sp^2 hybridized orbitals are shown in blue, the delocalized pi-orbital rings in yellow. The gray plane indicates the plane of the carbon atom ring. Taken from [13].

The electron orbitals of the carbon atoms in the ring undergo orbital sp^2 hybridization, creating three hybrid σ-orbitals orientated at 120° in a plane and a π-orbital perpendicular to the ring plane. The π-orbitals of neighbouring carbon atoms overlap, creating delocalized ring orbitals above and below the ring plane. A sketch of the benzene ring's orbital structure can be found in figure 2.2

The energy level structure of a π-electron consists of electronic singlet and triplet states, each containing several vibrational sub-states. A typical energy level structure is displayed in figure 2.3. According to the Franck-Condon principle, the excitation of a π-electron happens from the vibrational ground state of the electronic ground state into an excited vibrational state of an excited electronic state.The de-excitation of vibrational states happens internally without radiation at fast time scales of $\mathcal{O}(10^{-12}$ to $10^{-11})$ s. The de-excitation of electronic singlet states is called fluorescence and happens after a few to tens of nanoseconds. A direct decay from an excited triplet state into the ground singlet state is highly spin forbidden. Therefore the decay happens at longer time scales of O(104) s or larger and is referred to as phosphorescence. Other mechanisms of Triplet de-excitation are triplet-triplet annihilation, leading to delayed fluorescence, and the non-radiative internal conversion.

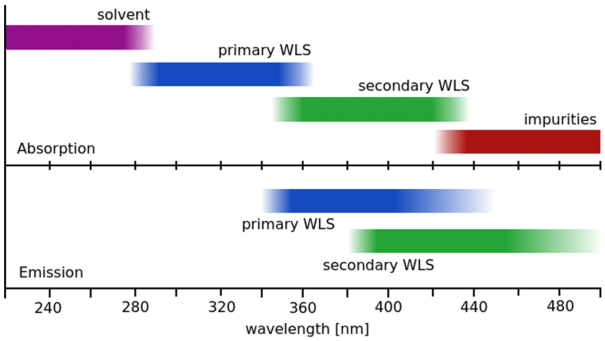

Figure 2.4: Typical arrangement of absorption and emission regions in a liquid scintillator consisting of a solvent and a wavelength shifter. Reprinted from [15]

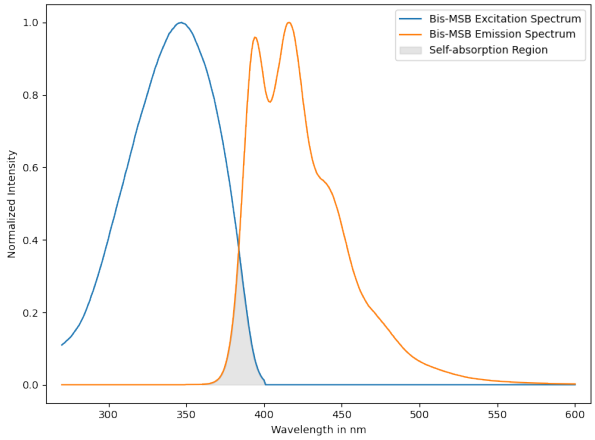

Figure 2.5: Absorption and Emission spectrum of the WLS Bis-MSB. One can clearly see the Stocks shift between both spectra. Both spectra overlap in the grey shaded area. In this wavelength region reabsorption can happen.

Composition of Liquid Scintillators

Liquid scintillators usually consist of one or more solvents with the addition of a primary and eventually a secondary flour. The words flour and wavelength shifter (WLS) are used interchangeably in literature.

The base solvent is often a scintillator itself. The emission spectrum is shifted to longer wavelengths with respect to the absorption spectrum, this phenomenon is called Stokes shift. But since the emission and absorption spectra still overlap, self-absorption can happen and the solvent is not transparent enough to its own scintillation light. An example spectrum of a scintillating Material is shown in figure 2.5.

To address the issue of self absorption, a so-called primary flour is added to the solvent in low concentrations of $\mathcal{O}(5g/l)$. The flour itself is scintillating with an emission spectrum located at longer wavelength than the solvent's absorption spectrum. The solvent transfers most of its energy to the fluor via the radiationless Förster resonance energy transfer effect [8]. The better the solvents emission spectrum overlaps the WLS emission spectrum, the more efficient the energy transfer is. This can be quantised by the spectral overlap integral J, calculated as

$$J = \frac{\int f_d(\lambda)\epsilon_a(\lambda)\lambda^4 \, d\lambda}{\int f_d(\lambda) \, d\lambda} \, , \tag{2.9}$$

Molecule	Formula	Density	Flash Point	max. absorption	max. emission
DIN	$C_{16}H_{20}$	0.96 kg/l	$>$ 140°C	279 nm	338 nm
LAB	$C_{6+n}H_{6+2n}$	0.85 kg/L	$\sim$ 140°C	260 nm	284 nm
PPO	$C_{15}H_{11}NO$	-	-	303 nm	358 nm
PTerphenyl	$C_{18}H_{14}$	-	-	276 nm	338 nm
BPEA	$C_{30}H_{18}$	-	-	310 nm	468 nm
Bis-MSB	$C_{24}H_{22}$	-	-	335 nm	418 nm

Table 2.1: Molecular formula, density, and flash point, as well as the wavelengths of the optical absorption and emission peak of typically used solvents (DIN & LAB), primary (PPO & PTerphenyl) and secondary (BPEA & Bis-MSB) fluors diluted in cyclohexane. Modified from [9].

where f_d is the donators (here solvents) emission spectrum and ϵ_a the acceptors (here WLS's) molar extinction coefficient. The florescence quantum yield of any Material is given by

$$Q = \frac{\#\ absorbed\ photons}{\#\ emitted\ photons} \tag{2.10}$$

and for WLS, it is usually a value close to 1. Hence the flour converts nearly all the obtained energy into detectable light at longer wavelength. As the flour is used in small concentrations, self-absorption has less of an effect and the emitted photons can traverse meters of detector material without being attenuated.

If even more transparency is required, one can shift the wavelength even further by adding a secondary flour at even lower concentrations of 10^{-1} to $10^{-3} g/l$). The absorption spectrum of the secondary fluor has to match the emission spectrum of the primary fluor for sufficient energy transfer.

A typical arrangement of absorption and emission spectra of a multi-component liquid scintillator can be found in table 2.4. A selection of commonly used solvents and flour as well as some of their chemical and physical properties is displayed in figure 2.1.

For the creation of a safety consideration matching scintillator, linear alkyl benzene (LAB) or di-isopropylnaphthalene (DIN) are a common option, since both exhibit high flash points as well as good material compatibility (e.g. with acrylic vessel). 2,5-diphenyloxazole (PPO) and 1,4-diphenyl-benzol (p-terphenyl) are examples for commonly used primary flours. As typical secondary flours 4-bis-(2-methyl-styryl)-benzene (Bis-MSB) as well as 9,10-Bis(phenylethynyl)anthracene (BPEA) can be mentioned.

Overall the solvent and the flours act as unit, the absorption spectrum is given to first order by the solvent, the emission spectrum equals in good approximation that of the latest flour. Another motivation to use flours is to maximise the overlap between the LS emission spectrum and the spectral detection efficiency spectrum of the used photon counter.

To finish this chapter about organic LS, lets look at their properties: Advantageous properties of organic LS are their fast time constants, small temperature dependence. Compared to inorganic Crystals, they feature smaller but sufficiently high light yields, allowing decent energy resolution. Further their response is less temperature dependent. LS feature volume flexibility, are scaleable and comparably cheap to produce.

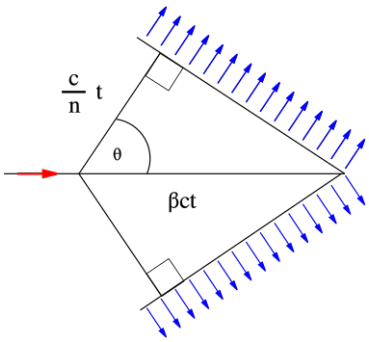

Figure 2.6: Diagram illustrating the formation of the Cherenkov cone, with an opening angle θ, as a charged particle (red arrow) above the Cherenkov threshold moves through a dielectric medium. Taken from [16].

2.4 Cherenkov Light

If the speed of the charged incident particle exceeds the speed of light in a dielectric material c', Cherenkov light is emitted as a consequence of the electromagnetic shock wave induced by the particle's motion. Cherenkov light is emitted coherently and is directed in a cone along the particles path as displayed in Figure 2.6. The opening angle θ of the Cherenkov cone depends on the velocity v of the incident particle as well as the refractive index n of the material:

$$cos(\theta_C) = \frac{c'}{v} = \frac{1}{n\beta} \ , \tag{2.11}$$

where $\beta = v/c$ and $c' = c/n$. As the possibility of Cherenkov light emission is coupled to the exceedance of the speed of light in the material, a lower energy threshold can be defined. This so-called Cherenkov threshold is given by

$$E_C = \frac{mc^2}{\sqrt{1 - 1/n^2}} \tag{2.12}$$

and depends only on the mass m of the particle and the mediums refractive index n.
The Cherenkov light typically contributes by a few percent to the total light yield within scintillating materials. In high-frequency regions, a part of the Cherenkov light is absorbed by the scintillator material and remitted as isotropic scintillation light at lower frequencies. The directed component then is lost.

2.5 Novel Approaches to Organic LS

In the following, three novel concepts to enhance the performance of organic LS detectors are presented.

2.5.1 Hybrid-Slow LS

The key feature of hybrid LS is to allow the separation of the Cherenkov component from the scintillation component in the collected light. The Cherenkov signal can be used to reconstruct the direction of the incident particle and to obtain topological information about the event. On the other hand, the high light yield of the scintillation

signal leads to good energy resolution and allows a low energy threshold. To separate the two components, the fact that the Cherenkov signal arises faster than the scintillation signal is usually exploited. The ratio of the Cherenkov signal to the scintillation signal ($\frac{C}{S} - ratio$) can be used to discriminate the shape of the pulse and identify the type of particle. This particle identification can be used for background suppression. A simple approach to improve the ability to temporally separate the fast Cherenkov signal from the slightly slower scintillation signal is to deliberately delay the scintillation signal by 10 ns or more, making it slower. It has been shown by [5] that a bi-solvent scintillator consisting of an LAB-based LS with purified DIN added in concentrations of 5-20 % provides the desired scintillation delay. The cocktail fully maintained high light yield and pulse shape discrimination capabilities compared to regular LS, resulting in percent energy resolution and low energy thresholds, as well as efficient background suppression. In some samples the C/S separation was able to achieve parities of the Cherenkov light population of up to 91 %. A drawback is the reduced transparency of the bi-solvent LS, which limits the detector size. Furthermore, the delayed scintillation light reduces the peak resolution, especially for low energy events.

2.5.2 Opaque LS

The idea behind opaque scintillators is to deliberately reduce the scattering length of the LS to 1-2 cm, thereby locally trapping the produced photons close to their point of emission. A dense grid of optical fibres is then distributed throughout the detector, collecting the trapped light and directing it to one of the silicon photomultipliers (SiPMs) connected to each fibre end. This method provides higher spatial resolution than conventional LS without significant loss of the overall scintillation signal [17]. This increases the ability to identify particles as the event topology is better resolved. It also reduces the demands on the absorption properties of the LS, since the photons are not required to travel far.
To make an opaque LS, paraffin is mixed into a regular LS. An example of an opaque LS is NoWaSH (**N**new **o**paque **W**ax **S**cintillator, **H**eidelberg), a three-component system containing LAB as the base solvent, a certain percentage of paraffin wax and PPO as the fluorophore. At room temperature, mixtures with wax concentrations of 10% or more are highly viscous, opaque and have improved chemical and optical stability.
In addition, opaque LS are well suited to high metal loading, as the reduction in absorption length due to the metal is not relevant as long as it is less than the scattering length of the opaque material.

2.5.3 Scintillator Loading

Loading is a term used to describe the introduction of certain metals or other isotopes into the LS material. The loaded material can enhance the cross section between certain particle types and the scintillator, yielding better detection capabilities. For example, adding Gadolinium into the scintillator increases the neutron capture efficiency drastically. If one wants to detect the radioactive decay of certain isotope, it is also possible to directly dissolve the isotope into a liquid scintillator.
One technique to dissolve a sufficient amount of isotopes of novel gases in liquid scintillator is to apply pressure [18]. According to Henry's law, the ratio between applied pressure p and the concentration of dissolved gas particles in the liquid C is a constant:

$$const = \frac{p}{C} \ . \tag{2.13}$$

Hence, increased pressure leads to a higher dissolved isotope concentration. Loading the isotope in high concentrations directly into the LS minimises all losses between target isotope and detector and increments the observed decay rates.

2.6 Light Detection

The detection of a few or even single photons and the corresponding creation of usable current signals is a specific challenge. In astro and particle physics the use of Photomultiplier tubes (Photomultiplier tube (PMT)) and SiPMs have become a common choice.

This section serves the explanation of the working principle and presentation of key features of both PMTs and SiPMs.

Base for the subchapters were the PMT Handbook [19] and technical guide on SIPMs [20] from Hamamatsu.

2.6.1 Photomultiplier Tube (PMT)

PMTs are highly sensitive devices that have been utilised in various fields of physics since their invention in 1930 [21]. A PMT comprises a photocathode, a focusing electrode and an electron multiplier structure composed of multiple dynodes, which are sealed within a vacuum housing. A schematic representation of a PMT setup can be found in Figure 2.7. The incident photon enters the PMT through a window. The first step in the transition from photons to signals is the conversion of photons into electrons through the photoelectric effect at the photocathode. The photocathode is made of photosensitive material, often Bi-alkali metals. Emitted photoelectrons are then focused and accelerated onto the first dynode in the high voltage field of the focusing electrode. The hit on the dynode creates multiple secondary electrons that are further accelerated towards the next dynode. This process reoccurs at all following dynodes so that an amplification of a single photoelectron by a gain factor of 10^5 *to* 10^9 is achievable depending on the applied high voltage and the number of dynodes. The plurality of electrons creates a significant current signal in the anode. The PMT interior is evacuated to facilitate unobstructed electron transportation and acceleration.

PMTs are manufactured for specific wavelength ranges. The long-wavelength cutoff is set primarily by the photocathode material (and to a lesser extent its thickness), while the short-wavelength cutoff is usually determined by the optical transmission of the entrance window material. The Quantum efficiency (QE) of PMTs is defined as

$$QE = \frac{number\ of\ emitted\ photoelectrons}{number\ of\ incident\ photons} \ . \tag{2.14}$$

The quantum efficiency is usually between 20-30% within the specified wavelength regime but varies with the exact wavelength.

Further qualities of PMTs are a linear charge amplification with applied high voltage, good time resolution (typical order $\leq 200ps$) and low noise. The dark count rate - when a photoelectron leaves the cathode due to thermal excitation - is in the order of kHz at room temperature.

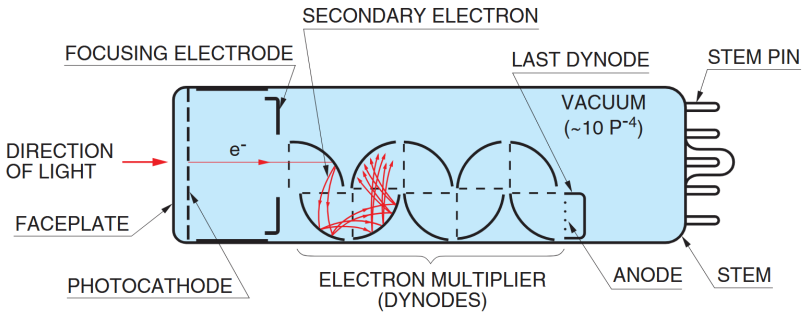

Figure 2.7: Schematic sketch of a PMT. Taken from [19].

2.6.2 Silicon Photomultipliers (SiPMs)

Silicon Photomultipliers are compact, single-photons sensitive solid state electronic devices that also reach gains in the order of 10^6. SiPMs are also known as Multi-pixel Photon Counters (MPPC). This name intuitively describes, that SiPMs are photon detectors that are made of multiple pixels. Each pixel incorporates an avalanche photodiode (APD).

To understand the operational principles of APDs, lets start with the underlying concept of a concept of a silicon-based PN photodiode:
Pure crystalline silicon is an intrinsic semiconductor characterised by a small band gap of 1.14 eV and relatively high resistance. The functionality of silicon-based PN photodiodes is attributable to the integration of a PN junction into the crystal lattice through the doping of one crystal face with electron-donating elements, typically from the fifth element group, to establish the N region, and the other with electron-accepting elements, usually from the third element group, to define the P region. The addition of an electron to the N region and a hole to the P region is demonstrated by the dopants. As the majority carrier concentration is increased in each region, the resistance drops in the doped areas. The PN junction is formed at the interface between both regions, as the excess electrons and holes recombine while the donor ions remain static in the lattice. Consequently, the N doped region becomes positively charged, while the P doped region becomes negatively charged. As demonstrated in Figure 2.8, the resultant electric field, emanating from the cathode (or N region) towards the anode (or P region), sustains the presence of electrons and holes on either side of the junction. Consequently, an empty depletion zone is formed, thereby delineating the region of charge carrier absence. This potential barrier defines a preferred conduction direction and the PN junction therefore act as diode.

The creation of an electron-hole pair within the depletion zone can be initiated by external sources of energy, such as thermal agitation or photoelectric absorption. Within the depletion zone's electric field, the charge carriers of the pair drift in opposite directions across the PN junction towards the respective outer edges where they accumulate. In the event of an electrical connection between the P and N regions, a current may flow within the loop. This current can either be a thermal dark current or a photo current. The former is characterised by its occurrence in response to thermal agitation, whereas the latter is attributed to photoelectric absorption.
Electron-hole pairs created outside the depletion region do not contribute to the current, as they have short lifetimes and recombine before reaching the depletion layer.

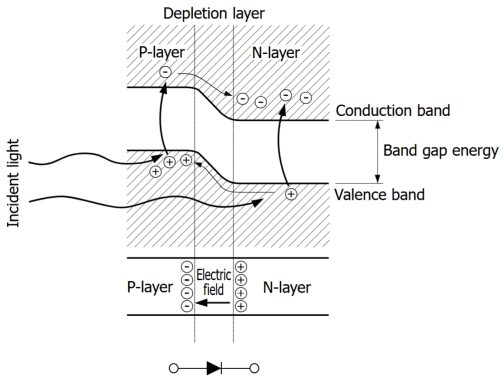

Figure 2.8: Illustration of the band structure of a PN Junction introduced into Silicon. Taken from [20].

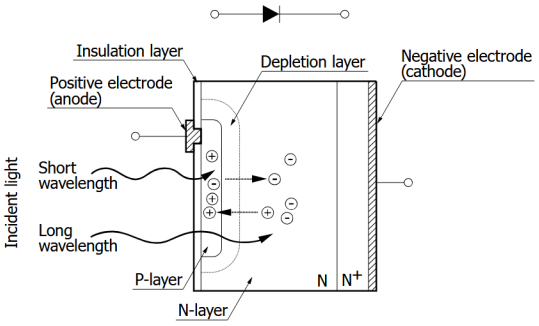

Figure 2.9: visualization of a Si PN photo diode. Photons of shorter wavelength are more likely to be absorb in the P layer, while longer wavelength radiation usually penetrated up into the n-layer. Reprinted from [20].

The depth of the depletion zone is a critical factor in determining the photosensitivity of the PN diode per wavelength. Longer wavelengths penetrate deeper into the material than shorter ones (see Figure 2.9). The presence of deeper depletion zones facilitates the detection of longer wavelengths. Enhancing the depletion layer in a given photo diode is achieved by increasing the reverse bias applied to the PN junction. In such a scenario, the cathode (N region) is at a higher electric potential in comparison to the anode (P region).

Another effect of an increased reverse bias voltage is, that the electric field over the depletion zone is strengthened, thereby intensifying the electric force on electrons and holes created in the depletion zone. This results in increased velocities and, consequently, greater kinetic energy between collisions of the carriers with the lattice. Once the average kinetic energy between collisions exceeds the band gap energy of silicon, sufficiently energetic carriers are able to ionise lattice atoms and create another electron-hole pair. It is this impact ionisation effect which is responsible for the rapid multiplication of drifting charge carriers, thus creating an avalanche. It is evident that the magnitude of the resulting current signal is increased as a consequence of the gain of charge carriers. This is the underlying concept of APDs. The gain of APDs is in theory linear, increases with the applied reverse bias voltage and diminishes with rising temperature.
The reverse bias voltage required to sustain impact ionisation, thereby ensuring the creation of an average of more than one additional carrier by each charge carrier in the depletion zone, is designated as the breakdown voltage, denoted by V_B. Should the reverse bias voltage applied exceed the APD's breakdown voltage, the diode will operate in Geiger mode. In such circumstances, the generation of an avalanche can be initiated by a single electron-hole pair. The breakdown voltage is a crucial characteristic of each APD. As the precise breakdown voltage varies between different APDs, even for the same model, the overvoltage ΔV, defined as the difference between the applied reverse bias voltage and the individual breakdown voltage, is typically the focus of discussion.

$$\Delta V = V_{applied\ bias\ voltage} - V_{BD} \ . \tag{2.15}$$

As previously mentioned, SiPMs or MPPCs are composed of hundreds to thousands of APD pixels, arranged in an array and operated in Geiger mode. The pixels are typically optically separated and connected in series over quenching resistors. The summation of all APD outputs constitutes the SiPM output. Given that the pixels under consideration are of a diminutive dimension, it is improbable that a single pixel will be struck by two photons concurrently. Consequently, their function is that of binary counters.
SiPMs are, compared to PMTs, more prone to noise. The Darkcount rate, so the rate in which thermal electrons will cause an avalanche , is slightly higher (at room temperature typically in orders of MHz). Another source of noise is optical crosstalk, whereby neighbouring pixels fire due to the optical photons released in the avalanche of a pixel. This resulted in an overestimation of photon counts and broader signal distributions. Further some carriers get trapped in lattice defects during the avalanche and create a delayed second avalanche, called after pulsing. The pixel recovery after an avalanche also leads to recharge noise.
Overall, noise rate is increasing with temperature and over voltage. But on the other hand, the detection efficiency is also known to increase with over voltage. Consequently, the over voltage level applied must be chosen with meticulous care.

2.7 Optical Fibres

In certain instances, it is necessary to collect and guide light e.g. emitted by scintillators to photon detectors placed further away outside the detector volume. In such cases, the employment of optical guides or fibres is a viable solution.
The guidance of light inside the fibres or guides relays on consequential total internal reflection (TIR). The phenomenon of TIR occurs when light propagates from an optically denser medium to an optically less dense medium. This phenomenon is based on Snell's Law of reflection [22], which states:

$$n_1 \cdot sin(\theta_1) = n_2 \cdot sin(\theta_2) \ , \tag{2.16}$$

where n_i denote the refractive indices of the first, here the optically denser, medium and the second, here the optically less dense, medium. θ_i gives the angle of incidence of the ray in each medium, see figure 2.10. In the event of $n_2 < n_1$, for values of θ_1 that exceed a critical angle, sine of θ_2 would have to exceed 1 in order to satisfy Snell's law. As this is not possible, the light is subject to total reflection at the interface. TIR occurs for any angle θ_1 greater than the critical angle θ_{crit} determined by the TIR condition:

$$sin(\theta_{crit}) = \frac{n_2}{n_1} \cdot sin(\theta_2 = 90°) \ . \tag{2.17}$$

If the incident angle onto the interface is smaller than the θ_c, partial reflection (Fresnel reflection) and partial transmission occurs. As those are attenuated quickly, those modes can be neglected in the discussion of optical light guides.

Standard optical fibres as used in communication technology, are composed of a singular core material, often glass based. Photons that fulfil the TIR condition inside such a fibre remain trapped and are guided along the fibre towards the ends. However, it should be noted that with these fibres, it is only possible to capture photons that enter the fibre

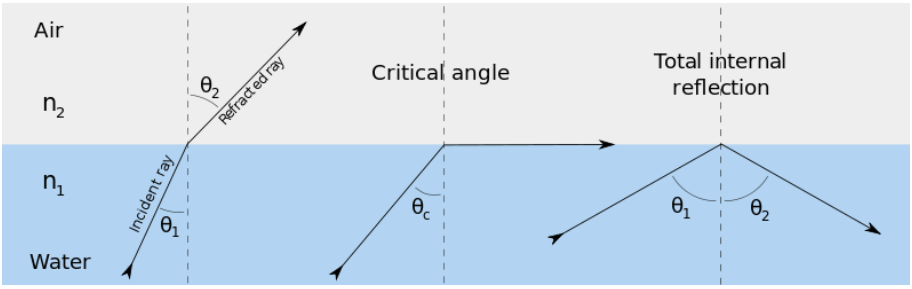

Figure 2.10: Light travels from the optical denser medium (here water) towards the interface to the optical less dens medium (here air). If $\theta_1 < \theta_{crit}$ (left), the light is refracted into the less dense medium. If $\theta_1 = \theta_{crit}$ (middle) the refraction angle is 90°. When θ_1 exceeds the critical angle, the light is reflected back into the denser material (right). This phenomenon is called total internal reflection. Taken from [23].

at either end. Photons that enter the fibre via the lateral surface can't be captured, as under the angle at that they can enter the fibre medium, they can also leave it.

2.7.1 Wavelength Shifting Fibres (WLS-fibres)

To collect lateral arriving light, special optical WLS-fibres can be used that are commercially available. Often they consist of a polystyrene core, cladded with one (single clad) or even two layers (multi clad) of materiels with decreasing refractive indices. The WLS molecules are distributed uniformly throughout the fibre core. Photons that enter the fibre can be absorbed by the WLS molecules and are re-emitted isotropically. Consequently, there exists a possibility that the re-emitted photon will fulfil the TIR condition, whether at the core-cladding or at the cladding-surrounding interface, and become trapped. The photons trapped at the core-cladding interface will be referred to as core rays, the ones captured at the cladding-surrounfing interface cladding rays. The trapped photons are than piped along to the fibre ends. A sketch of the light trapping process in a single cladded WLS fibre can be found in figure 2.11. It should be noted, that the amount of cladding rays can be larger compared to the core rays when the difference refractive index between the core and cladding is smaller then that between the cladding and the surrounding material. But earlier studies indicate that these photons attenuate quite quickly due to poor outer surface qualities. After a few tens of cm those rays do not contribute significantly to the light output of the fibre [24].

Generally, the emitted photons can be categorised by their path along the fibre in two groups: meridional and skew rays. Meridional rays are confined to a single plane along the fibre axis. All others are skew rays.
As shown in the middle sketch of figure 2.12, at the point of surface encounter, skew rays exhibit a skew angle $\gamma > 0$ in between the surface normal $\vec{n}$ and the direction of the photons path $\vec{p}$. Therefore they spiral along the photons path. The emitted photons hit the surface under an angle α, given by:

$$cos(\alpha) = \vec{n} \cdot \vec{p} \tag{2.18}$$

To fulfil the TIR condition $\alpha \geq \theta_{crit}$ must be satisfied. The capture efficiency of a

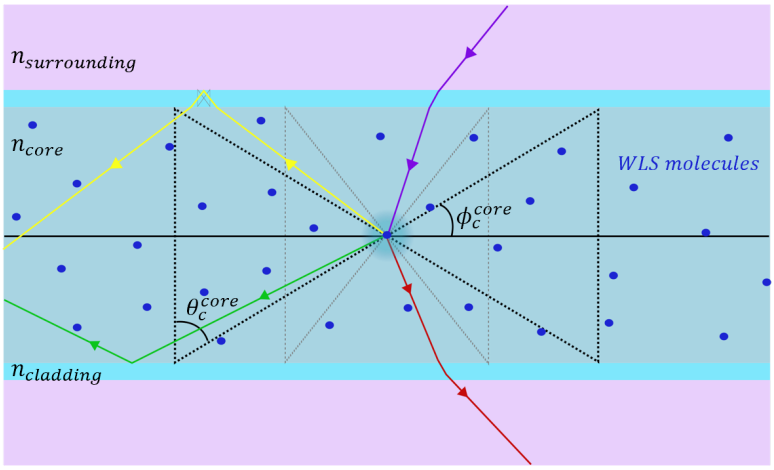

Figure 2.11: Illustration of the light capturing process in WLS fibres. The sketch shows a 2D cut trough a single cladded WLS-fibre along the fibre axis. The refractive indices decrease from the core to the outside: $n_{core} > n_{cladding} > n_{surrounding}$. An initial photon (purple ray) enters the fibre and is absorbed by a WLS molecule (blue dot). The emission happens isotopically, different scenarios are displayed. The dashed black lines outline the projection of the capture cone with an opening angle of $\phi_c^{core} = \pi/2 - \theta_c^{core}$. If a photon is emitted within this cone (green ray), the TIR is fulfilled at the core-cladding interface and the photon is piped along the fibre. Even if a photon is emitted outside this cone, due to the cladding, there is another chance that TIR can happen at the cladding-surrounding interface (yellow ray). The grey dotted lines indicate the capture cone in this case. If the photon is emitted at an even steeper angle with respect to the fibre surface, the ray will leave the fibre (red ray). Sketch is not to scale. All rays are meridian.

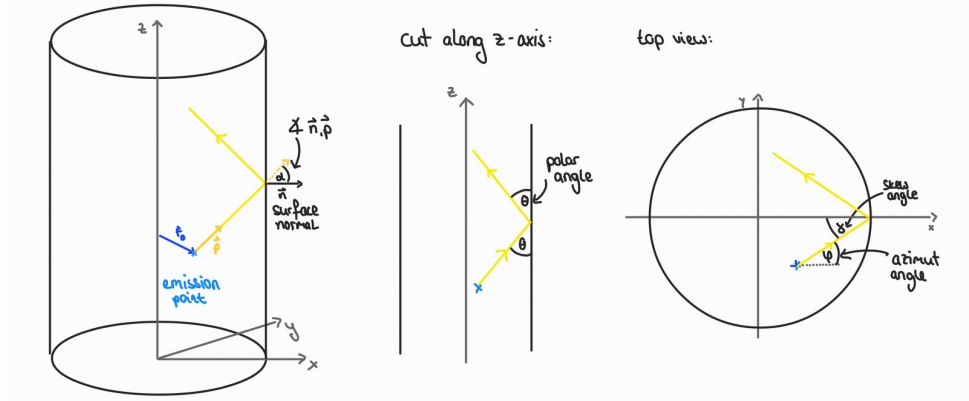

Figure 2.12: Sketch of the propagation of a skew ray in a WLS fibre.

cylinder fibre is given by

$$\epsilon_{TIR} = \frac{1}{4\pi} \int \Theta\Big(|\vec{n} \cdot \vec{p}| - cos(\theta_{crit})\Big) d\Omega \ , \tag{2.19}$$

Θ denotes the Heaviside step function. As the WLS molecules are uniformly distributed within the core material, the point of emission $\vec{r_0}$ can be off axis and also increases the capture efficiency:
Lets consider a fibre of radius R. Lets place the coordinate system such that z axis is placed along the fibre axis. Further we use spherical coordinates where θ and φ denote polar and azimuth angles respectively. The emitting WLS molecule is placed at $\vec{r}_0 = (r_{\text{em}}, 0, 0)$ (with $0 \leq r_{\text{em}} \leq R$) and the photon leaves in direction $\vec{p} = (\sin\theta\cos\varphi,\ \sin\theta\sin\varphi,\ \cos\theta)$. The photons path to the first surface intersection can be parametrised by

$$\vec{r}(t) = \vec{r}_0 + t\vec{p} \qquad with\ t > 0. \tag{2.20}$$

The hit point on the fibre surface occurs at a time t_+ that can be determined by solving the following for t:

$$\begin{aligned} R^2 &= x^2 + y^2 \\ &= \big(r_{\text{em}} + t\sin\theta\cos\varphi\big)^2 + \big(t\sin\theta\sin\varphi\big)^2 \\ \Leftrightarrow 0 &= t^2\sin^2\theta + 2r_{\text{em}}\, t\sin\theta\cos\varphi + (r_{\text{em}}^2 - R^2) \end{aligned} \tag{2.21}$$

For $\sin\theta \neq 0$, the positive solution is

$$t_+ = \frac{-r_{\text{em}}\cos\varphi + \sqrt{R^2 - r_{\text{em}}^2\sin^2\varphi}}{\sin\theta} \qquad . \tag{2.22}$$

The surface normal at the hit point $\vec{n}$ is given by

$$\vec{n} = \left(\frac{x_{\text{hit}}}{R},\ \frac{y_{\text{hit}}}{R},\ 0\right).$$

where

$$\begin{aligned} x_{\text{hit}} &= r_{\text{em}} + t_+\sin\theta\cos\varphi, \\ y_{\text{hit}} &= t_+\sin\theta\sin\varphi. \end{aligned}$$

To check where the TIR condition is fulfilled, the dot product has to be calculated:

$$\begin{aligned} \vec{n}\cdot\vec{p} &= \frac{1}{R}\Big(\sin\theta\cos\varphi\,(r_{\text{em}} + t_+\sin\theta\cos\varphi) + \sin\theta\sin\varphi\,(t_+\sin\theta\sin\varphi)\Big) \\ &= \frac{\sin\theta}{R}\Big(r_{\text{em}}\cos\varphi + t_+\sin\theta(\cos^2\varphi + \sin^2\varphi)\Big) \\ &= \frac{\sin\theta}{R}\Big(r_{\text{em}}\cos\varphi + t_+\sin\theta\Big) \\ &= \frac{\sin\theta}{R}\Big(r_{\text{em}}\cos\varphi + \big(-r_{\text{em}}\cos\varphi + \sqrt{R^2 - r_{\text{em}}^2\sin^2\varphi}\,\big)\Big) \\ &= \frac{\sin\theta}{R}\Big(\sqrt{R^2 - r_{\text{em}}^2\sin^2\varphi}\Big) \quad . \end{aligned} \tag{2.23}$$

By defining the dimensionless offset

$$x_0 \equiv \frac{r_{\text{em}}}{R}, \qquad 0 \leq x_0 \leq 1 \tag{2.24}$$

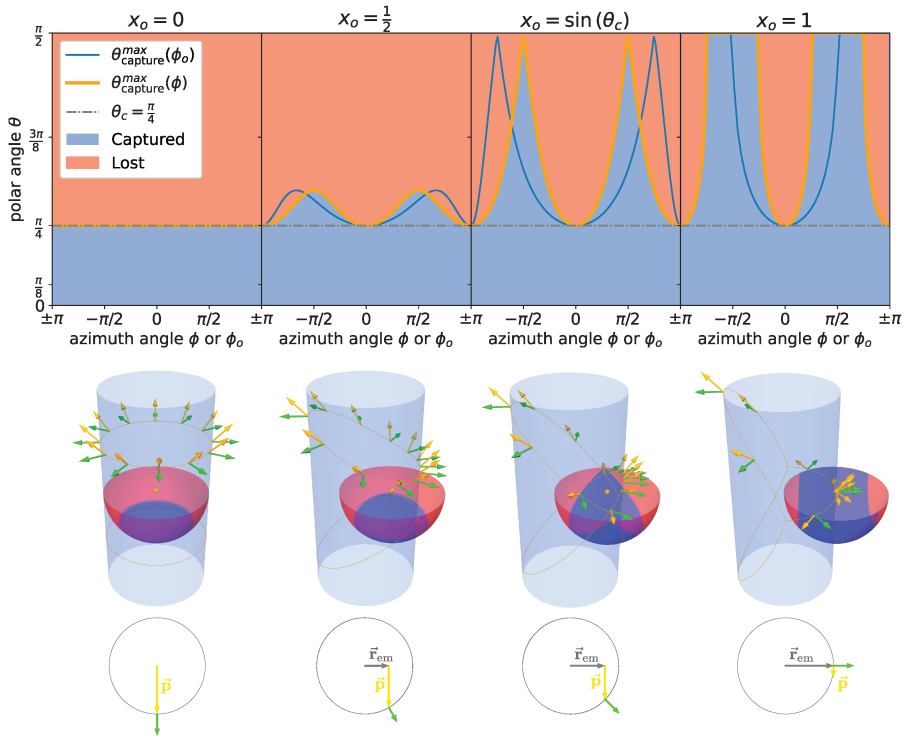

Figure 2.13: "Illustration of the solid angle under which the photons are captured as a function of the relative fraction of the radius x_0 at which the photons are emitted (indicated by the yellow dot). The orange (blue) line in the upper plot indicates photons that encounter the surface under the critical angle as a function of the azimuth angle $\phi\,(\phi_0)$ relative to the point of emission (centre of the cylinder). In the upper and middle plots the blue shaded areas indicate solid angle regions under which photon trajectories are captured by total internal reflection, while red shaded areas show those that are not captured. In the middle plot yellow arrows indicate directions of incident photons, while green arrows depict surface normals. In this example, the critical angle is chosen as $\theta_c = \pi/4$." Taken from [25].

one can further condense the equation to

$$\vec{n} \cdot \vec{p} = \sin\theta \sqrt{1 - x_0^2 \sin^2 \varphi} \quad . \tag{2.25}$$

Plugging this into the TIR condition yields

$$cos\theta_{crit} \geq \sin\theta \sqrt{1 - x_0^2 \sin^2 \varphi} \tag{2.26}$$

To conclude, three parameters have an effect: the relative emission radius x_0 as well as θ and φ defining the photons path. Figure 2.13 displays the effect of all parameters on the capture efficiency. The capture fraction increases as x_0 gets closer to 1. If $x_0 \geq sin(\theta_{crit})$ the possibility to also capture capture horizontally emitted rays ($\theta = \pi/2$) arises. From the figure one can also see, that the larger x_0 is, the more skew rays are produced.
Skew rays largely contribute to the capture rate of WLS fibres. However, as they spiral along the fibre axis, they travel a much longer distance till they reach the fibre's ends and undergo more TIR reflections in comparison to meridian rays. This renders them more susceptible to absorption.

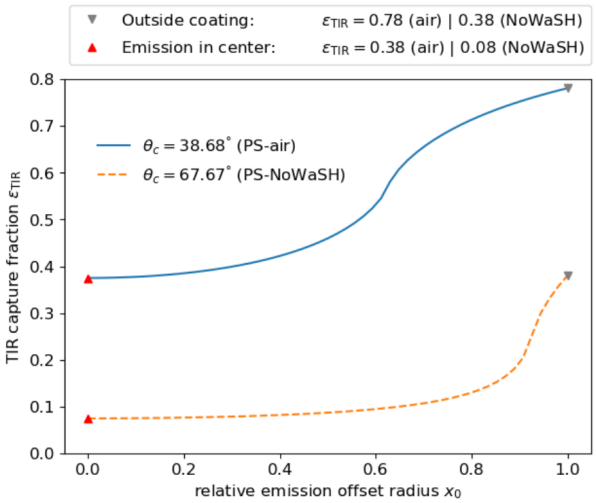

Figure 2.14: Fraction ϵ_{TIR} of emitted photons over the solid angle trapped under TIR as a function of the emission point's offset radius x_0. The curves show the relation for a WLS polystyrene fibre immersed in air (blue, solid line) or the scintillator NoWaSH (orange, dashed line). Reused from [1].

2.7.2 Optimised Wavelength Shifting Fibres (OWL-fibres)

Detectors that aspire to utilise WLS fibres for the purpose of light collection through a detection medium stand to benefit from the recently developed OWL fibres [26]. In contrast to commercial optical fibres, in which the WLS molecules are dispersed throughout the fibre material, OWL fibres (OWLs) possess a pure plastic or glass core and are coated with a thin layer of wavelength-shifting paint (WLS paint). This results in the point of re-emission being positioned on the OWL surface, yielding $x_0 = 1$. As previously discussed, this configuration results in an enhanced capture fraction. The enhancement in the capture fraction, denoted by ϵ_{TIR}, with respect to the emission radius offset, is evident, as demonstrated in figure 2.14

To this point, only OWL prototypes are available. For the OWL cores, fibres made from Quartz, PMMA (Poly(methyl methacrylate)) or Polystyrene are obtained commercially. The WLS paint is self-made: a plastic like PMMA, PEMA (Poly(ethyl methacrylate), $(C_6H_{10}O_2)_n$) or Polystyrene is dissolved in Toluene. WLS molecules are mixed into the paint at small concentrations and the paint is then applied onto the fibre via dip-coating. The layer thickness is influenced by the velocity with that the fibre is drawn out of the paint. The paint dries as the Toluene evaporates, leaving a matrix of the plastic as paint layer within which the WLS molecules are uniformly distributed.

2.8 γ Spectroscopy

Gamma rays interact over a variety of interaction mechanisms with matter leading to a sudden change in the gammas energy and direction or even to disparateness of the gamma. In either case most of the gamma's energy is transferred to an electron in the material. The most relevant mechanisms are photoelectric absorption, Compton scattering and pair production. As can be seen in figure 2.15, what process is dominate is determined by the gammas energy as well as the atomic number Z of the absorber. Photoelectric absorption

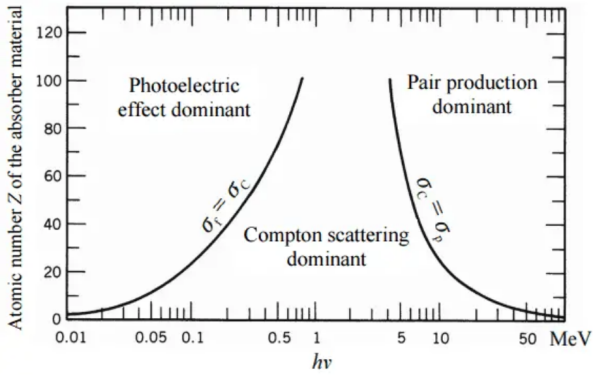

Figure 2.15: Plot showing the relative dominance of each process depending on the gamma energy and the absorber's atomic number. Adapted from [27].

is the process where the gamma with energy $E_\gamma = h\nu$ completely disappears by the interaction with an absorber atom. An energetic photoelectron is ejected from a bound shell with an energy of

$$E_{e^-} = E_\gamma - E_b \ . \tag{2.27}$$

E_b is the binding energy of the electron. The photoelectron carries the majority of the gammas energy if the initial gamma energy was more than a few hundred keV. The vacancy left by the photo electron is quickly filled thought rearrangement of the electrons in the atom's shell structure and/or by the capture of a free election inside the medium. Consequential the binding energy is liberated via the emission of characteristic X-rays and/or Auger electrons. Photoelectric absorption is the prominent interaction for gammas with relatively low energies or absorber materials of high atomic number Z. A rough approximation for the probability of photoelectric absorption τ is given by

$$\tau \cong \frac{Z^n}{E_\gamma^{3.5}} \ , \tag{2.28}$$

where n varies between 4 and 5.

Compton scattering takes place between an electron in the absorber material and the initial gamma. The incoming gamma is deflected through an angle θ from its original direction. Part of the gammas energy is transferred to the so-called recoil electron. In the rest frame of the initial electron, the scattered gammas energy $_{\gamma'}$ is given by the Compton formula

$$E_{\gamma'} = \frac{E_\gamma}{1 + \frac{E_\gamma}{m_e c^2}(1 - cos(\theta))} \ . \tag{2.29}$$

m_e notes the electrons rest mass and c the speed of light. The recoil electron's energy is given by

$$E_{e'} = E_\gamma - E_{\gamma'} \ . \tag{2.30}$$

The probability of Compton scattering depends on the number of electrons in the absorber and therefore increases linearly with Z. The differential scattering cross section $d\sigma/d\Omega$ is given by the Klein-Nishina formula:

$$\frac{d\sigma}{d\Omega} = Z r_0^2 \left(\frac{1}{1 + \alpha(1 - cos(\theta))}\right)^2 \left(\frac{1 + cos(\theta)^2}{2}\right) \left(1 + \frac{\alpha^2(1 - cos(\theta))^2}{(1 + cos(\theta)^2)(1 + \alpha(1 - cos(\theta)))}\right) \tag{2.31}$$

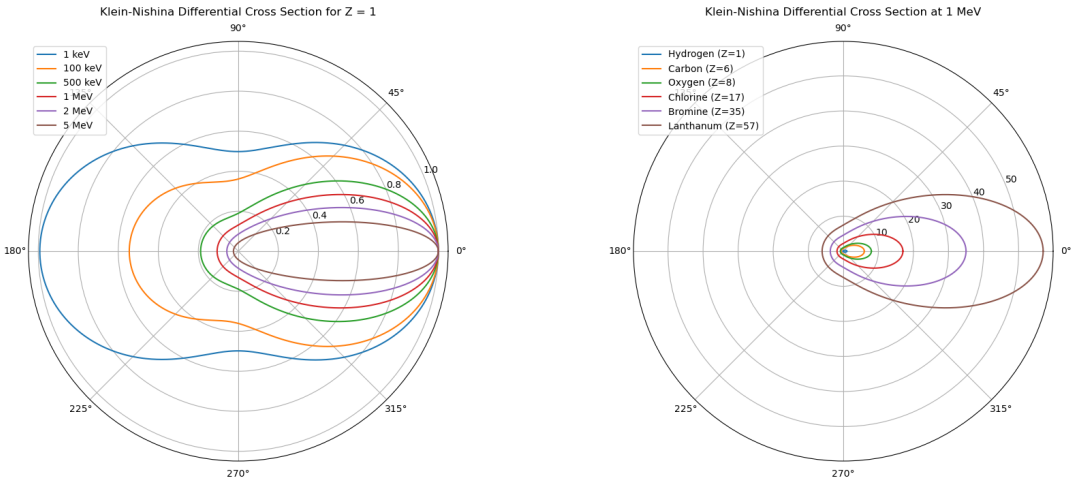

Figure 2.16: Polar plot of the photon number scattered under the scattering angle θ given by the Klein-Nishina differential cross section (Eq. 2.31) for various gamma energies at fixed Z = 1 (left) and for different atomic numbers Z at a fixed gamma energy of 1 Mev (right).

where $\alpha = E_\gamma / m_0 c^2$ and r_0 gives the classical electron radius. Figure 2.16 shows the influence of Z and E_γ onto the angular distribution. For higher gamma energies, the probability for forward scattering increases significantly, the backscatter probability drops simultaneously.

Pair production is only possible if the gamma energy exceeds twice the electrons rest mass energy, hence 1.02 MeV. In the coulomb field of a nucleus, a gamma can disintegrate into an electron position pair. The residual energy $E' = E_\gamma - m_0 c^2$ is distributed as kinetic energy between electron and positron. The probability for pair production remains relatively low unless the gamma energy exceeds several MeV. Further it varies approximately with the square of the absorber's atomic number Z.

A common way to record a gamma spectrum is with scintillation detectors, were the scintillator acts as absorber material, emits scintillation light that then is recorded by a photon counting device for example a PMT. The shape of the recorded gamma spectrum highly depends on the size and geometry of the scintillator, as well as the material and especially its atomic number Z. Further not all features of the gamma interactions are visible in all detectors. The features are not discrete peaks and sharp edges due to smearing and limited energy resolution. In section 4.4.1 and 4.4.2 the gamma spectrum of Co-60 is taken with a Lithium bromide crystal and a liquid scintillator sample will be discussed in detail.

2.9 Cobalt 60

Cobalt 60 is a radioactive isotope that can be used as gamma source. The isotope undergoes β^- decay into an excited state of Nickel 60 with a half-life of 5.2714 years:

$$^{60}Co \rightarrow ^{60} Ni^* + \beta^- + \bar{\nu}_e \ . \tag{2.32}$$

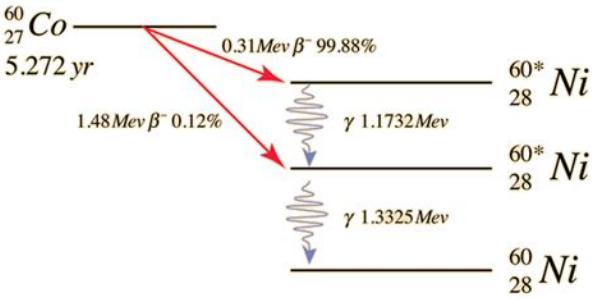

Figure 2.17: Decay scheme of Cobalt-60. Taken from [28].

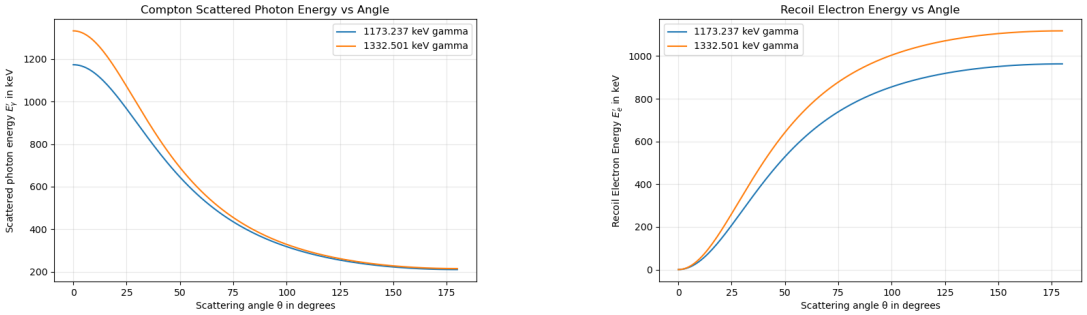

Figure 2.18: Energy of Compton scattered gamma given by Eq.2.29 (left) and the resulting recoil electron's energy (right) for all scattering angles θ.

In 99.8 % of the cases, the Ni-60 nucleus is left in an excited 4^+ state and relaxes via the sub sequential release of two gammas :

1. a 1.173 MeV gamma during the transition $4^+ \rightarrow 2^+$
2. a 1.332 MeV gamma in the transition $2^+ \rightarrow 0^+$.

Figure 2.18 shows the energy of a Compton scattered gamma and the recoil energy in dependants of the scattering angle as predicted by the Compton scatter formula 2.29.

Chapter 3

NuDoubt^{++}

This chapter is based on [1].
NuDoubt^{++} is an experiment planned to study double beta plus decay. In view of the fact that double beta decays are extremely rare processes, a detector with both excellent energy resolution and background suppression capabilities is required.
The *NuDoubt*$^{++}$ collaboration has therefore proposed an innovative detector concept based on a hybrid-slow opaque scintillator penetrated by a dense grid of OWL-fibres. An isotope, undergoing double beta plus decay, is loaded into the scintillator. The isotope under consideration is Krypton-78, with Cadmium-106 and Xenon-124 as alternative candidates.
The concept of combining several novel approaches involves the integration of their individual background suppression capabilities. That is to say, the good C/S separation, energy resolution and low energy threshold of a hybrid-slow scintillator should be combined with the excellent spatial resolution of an opaque scintillator penetrated by a dense grid of optical fibres, which is able to resolve the topological event information. The utilisation of OWL-fibres is instrumental in ensuring a sufficient photon capture rate. Furthermore, as elucidated in section 2.5.3, LS allow high isotope loading, thereby increasing the target isotope fraction in the detector volume.

3.1 Double Beta plus decays

Double Beta decay is a second order weak interaction with a correspondingly long half-live of 10^{18} to 10^{24} years. This process can occur in unstable nuclei where single beta decays are energetically forbidden or strongly suppressed by the conservation of angular momentum. In the Standard Model (SM), each double beta decay ($2\nu2\beta$), produces two (anti)neutrinos. However, the possibility of non-SM, neutrinos-less double beta decay ($0\nu2\beta$) has also been postulated, which would suggest the Majorana nature of the neutrinos. Indeed, double beta decay processes provide the most precise experimental access to probe the Majorana nature [2],[3].
NuDoubt^{++} will exploit the less explored double beta plus decays. Within the SM, 3 decay modes are possible:

$$\text{Double positron decay } 2\nu2\beta^+ : \qquad (A,Z) \rightarrow (A,Z-2) + 2e^+ + 2\nu \tag{3.1}$$

$$\text{Positron emitting electron capture } 2\nu EC\beta^+ : \quad (A,Z) + e^- \rightarrow (A,Z-2) + e^+ + 2\nu \tag{3.2}$$

$$\text{Double electron capture } 2\nu2EC : \qquad (A,Z) + 2e^- \rightarrow (A,Z-2) + 2\nu \ . \tag{3.3}$$

The experimental signature of the decay modes associated with positrons is the simultaneous emission of 511 keV annihilation gamma rays. One pair of gammas, in the case

of $2\nu EC\beta^+$, or two, in the case of $2\nu 2\beta^+$. Neither process has been observed experimentally. The event signature of the only mode observed so far, $2\nu 2EC$, is a cascade of X-rays and Auger electrons generated during the filling of vacancies following the capture of two inner-shell electrons. It is important to note that ND will be sensitive to the two positron-emitting decay modes.
Analogous to the 3 SM modes, the non-SM neutrinoless process can be formulated as follows:

$$\text{Neutrino-less double positron decay } 0\nu 2\beta^+ : \quad (A, Z) \rightarrow (A, Z-2) + 2e^+ \tag{3.4}$$

$$\text{Neutrino-less positron emitting electron capture } 0\nu EC\beta^+ : \quad (A, Z) + e^- \rightarrow (A, Z-2) + e^+ \tag{3.5}$$

$$\text{Neutrino-less double electron capture } 0\nu 2EC : \quad (A, Z) + 2e^- \rightarrow (A, Z-2)\ . \tag{3.6}$$

These processes have expected half-lives of 10^{26} years or more. All three violate lepton number conservation by two units and, if observed, would lead to the Majorana nature of the neutrinos and offer the potential to discover the neutrino Majorana mass.

3.2 Proposed prototype

The detector prototype is shown in figure 3.1. It has a cylindrical shape to facilitate the implementation of the OWL fibres. The inner detector measures 110 cm in diameter as well as in height and contains approximately one tonne of hybrid slow opaque scintillator. Approximately 13,000 OWL fibres will run parallel to the cylinders' symmetry axis, arranged in a triangular grid with a pitch of $\mathcal{O}(1\ cm)$. Every OWL-fibre will be connected to a SiPM at each end. This setup will be surrounded by a cylindrical vessel with PMTs implemented at the top and bottom, containing transparent LS to act as an active veto. In the centre of the inner detector, a smaller target detector with a fiducial volume of about 10 litres can be inserted. This target volume will contain the isotope loaded hybrid-slow opaque scintillator.
The detector must be placed in a shielded environment, such as deep underground mines, to reduce the background as much as possible.

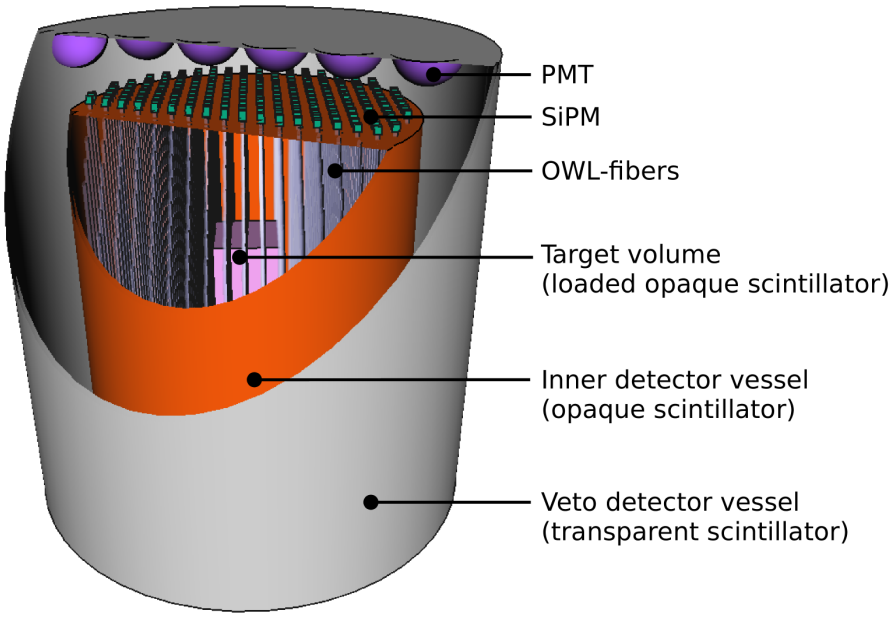

Figure 3.1: „Basic detector design, explained from the outer to the inner layer: the active veto volume (grey) has a diameter and height of 155 cm, is filled with transparent scintillator and has PMTs (purple) on the top and bottom; the inner detector volume (orange) has a diameter and height of roughly 110 cm, holds 1 t of unloaded hybrid-opaque scintillator and parallel-running OWL-fibres (light grey) with a diameter of 3 mm and a fibre pitch of 1 cm (fibre pitch has been increased in the drawing for a better visualisation); dedicated SiPMs and electronics (green) are at both ends of each fibre. The inner cubical target volume (pink) is filled with about 10 kg loaded hybrid-opaque scintillator and has an edge length of roughly 10 cm.“Reprinted from [1]

Chapter 4
Proof of Concept Detector

The objective of this thesis is twofold: firstly, to verify that light collection with OWLs in opaque LS is indeed possible; and secondly, to conduct a comparative study between different fibres and opaque LS. To this end, a light yield backscatter setup has been designed.
In the following chapter, the materials available for consideration are discussed. Then the final version of the light yield backscatter setup is presented. In the final section, the Co-60 spectrum recorded with the two scintillation detectors utilised in the set-up are examined.

4.1 Materials

In this section, the material under consideration is discussed alongside the experiences made with it and the reasoning behind the final selection of materials.

As the final $NuDoubt^{++}$ experiment will be performed in a deep under-ground laboratory with increased safety considerations, the scintillator LAB is a good choice as base. The substance under consideration is a satisfactory scintillator, exhibiting both adequate transparency and a high flashpoint of approximately 140 °C. Furthermore, it is characterised by its low hazardousness level [29]. As the feasibility study of $NuDoubt^{++}$ is conducted using an opaque, LAB-based scintillator (see section 3.2.1), it is logical to also consider LAB-based LS in this context.

The OWL core material must exhibit high transparency in the optical regime and attenuation lengths in the order of metres. Possible core candidates are fused quartz ($Si0_2$), PMMA (Poly(methyl methacrylate), $(C_5H_8O_2)_n$), and polystyrene ($(C_8H_8)_n$). The plastics PEMA (Poly(ethyl methacrylate), $(C_6H_{10}O_2)_n$), PMMA, and polystyrene can also be used as a matrix inside the WLS paint applied to the core to create the OWL fibre. Table 4.1 shows the refractive index of those materials. A spectrum of the refractive index of PEMA is not available to the public, but the refractive index is generally assumed to be matching that of PMMA [30]. For simplicity dispersion is neglected. The refractive indices n are estimated to a fixed value, taking the value of n at a wavelength of 450 nm.

It is advantageous for the core to possess a higher refractive index in comparison to the paint material, thereby preventing the trapping of photons within the paint layer. However, it should be noted that this is not a prerequisite. It is imperative to note that the refractive index of the paint is higher than that of the surrounding material; hence the LS. The liquid scintillator LAB has a refractive index of about $n_{LS} = 1.4970.005$ [32]. Although PMMA and PEMA have a slightly higher refractive index than LAB, the difference is de facto negligible, making them unsuitable for enabling TIR. The best choice

Material	Quartz	PMMA	Polystyrene
n (@ 450 nm)	1.4656	1.5016	1.6136

Table 4.1: Refractive indices of fused quartz, PMMA and Polystyrene at an wavelength of 450 nm. The refractive indices were taken from [31].

is be polystyrene.

As LAB is not only a scintillator, but also a solvent, it was observed that polystyrene OWLs were completely dissolved within a few days inside the LAB. Therefore polystyrene based paint and cores are not suitable for direct implementation inside the LAB, making LAB resistivity another criterium. PMMA and Quartz are LAB resistant. Nonetheless, it was observed that paints based on PMMA peeled off from quartz cores, as LAB is capable of crawling into even the tiniest cracks in the paint. Under the assumption that PEMA paint would not perform better, the idea of putting the OWL fibres directly into the scintillator had to be abandoned. As an alternative, the concept of the so-called Bubo fibre was born.

4.2 From OWL to Bubo

The term "Bubo fibre" is used to denote the complex of an OWL fibre within a protective tube. The name arises from the biological genus "Bubo", that contains large, powerful owls with ear tufts.

The tubes have been designed to have a slightly larger inner diameter, resulting in a small air gap between OWL and tube. The tubes utilised in this thesis were fabricated from fused quartz glass; however, they could also be fabricated from PMMA or any other transparent, LAB-resistant material. The bottom end of the tube was sealed by gluing in a 3D-printed cap. On the inside of the cap, a centred ring allowing for a tight fit of the OWL is placed. It serves to fixate the OWLs right in the tube's centre. Reflective foil was adhered to the interior surface of the ring, with the purpose of reflecting photons that had traversed the fibre's length back towards the top. In order to prevent the ingress of LAB into the tube, the capped extremity of the tube was immersed in a resin which was subsequently hardened under UV light.

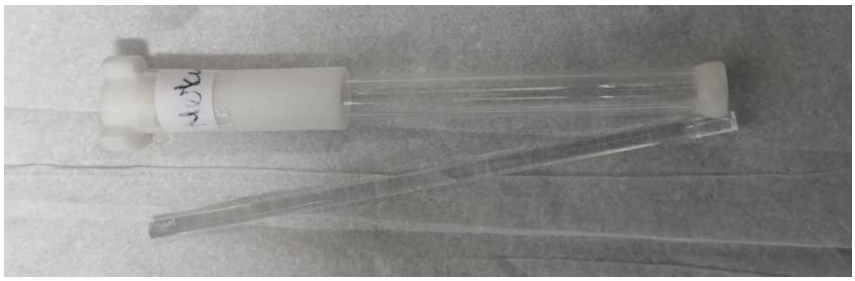

Figure 4.1: The two main components of a bubo fibre: the WLS fibre (bottom) and the quartz tube (top) with both of it's endcaps. In the final assembly the fibre is plugged into the tube and is thus protected form the dissolving LS.

In this way (see figure 4.1), the OWLs are protected from direct LAB contact. The presence of the additional tube influences the trapping efficiency of the OWL. The air gap has a positive influence on the TIR capture efficiency of the OWL due to the larger difference in refractive index between WLS paint and air. However, it should be noted that the tube introduces additional TIR and Fresnel losses at both the tube - air interface, and in the case of quartz tubes, also at the LS - tube interface. Moreover, the active LS volume is reduced when the OWLs are substituted for Bubos, as the tubes must have a marginally

larger inner diameter than the fibre. Furthermore, the commercially available tubes have a wall thickness of 1 mm or greater. The increase in the amount of inactive material in the detector, is accompanied by a reduction in scintillation light output. Additionally, the inactive material present inside the detector enlarges the background, a quite critical object for real physics measurements.

4.3 Experimental Setup

In order to demonstrate the light collection principle with OWL fibres in an opaque LS, a tabletop light yield setup was designed as a proof of concept detector. This section presents the final version of the setup. A sketch, as well as a photo, can be found in figures 4.3 and 4.2.

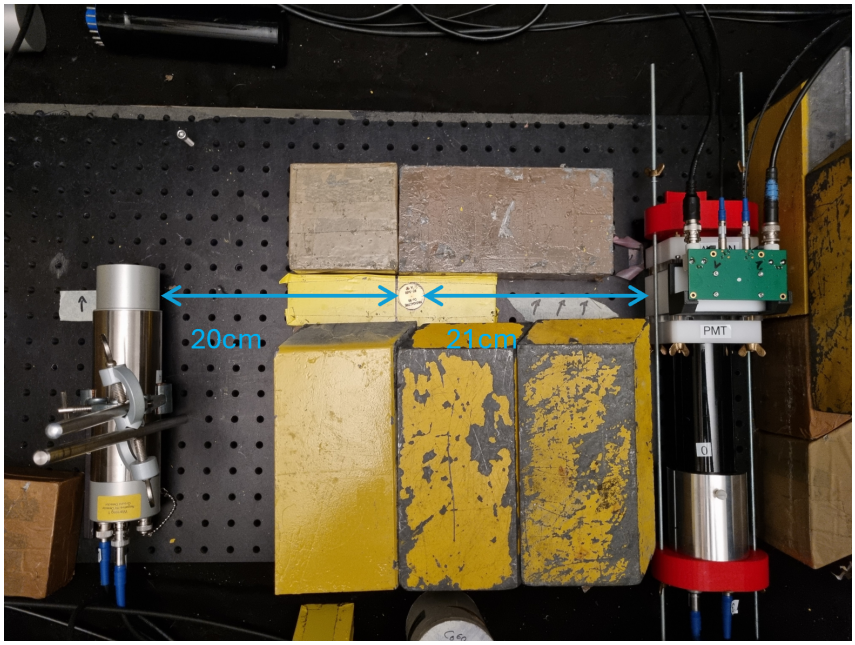

Figure 4.2: Photo of the Light Yield Backscatter setup. In the centre, a 3MBq Co-60 source is placed. Usually it is covered on the top by lead slaps, they were removed for the photo. To the left of the Co-60 source, the LBC detection unit is placed. To the right, the LS-fibre detector is placed.

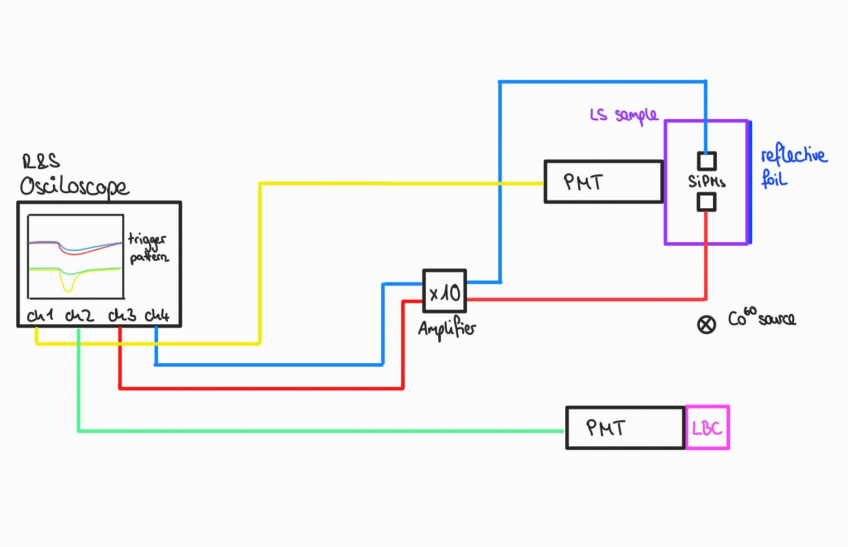

Figure 4.3: Sketch of the proof of concept detector Setup and the signal paths.

The configuration of the system was designed as a Light Yield Backscatter setup. The apparatus consists of two scintillation detectors, a lanthanum bromide crystal read out by a PMT and a a LS filled cavity that is faced by another PMT. Further 2 fibres run through the LS volume which are read out by SiPMs. The union of the later described detector complex is called LS-fibre detector. Both detectors are placed on either side of a gamma source. A 3 MBq Cobalt-60 sample was utilised as the gamma source.

The LS-fibre detector is composed of a small cavity (see technical drawing in figure A.1). This cavity, with a volume of: 3 mm × 5.12 mm × 6.36 mm, can be filled with LS. The fibres can enter the LS via holes in the cavity's lid. A 3D-printed structure, affixed to the lid, contains a board on which SiPMs are mounted. The excess of the fibres, that stands out of the cavity, are each fixed within a 3D printed holder. The holders are affixed to the board in such a manner that each fibre is oriented towards a 6 mm × 6 mm SiPM (Hamamatsu, S13360-6050VE). The fibres were measured at 98 mm in length when placed directly into the LS and 96 mm when utilised within the quartz tubes (Bubo fibres). The lengths were chosen such that the fibre fitted just right in between the Polytetrafluoroethylene (PTFE) cavity bottom or Bubo cap and the SiPM. Due to tolerances, air gaps in the submillimeter regimes might occur between upper fibre end and SiPM. The lateral surfaces of the cavity are composed of acrylic glass. A 2" PMT (HZC Photonics, XP2020 series) is positioned in such a manner that it faces the LS through one of the glass windows; the other window is sealed with reflective foil. In Figure 4.4, the view into the LS-fibre detector cavity through the PMT window is shown.

The plastic scintillator detector (Type: 51B102/2M-E1-EJ230-X-NEG) from Scionix is utilised as a backscatter detector. In this thesis, the detector is referred to as LBC, or the LBC detection unit. The apparatus under consideration consists of a cylindrical cerium-activated lanthanum bromide (LaBr3:Ce) scintillation crystal, hereafter referred to as the LBC, with a diameter of 2 inches and a length of 102 millimeters. The crystal is viewed by a 2-inch PMT (Hamamatsu, R13089-100).LBC and PMT are united in an light- and air-tight 1 mm aluminium case.

The connection of the devices is shown in figure 4.3. The PMT, LBC and SiPMs signals

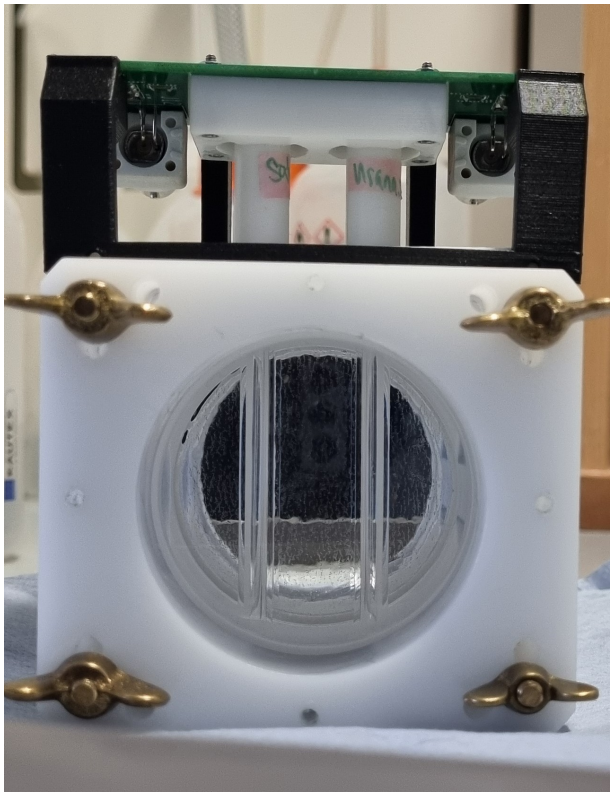

Figure 4.4: Look into the LS cavity through the PMT hole. The cavity is filled with transparent LS, Bis-MSB coated bubo-fibres are inserted. Reflective foil is glued to the opposite glass window. The black holding structure holds the board where the SiPMs are mounted to. The fibre ends are connected to the SiPMs via the white fixing structure.

enter a RTO64 oscilloscope from Rohde&Schwarz. The SiPM signals are amplified by a gain-10 linear amplifying NIM module (LeCroy, Model 612A) prior to being entered into the oscilloscope.

In Appendix B, the PMT and SiPM characterisations are displayed. The PMT was operated at a voltage of 1800V. The breakdown voltages of the SiPM were determined and the SiPMs were operated at 3V over voltage.

The concept underpinning the backscatter configuration involves the selection of events in which a gamma ray undergoes a 180° backscatter within the LS sample. In this case, the energy deposited in the sample is known and can be determined by the Compton backscatter formula (see equation 2.30). The knowledge of the deposited energy thus enables an estimation on the efficiency of the light collection with fibres. As demonstrated in figure 2.18, the variation in deposited energy is minimal for large scattering angles above 125°. In order to select the 180° backscatter events, it is necessary to employ an additional detector positioned on the opposite side of the Co-60. Due to the negligible delay in time of flight, the backscattered gamma is seen instantly in the LBC with a known energy. This forms the basis for the applied triggering and event filtering. Further information on the triggering will be given in sections 5.3- 5.4 .

4.4 Co-60 spectrum

Since this backscatter setup essentially involves gamma spectroscopy and both scintillator responses are used for filtering, it is necessary to discuss the Co-60 gamma spectrum obtained from either sample.

4.4.1 LBC response

Figure 4.5 is a histogram showing the Cobalt-60 spectrum recorded with the LBC. The signal threshold was set quite low, to -27 mV, revealing the largest part of the spectrum.

The two photo peaks are prominent, corresponding to 1.173 MeV and 1.332 MeV. In addition, the two Compton edges are observable to the left of these. As the Compton edges represent instances of 180° backscattering of gamma within the sample, they are equivalent to energies of approximately 963 and 1117 keV, respectively. The Compton continua of both gamma rays overlap, which complicates the discernment of other features.

An overlaid or combined backscatter peak becomes observable at a further leftmost position along the aforementioned continuum. The nomenclature of this peak is counterintuitive, as it does not represent the case of 180° backscatter occurring within the scintillator. Rather, it is indicative of a gamma that backscattered elsewhere and was subsequently absorbed in the LBC. In accordance with the Compton formula, the energy levels of the gammas are determined to be 210 or 215 keV, respectively. As the energy difference between those is only 5 keV, they cannot be separated due to limited energy resolution. The peak is assigned to the energy of $(210\ keV + 215\ keV)/2 = 212.5\ keV$.

To the right of each photo peak, a smaller peaks are visible. These may occur due to true coincidence photo peak-summing, i.e. when the two gamma rays from one Co-60 decay are emitted in the same direction within a short time window. If that window is unresolvable for the LBC, the photo absorption of one gamma ray is overlaid with another gamma ray undergoing a Compton scattering process. However, the full sum peak of coincidental photo peak absorption at 1.173 MeV + 1.332 MeV = 2,505 MeV is

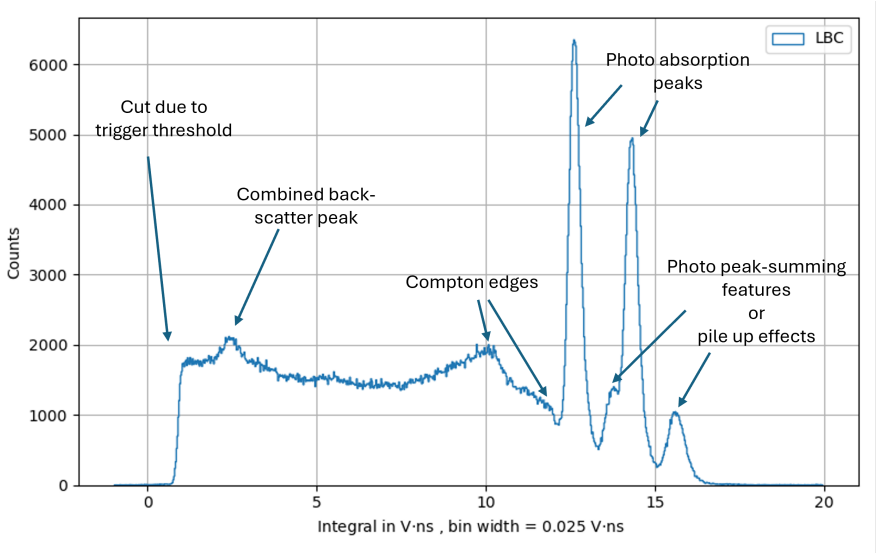

Figure 4.5: This histogram shows the Co-60 spectrum recorded by the LBC. The two prominent features are the photo peaks at 1.173 MeV and 1.332 MeV. The two Compton edges are also visible at around 963 keV and 1117 keV respectively. All other features of the spectrum are superimposed and cannot be resolved individually, except for a combined backscatter peak. Smaller peaks arise just next to the right of the photo absorption peaks. Possible explanations for these are photo peak summing or pile-up effects.

not visible. As the rate of gamma emission is elevated, an alternative hypothesis for those small neighbouring peaks is pulse pile-up effects [8]. This describes an artificially detected coincidence, arising when two gamma rays interact within the same time resolution window, but they originate from separate nuclear decays. Electric time resolution is the bottleneck in this case. Since these small neighbouring peaks disappear when the trigger rate is reduced, they are most likely due to pile-up effects.

4.4.2 Transparent LS response

Figure 4.6 shows the gamma spectrum recorded by the PMT viewing transparent LS inside the LS-fibre detector. In comparison to the LBC spectrum, it exhibits a significantly lower number of features. The photo peaks are not visible due to the low atomic numbers of the elements present in the LS. The Compton continuum can be seen, ending with a combined Compton edge, as the individual edges cannot be resolved. The averaged Compton edge is located at an energy of $(963\ keV + 1117\ keV)/2 = 1040.2\ keV$. A Compton edge fit, as proposed by [33], was performed. The highest point in the spectrum around the edge was identified and the bin to the left of this point, which exhibited 70 % of the maximum count of the highest point, was allocated to the Compton edge.

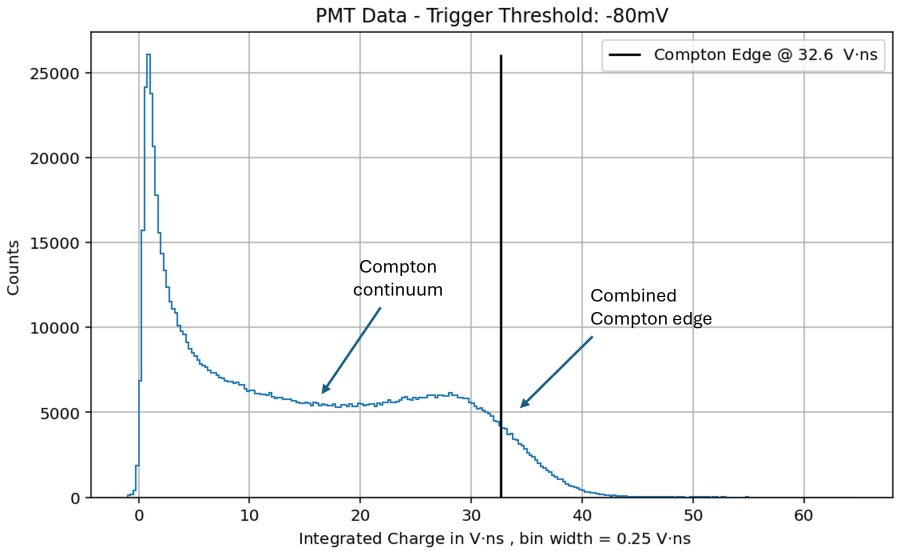

Figure 4.6: Spectrum of the PMT response to transparent LS (LAB+0.3 %PPO) inside the LS-fibre detector excited by a Co-60 gamma source. The trigger threshold on the Oscilloscope was set low, to -80 mV.

Chapter 5

Measurements

In this Chapter, the executed measurements are discussed. In total four measurements were performed in each opaque and transparent LS. In section 5.1, the used fibres and LS are presented. Section 5.2 is addressing the issue of compatibility between the performed runs. In the sections 5.3 and 5.4, the triggering, filtering and results of the measurements in transparent and opaque LS are discussed. After that follows the Conclusion section 5.5.

5.1 Samples

The goal of this thesis was to perform a relative comparison measurements between different OWLs and commercial Y11 fibres.

As previously discussed, the OWLs can be used directly inside the LS, but they must be protected from direct contact with the LS by a quartz tube, resulting in Bubo fibres. The Bubo fibres employed here consist of a 3 mm diameter quartz core OWL enclosed in a quartz tube with an inner diameter of 5 mm and an outer diameter of 6 mm. Four distinct OWLs were used in the study. Details on the paint layer used for the different OWL fibres can be found in table 5.1. In all cases, the paint matrix material was PEMA. The detailed composition of the paint can be found in table 5.2. A photo of the fibres under UV light is displayed in figure 5.1.

The two OWLs, designated Mars and Erde, have been coated with 14 μm or 24 μm of the BPEA-30 paint. The thickness of the paint was ascertained through the process of weighing the fibres prior to and following the coating process. This was then used in conjunction with the assumption of a homogeneous paint distribution around the fibres. The OWLs Uranus and Saturn were coated with 15 μm or 27 μm P64, a paint that contains P-Terphenyl and Bis-MSB. This paint was also utilised for the coating of the Wavelength-shifting Optical Modules (WOMs) deployed in the IceCube Upgrade. The excitation spectrum of P-Terphenyl is situated within the ultraviolet (UV) region, a vital

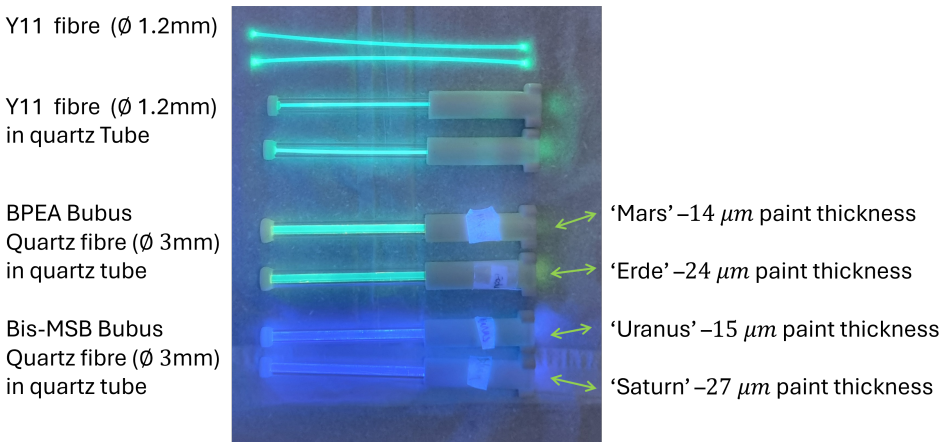

Figure 5.1: Display of the fibres used in the measurement under UV light (365 nm).

Fibre Name	Paint	Relevant WLS in Paint	Estimated Paint Thickness
Mars	BPEA-30	BPEA	14 μm
Erde	BPEA-30	BPEA	24 μm
Uranus	P64	Bis-MSB	15 μm
Saturn	P64	Bis-MSB	27 μm

Table 5.1: Details of the on the paint and applied paint thickness used on the OWL fibres.

Paint	Solvent	Matrix Material	1. WLS	2. WLS
BPEA-30	Toluol (70 %)	PEMA (30 %)	BPEA (2.33 mg/(g_{Matrix}))	-
P64	Toluol (75 %)	PEMA (25 %)	P-Terphenyl (10.7 mg/(g_{Matrix}))	Bis-MSB (5.85 g/(g_{Matrix})

Table 5.2: Composition of the paint used to produce the WLS fibres, the ratios are given in terms of mass percentage. The solvent evaporates after coating the fibre with the paint, leaving a PEMA matrix distributes with WLS molecules.

capture regime for the IceCube experiment. However, given that the LS used in this thesis emitted at wavelengths above 330 nm, the presence of P-Terphenyl in the P64 paint is not relevant for the capture of scintillation photons. Only the Bis-MSB in the paint contributes to this (see figure 5.2). These fibres will be referred to as Bis-MSB OWLs / Bubos.

The Y11 (Type YS-2MSJ) [34] fibres from Kuraray, with a diameter of 1.2 mm, were utilised for the comparison measurement. These fibres are multi cladded. The polystyrene core (n = 1.59) is impregnated with wavelength-shifting dye K27 at a concentration of 200 ppm. This dye absorbs in the blue region (the peak absorption is around 430 nm) and emits in the green region (the peak emission is around 470 nm). The detailed composition of the paint is not published, but the emission and excitation spectra look similar to that of BPEA (see figure 5.3).
The cladding comprises two layers: the inner layer is made from PMMA (n = 1.49) and the outer layer is made from a fluorinated polymer (n = 1.42). The double cladding thickness equals 4 % of the fibre diameter, while both layers have the same thickness, 2 % of the fibre diameter - hence 24 μm. According to the manufacturer, the Y11 fibres have a high light yield and a large attenuation length of approximately 3.5 m.

As can be seen from the photograph of the fibres under UV light (see figure 5.1), the Y11 and BPEA fibres emit green light, while the Bis-MSB fibres emit light in the blue region. The absorption spectra of the different WLS also cover different wavelength regions. To maximise the spectral overlap between LS emission and WLS absorption, two different LS were used. The spectra are shown in figures 5.2 and 5.3.

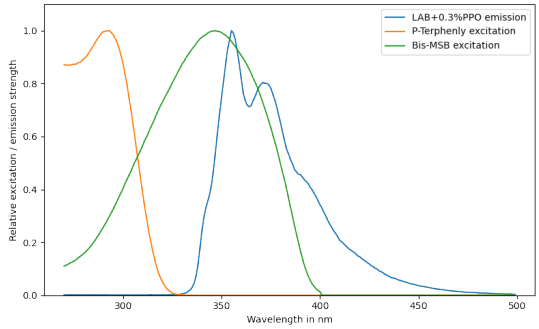

Figure 5.2: Emission spectrum of the LS composed of LAB and 0.3 % PPO, as well as the excitation spectra of the two WLS components in the P64 paint: P-Terphenyl and Bis-MSB.

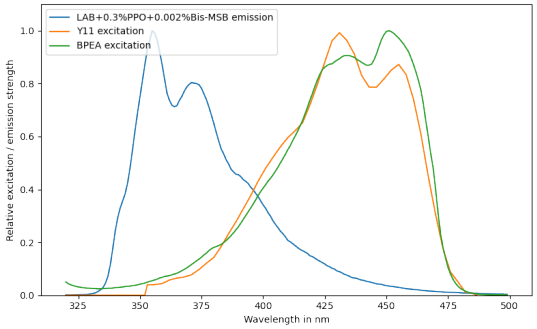

Figure 5.3: Emission spectrum of the LS made from LAB, 0.3 % PPO and 0.002 % Bis-MSB, as well as excitation spectra of BPEA and the Y11 paint K27 (this spectrum was taken from [34]).

A LS based on LAB with the addition of 0.3 % PPO emits in the violet region, which overlaps well with the absorption of Bis-MSB (see figure 5.4). The given percentage concentrations of the flours (and later waxes) must be understood as the mass fractions added on top to the 100 % mass of the solvent LAB. This LS was used for the measurements performed with the Bis-MSB Bubos. If Bis-MSB is added to this LAB + 0.3 % PPO cocktail at a concentration of 0.002 %, the LS emission is shifted to the blue region. As BPEA and K27 absorb in this region, they are used with this cocktail.

In the case of opaque LS, 3 % N,N′-Ethylenedi(stearamide) wax and 2 % Fischer-Tropsch wax are added to the transparent LS mixtures, resulting in an opaque liquid with a consistency similar to yogurt.

Overall, measurement runs with four different fibre pairs mounted in the LS-fibre detector were performed in each transparent and opaque LS. In one pair, the two Bis-MSB Bubos were used, in another the two BPEA Bubos. A further pair consisted of two Y11 fibres placed directly inside the LS. To assess the impact of the quartz tube, runs were conducted with two Y11 fibres, each enclosed in the same type quartz tubes (5 mm inner and 6 mm outer diameter) as the OWLs in the Bubos.

5.2 Considerations on Comparability and Expectations

When we compare different Bubos with each other and with the 'naked' and quartz tube-enclosed Y11, the question of compatibility arises. Although a relative comparison measurement can be performed despite the differences, considering the theoretical impact of different factors may provide insight into the underlying reasons for the results obtained. The following sections aim to describe these effects qualitatively.

5.2.1 Opacity of the Scintillator

Although the opacity does not directly affect the capture efficiency of the fibres, it influences the number of photons that encounter the fibre. The chance of TIR trapping scales with the number of photons that encounter the fibre. Considering the small size of the LS volume in the LS-fibre detector, in transparent LS all photons initially travelling towards the fibre will encounter it and have a chance of being captured. If they are not captured at this initial encounter, they are lost.

The opaque LS used still has a comparable light yield, but the scattering length has been reduced to a few millimetres. Therefore, it is less likely that photons created further away will make it to the fibre. However, nearby created photons actually have a higher chance of being trapped: firstly, due to the short scattering length, photons that initially travelled away from the fibre have a significant chance of being scattered in such a way that, after a few scatters, they still hit the fibre. Secondly, photons that hit the fibre but are not immediately trapped are not lost, as they may approach the fibre again after a few scatters.

5.2.2 Fibre Diameter

Assuming a uniform light flux, the number of photons that encounter the fibre is proportional to its projected cross-sectional on the lateral surface of the fibre, proportional to the fibre diameter times the fibre length. As the length of the fibre that is inside the LS volume is the same for all fibres equipped in the LS-fibre detector, only the diameter matters. Accordingly, larger-diameter fibres have a higher chance of being hit by a photon simply because of their size. However, the path length of a photon travelling inside the fibre until it reaches one end also increases with the diameter, thereby increasing the likelihood of attenuation inside the fibre. But this effect is expected to contribute less compared to the cross-sectional benefit.

5.2.3 Quartz Tube

As already discussed in section 4.2, the quartz tube has multiple effects. The air gap positively influences the TIR capture efficiency of the OWL due to the greater difference in refractive index between WLS paint and air. However, the presence of additional LS-tube and tube-air interfaces can also result in increased TIR and Fresnel losses. Consequently, the total number of photons that strike the OWL may decline. Furthermore, the reduction in active LS material is noteworthy, particularly given that the fibres are positioned on the backscatter path of the gammas in this proof of concept detector. This results in a greater proportion of energy being deposited outside the scintillator material, which reduces the scintillation output.

5.2.4 Differences between the OWLs

Absorption of Incident Photons in the WLS Paint

According to the Bouguer–Beer–Lambert law (Eq. 2.6), the absorbance of a material is proportional to the concentration of the absorbing component inside the material as well as the path length inside the material. Therefore the likelihood of an incident photon present in the WLS paint being absorbed by a WLS molecule is increased by a higher

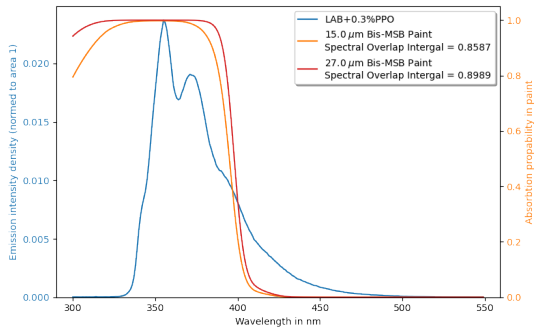

Figure 5.4: Emission spectrum of the LS made from LAB and 0.3 % PPO, as well as the absorption probability inside the Bis-MSB paint when coatings of 15 μm and 27 μm are applied.

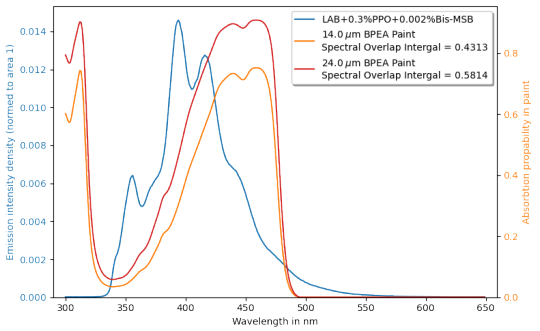

Figure 5.5: Emission spectrum of the LS made from LAB, 0.3 % PPO and 0.002 % Bis-MSB, as well as the absorption probability inside the BPEA paint when coatings of 14 μm and 24 μm are applied.

WLS concentration in the paint, as well as by a thicker paint layer, since the photon then travels a longer path through the paint. Furthermore, a greater spectral overlap between LS emission and WLS excitation increases the number of WLS-absorbed photons. Since the absorbed photons are emitted isotropically, the number of photons trapped inside the fibre is proportional to the number of photons absorbed by the WLS. This is therefore a crucial factor in determining the efficiency of the fibres. Since energy transfer occurs via real photons here, we can define a dimensionless spectral overlap integral, denoted by the symbol η, via

$$\eta = \int f(\lambda) \cdot P_{abs}(\lambda, l)\ d\lambda \quad , \tag{5.1}$$

where here $f(\lambda)$ is the normalised LS emission spectrum. $P_{abs}(\lambda, l)$ is the probability of a photon being absorbed in the WLS paint after travelling a distance of l within the paint:

$$P_{abs}(\lambda, l) = 1 - exp\left(-\frac{l}{\Lambda_{att}(\lambda)}\right) \ . \tag{5.2}$$

In the following, l has been chosen to equal twice the paint thickness. The attenuation lengths $\Lambda_{att}(\lambda)$ of the two paint types have been extracted from attenuation measurements [35] and were adjusted to the WLS concentrations present in the paints. As discussed in section 2.1, this attenuation length represents the sum of multiple attenuating components, i.e. 'normal' absorption, scattering and, in this case, WLS absorption. As the normal absorption and scattering lengths of the paint are primarily dependent on the PEMA matrix material and are of the order of metres, the main attenuation effect at short path lengths of twice the paint thickness is WLS absorption. Therefore, P_{abs} is approximately equal to the WLS absorption probability.
The spectra are shown in figures 5.4 and 5.5. The spectral overlap integral between LS emission and the absorption probability in the paint at given thicknesses are summarized in table 5.3.

As it can be seen in figure 5.4, the concentration of the Bis-MSB is sufficiently high, therefore close to 100 % absorbance over the whole Bis-MSB excitation range is reached independent on the paint thickness. Therefore the values of the spectral overlap are quite similar, even though the thicker paint has a slight benefit. The concentration of BPEA is

LS	WLS in Paint	Paint Thickness	η
LAB + 0.3 % PPO	Bis-MSB	15 μm	0.8587
LAB + 0.3 % PPO	Bis-MSB	27 μm	0.8989
LAB + 0.3 % PPO + 0.002 % Bis-MSB	BPEA	14 μm	0.4313
LAB + 0.3 % PPO + 0.002 % Bis-MSB	BPEA	24 μm	0.5814

Table 5.3: Summary of the spectral overlap integral η in between different LS and WLS paints.

not high enough to reach 100 % absorbance over the whole excitation range and therefore one can see a stronger dependence on the paint thickness in the overlap integral.
Due to the approximately 1.2 to 2 fold increase in the value of the spectral overlap integral η at same path length l between Bis-MSB and BPEA with the corresponding LS cocktail, the Bis-MSB Bubos should perform best and approximately similar. A difference in performance due to the thickness might be observable between the BPEA Bubos.

Reabsorption within the WLS Paint

However, thicker paint and higher WLS concentrations also increase the likelihood of a trapped photon being reabsorbed by a WLS molecule. This photon would then be emitted isotropically and potentially lost again for the same reason.

The probability of reabsorption is related to the intrinsic spectral overlap between the WLS emission spectra and the absorption probability in the paint. Table 5.4 shows the "intrinsic" spectral overlap integrals from the spectra displayed in figures 5.6 and 5.7. At similar path length, hence similar paint thicknesses, BPEA shows a roughly 1.5 factor higher chance of reabsorption, which further enhances the expected superiority of Bis-MSB fibres.

WLS in Paint	Paint Thickness	η
Bis-MSB	15 μm	0.1621
Bis-MSB	27 μm	0.2084
BPEA	14 μm	0.2806
BPEA	24 μm	0.3607

Table 5.4: Summary of the "intrinsic" spectral overlap integral η inside different WLS paint layers.

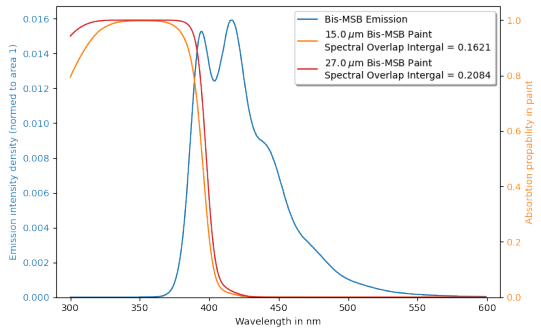

Figure 5.6: Emission spectrum of Bis-MSB as well as the absorption probability inside the Bis-MSB paint when coatings of 15 μm and 27 μm are applied.

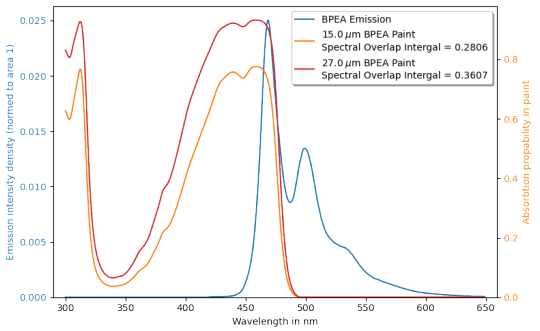

Figure 5.7: Emission spectrum of BPEA as well as the absorption probability inside the BPEA paint when coatings of 14 μm and 24 μm are applied.

5.2.5 SiPM Detection Efficiency

The SiPM detection efficiency is not constant across the entire sensitive wavelength region. Overlaying the WLS emission spectra of all the used WLS with the spectral detection efficiency and calculating the spectral overlap integral provides insight into the possible advantages. As can be seen from figure 5.8 even though the WLS emission spectra peak at different wavelengths, the overall spectral overlap integrates to a similar value. No significant advantage can be noted.

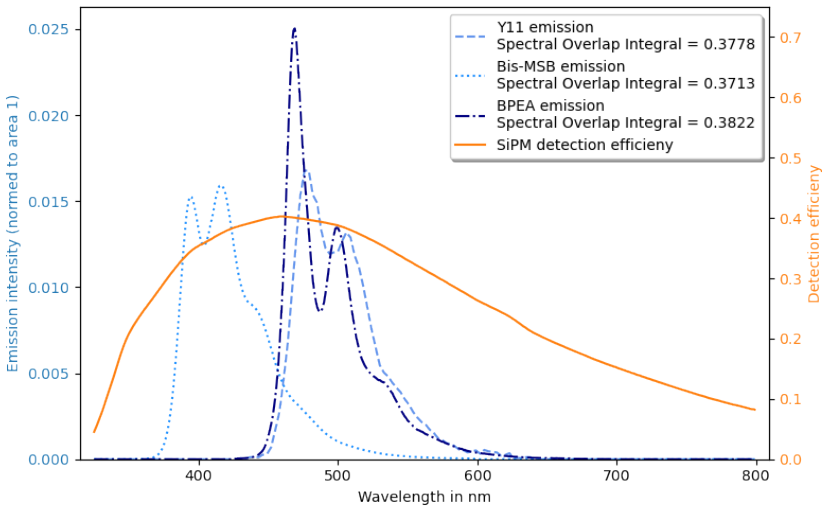

Figure 5.8: Display of the measured emission spectra of Bis-MSB and BPEA dissolved in Cyclohexane. The emission spectra of Y11 dye K27 was extracted from [34]. Alongside, the SiPM detection efficiency curve, extracted from [36], is shown.

5.2.6 Surface Quality, Materials and WLS Positioning

The photons detected in the SiPMs are the result of successful photon trapping and undisturbed transport via consequential TIR towards the fibre ends. As discussed in section 2.7.1, for the TIR efficiency a larger difference in refractive indices at the interfaces, as well as WLS emission closer to the fibre surface, is beneficial. Furthermore, for

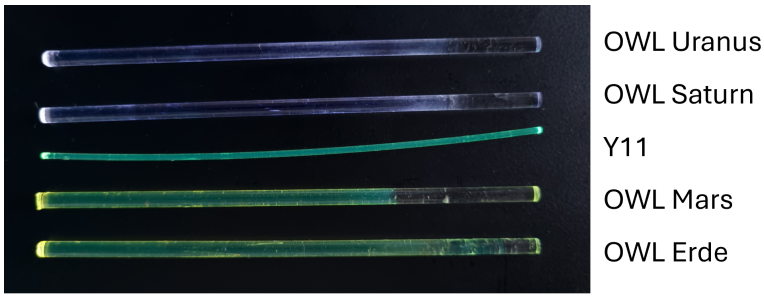

Figure 5.9: Photo of the OWLs and a Y11 fibre in daylight to show the surface qualities.

successful piping of the photons along the fibre via consequential TIR, homogeneous and scratch-free interfaces and surfaces are important, as this reduces scattering losses.

As the Y11 fibres are commercially available double cladded WLS fibres, it is reasonable to assume that they are already optimised in terms of material composition, cladding thickness and interface quality. The double cladding serves two purposes. Firstly, it protects the underlying interfaces from external influences. Secondly, as the WLS emission takes place inside the core, the consequential ordering of materials with refractive indices that decrease gradually towards the outside creates three interfaces at which TIR can occur. This enlarges the effective TIR capture angle of the fibre. Further due to the large jumps in refractive index from Polystyrene (n = 1.59) to PMMA (n = 1.49) to the outermost layer of fluorinated polymer (n = 1.42), a lot of photons are already captured at the two inner interfaces and the fraction of cladding rays is lower.

The strength of the OWLs lies in the presence of the WLS on the outside of the fibre, as this arrangement is beneficial for the capture fraction (see section 2.7.2). However, as the WLS process happens in the paint, the only TIR-capable interface is the paint-air interface. Even if the OWL core was made from a higher refracting material as the paint, TIR could not happen at the core-paint interface as the WLS shifted photons originate from the paint layer. This makes all captured photons cladding rays. Those are prone to attenuation, as this outermost interface is usually of poorer quality as it has no protection and is more prone to scratches and surface inhomogeneities. Further, the "additional", not to TIR contributing core - paint interface provides another opportunity for scattering on inhomogeneities that could result in photon loss.

Looking at the photo displayed in figure 5.9, one can clearly see more scratches and inhomogeneities on the surfaces of the OWL prototypes in comparison to the Y11 fibre.

5.2.7 Expectations

Based on the analysis of the differences between the Bis-MSB and BPEA Bubos, the two Bis-MSB Bubos should perform best with only a small difference between them. Differences in paint thickness might be visible between the BPEA fibres, the thicker coated one is expected to perform better.

Guessing the relative performance of Y11s compared to OWLs is more difficult. The OWLs clearly benefit from their 3 mm diameter, which is significantly larger than that of the 1.2 mm Y11s. As the projection cross-section area scales with the diameter, there

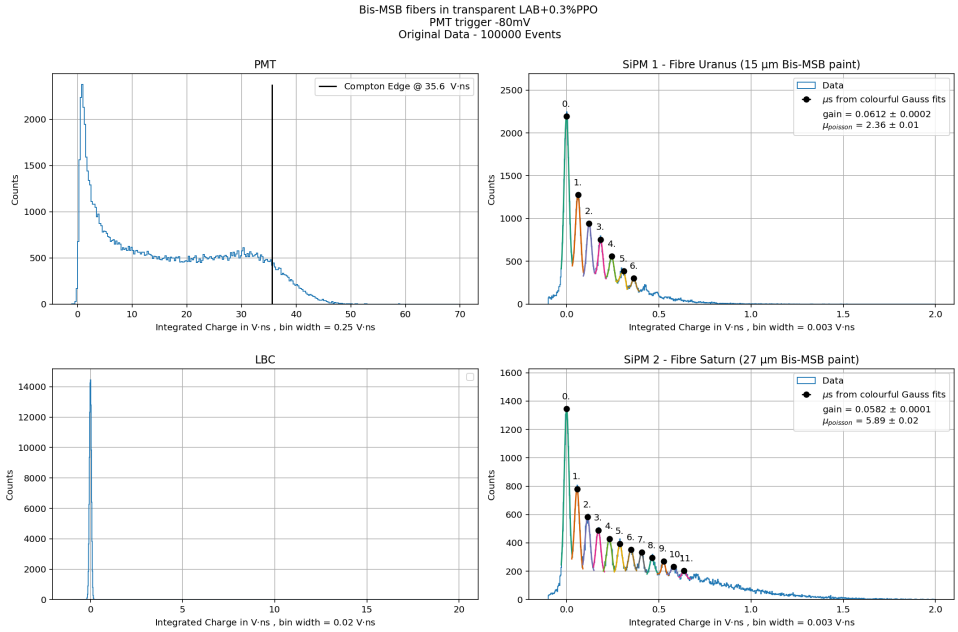

Figure 5.10: Overview of the intergraded charge histograms obtained with the Bis-MSB Bubos emersed in transparent LAB + 0.3 % PPO. The trigger was set to the PMT signal, the threshold was -80 mV.

should be a 2.5-fold increase in the likelihood of a photon hitting the fibre. However, in terms of surface quality and TIR maximisation, the Y11s clearly lead.

5.3 Runs in Transparent LS

5.3.1 Triggering and Event Selection

In this section, the triggering of the measurements runs with fibres in transparent LS as well as the data processing are discussed. The data of run with Bis-MSB Bubos inside transparent LAB + 0.3 % PPO is displayed as an example.

As discussed in Chapter 4, the LBC is utilised as a backscatter detector to filter events where gamma backscattering occurs within the LS-fibre detector. The events in question are located at the Compton edge of the LS inside the LS-fibre detector. As the Compton spectrum exhibits subtle variations between different runs with different LS and fibres prior to the initiation of the actual backscatter measurement, the Co-60 spectrum was recorded by triggering on PMT signals that exceeded a threshold of -80 mV. As outlined in Section 4.4.2, a Compton edge fit was performed. As illustrated in Figure 5.10, the charges of all four channels are displayed, derived from the integration over the recorded signals when this low PMT trigger is set.

The SiPM spectrum displays multiple peaks, which are referred to as fingers. The finger spectrum of an ideal, noise free SiPM would show a series of discrete fingers, with no overlap and a Poisson distribution centred around the mean photon count value, denoted as m in the Poisson distribution. The peaks are distributed at equidistant intervals, with the distance being determined by the applied gain. However, crosstalk and after-pulsing have been shown to cause excess noise, resulting in a deviation from the Poisson shape

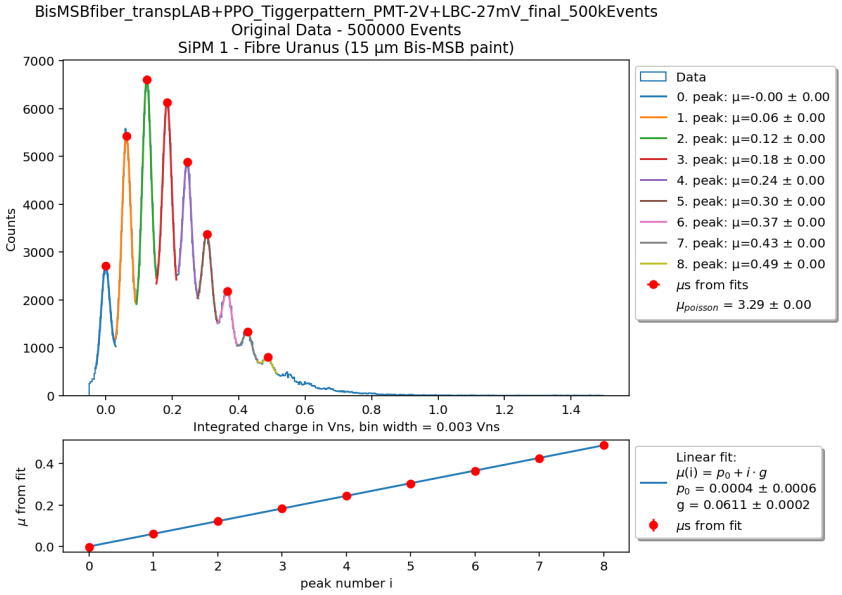

Figure 5.11: Display for the procedure to figure out the gain of the SiPM. The upper plot shows a finger spectrum obtained during one of the measurements. To each finger, a gauss function with linear background is fitted. The lower plot shows the peak number vs the fit value of μ. The relation is linear, the slope is equal to the gain g.

[37]. Electronic noise, gain fluctuations between individual microcells, pulse shape effects in combination with cross-talk, after pulsing and dark counts can broaden the fingers to the point where they overlap and eventually become unresolvable.
The used SiPMs seem to be prone to noise, as the fingers are overlapping and the envelope of the peaks falls slower than an Poisson shaped distribution would. This is not surprising, as the utilized SiPMs contain over 14.000 pixels and the dark count rate is therefore high. The evaluation of the mean photon counts, denoted by $\mu_{Poisson}$, was conducted through the following procedure:
Initially, an automated function was employed to identify all prominent finger peaks within the spectrum. Subsequently, a Gaussian function with a linear background is fitted to each finger that has been identified. The μs of each peak are used to ascertain the gain of the SiPM, as the peak number i and the μ_i are linearly related. This is exemplarily shown in figure 5.11. In the overview plots, the gain curves are not shown but the fitted gain can be found in the legend. With the help of the gain and the arithmetic mean $< charge >$ of the charge distribution, the expectation value of the Poisson distribution $\mu_{poisson}$ can be calculated via:

$$\mu_{poisson} = \frac{< charge >}{gain(1 + crosstalk\ probability)} \quad . \tag{5.3}$$

The crosstalk probability was extracted from the SiPMs data sheet [36] and equals about 5 % at 3 V over voltage.

In the backscatter measurements, a trigger pattern looking for coincidental PMT signals exceeding -2 V and LBC signals above -27 mV was applied in the Oscilloscope. The PMT threshold has proven to be close to the Compton edge, reducing the recording of unnecessary events, as can be seen in figure 5.12. As this selects those events where a lot of light was produced inside the LS-fibre detector, a shift in the SiPM finger spectrum is visible, resulting in greater $\mu_{poisson}$. As we now trigger on the LBC in coincidence,

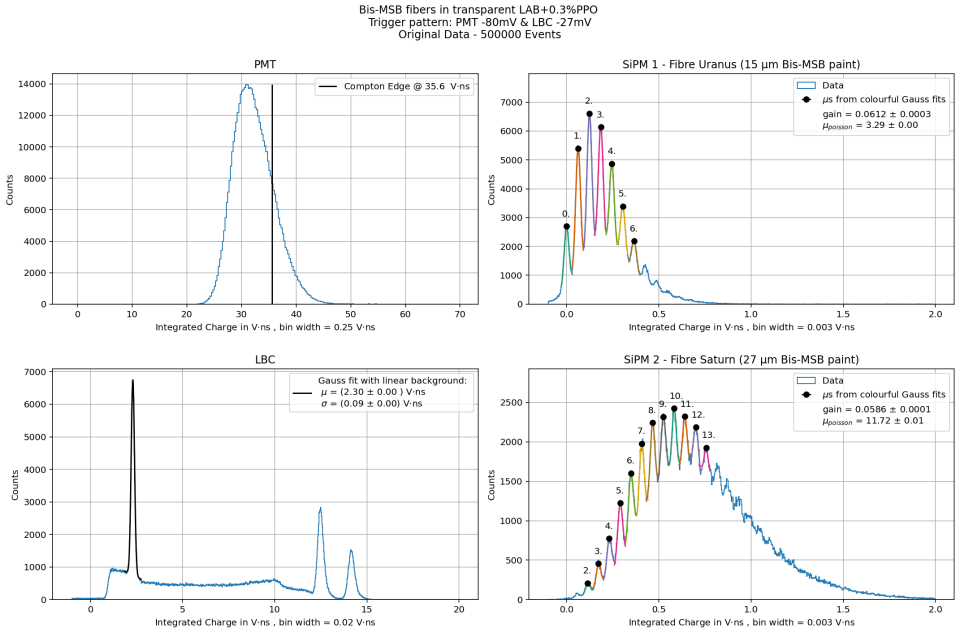

Figure 5.12: Overview of the integrated charge histograms obtained with the Bis-MSB Bubos emersed in transparent LAB + 0.3 % PPO. A trigger pattern looking for simultaneously excess of threshold of -2 V in the PMT signal and -27 mV in the LBC signal.

the full Co-60 spectrum is visible in the LBC. In comparison to the "pure" LBC Co-60 spectrum in figure 4.5, it is noticeable that the backscatter peak is more prominent. A Gaussian with linear background was fitted to the peak region. That fact that the full Co-60 spectrum is still visible after employing the coincidence triggering setting shows that a lot of random coincidences are also recorded due to the high activity of the gamma source. In the offline data processing, the events with a LBC charge lying within the 2σ interval of the backscatter gauss fit are cut out. This data is considered to arise from true backscatter events. As displayed in figure 5.13, this has a slight shift in the finger plots to greater expectation values as consequence.
For the final backscatter measurements, four days of data taking yielded about 500 000 triggered events. After applying the backscatter LBC cut, about 70 000 events survived.

5.3.2 Results

The measurements and data processing were performed in the same manner as explained in the previous section. The $\mu_{poisson}$ results of the selected backscatter events are summarised in table 5.5. The plots of the other measurements can be found in Appendix C.1 - C.3. From the measurement runs performed with identical fibres, we can learn that they may yield a similar $\mu_{poisson}$, but this is not always the case, hence unprotected Y11. Further the fibre position inside the LS-fibre sample might have an influence. As the second fibre is placed behind the first one in regard to the gammas back-scatter line, different amounts of light might reach the individual fibres due to geometry reasons. But this hypothesis can't be confidently confirmed. Therefore on top of the errors given from the fits displayed in the tables, a systematic adjustment and positioning uncertainty from 10 % will be granted.

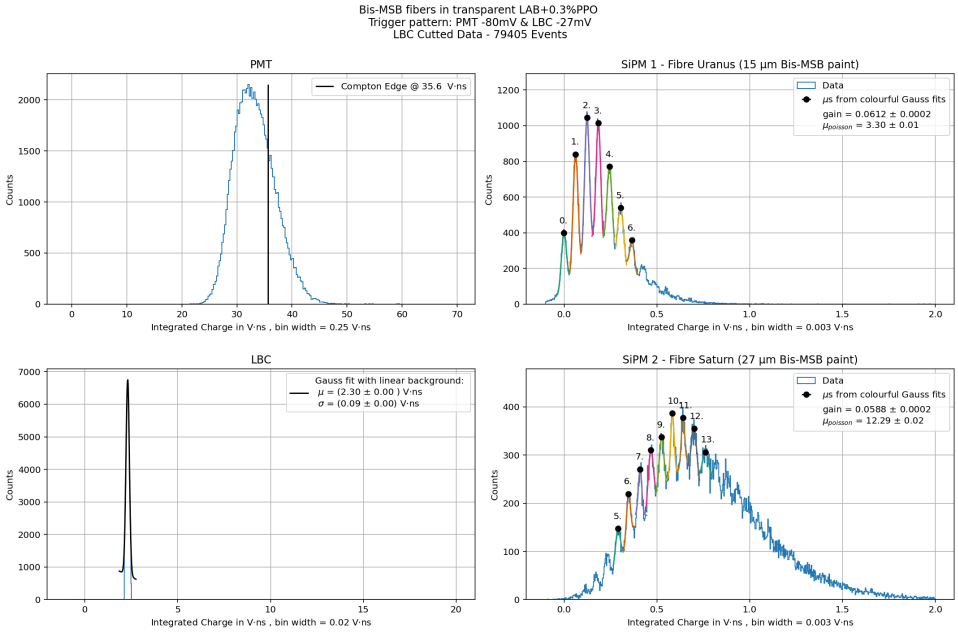

Figure 5.13: Overview of the intergraded charge histograms obtained with the Bis-MSB Bubos emersed in transparent LAB + 0.3 % PPO. A trigger pattern looking for simultaneously excess of threshold of -2 V in the PMT signal and -27 mV in the LBC signal. In addition an offline cut the the 2σ region of the Gauss fitted to the LBC backscatter peak was applied.

Fibre on SiPM 1 1	$\mu_{poisson}$	Fibre on SiPM 2	$\mu_{poisson}$	Averaged $\mu_{poisson}$
Uranus Bubo	3.30 ± 0.00	Saturn Bubo	12.29 ± 0.02	-
Mars Bubo	3.28 ± 0.01	Erde bubo	4.82 ± 0.01	-
Y11 fibre	8.86 ± 0.02	Y11 fibre	9.44 ± 0.02	9.15 ± 0.29
QT enclosed Y11	7.25 ± 0.01	QT enclosed Y11	7.24 ± 0.01	7.25 ± 0.01

Table 5.5: Mean detected photon count $\mu_{poisson}$ results of the measurement obtained in coincidental triggering pattern when the LBC cut is applied on top.

The most light is captured with the Saturn Bubo as the mean detected photon count is 12.29. Next come the "naked" Y11 fibres with about a quatre lower $\mu_{poisson}$ value. Then the quartz tube (QT) enclosed Y11 fibres with 7.25 ± 0.01. The other Bubos are the tail lights. Puzzlingly, there is a factor of around 4 discrepancy between the two Bis-MSB fibres Uranus and Saturn. The BPEA fibers perform worse than the Bis-MSB fibre considered at similar paint thicknesses. Further, a dependance on paint thickness between the BPEA fibres is visible. As expected the thicker coated Erde Bubo leads between those. Considering the effect of the QT in transparent LS it can be noted that they seem to have a negative effect in transparent LS, as the "naked" Y11s see on average more than one photon more then the enclosed Y11s.

The same overall behaviour can also be extracted from the measurements taken with a low PMT trigger threshold. As can be seen from table 5.6, the Bubo Saturn performs the best, followed by the naked Y11, then the QT enclosed Y11 and last come the other Bubos. The large discrepancy between the Bis-MSB Bubos, the negative effect of the QT on the Y11 efficiency as well as the BPEA thickness dependence remain. Cosnsequently,

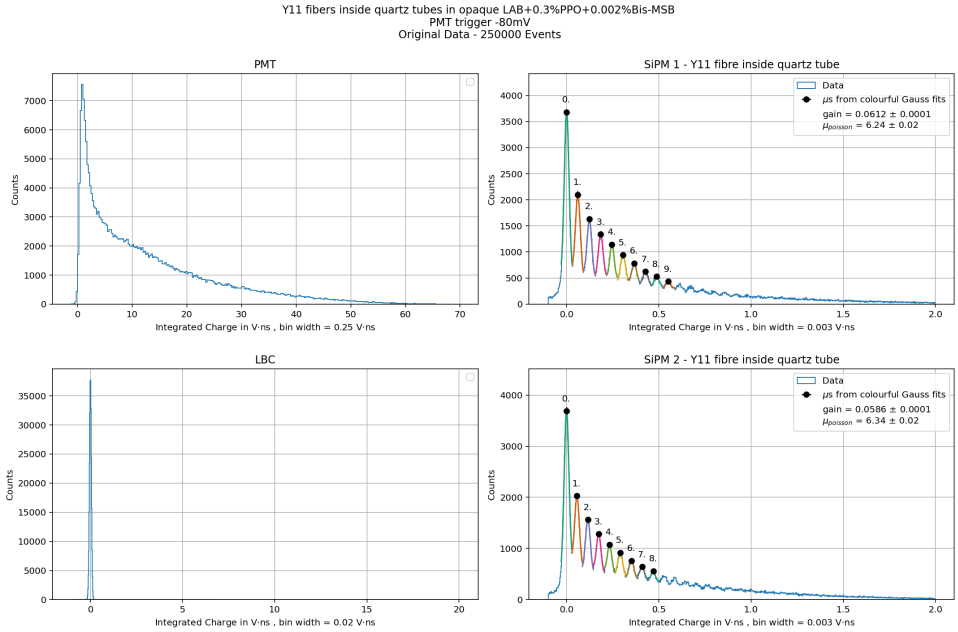

Figure 5.14: Overview of the intergraded charge histograms obtained with the QT enclosed Y11 fibres emersed in opaque LAB + 0.3 % PPO +0.002 % Bis-MSB. The trigger was set to the PMT signal, the threshold was -80 mV.

these measurements can't be used to obtain a reasonable number for the light yield, but they already give a hint at which fibre candidates look promising. As this measurements only take about 5 minutes, keeping this method in the back mind might save some time in the future when multiple Bubo prototypes are tested.

Fibre on SiPM 1	$\mu_{poisson}$	Fibre on SiPM 2	$\mu_{poisson}$	Averaged $\mu_{poisson}$
Uranus Bubo	2.36 ± 0.01	Saturn Bubo	5.89 ± 0.02	-
Mars Bubo	1.67 ± 0.01	Erde Bubo	2.18 ± 0.01	-
Y11 fibre	4.19 ± 0.01	Y11 fibre	4.32 ± 0.01	4.26 ± 0.07
QT enclosed Y11	3.60 ± 0.01	QT enclosed Y11	3.44± 0.01	3.52 ± 0.08

Table 5.6: Mean detected photon count $\mu_{poisson}$ results of the measurement obtained by setting a trigger threshold of -80 mV to the PMT signal.

5.4 Runs in Opaque LS

5.4.1 Triggering and Event Selection

The original idea was to apply the same trigger procedure to the opaque LS measurement runs as to the transparent LS runs, but this has been proven to not be possible. Figure 5.14 shows the first run performed while triggering on the same low PMT threshold (-80 mV). Eminently, no Compton edge is visible. The local confinement of light due to the opacity is evidently very efficient, the photons can't spread throughout the few centimetres of the LS volume and the homogenous light flux onto the PMT is suppressed. This has a large impact on the possibility of filtering for the true backscatter events, as only applying the LBC backscattered hits is not sufficient and without a Compton edge,

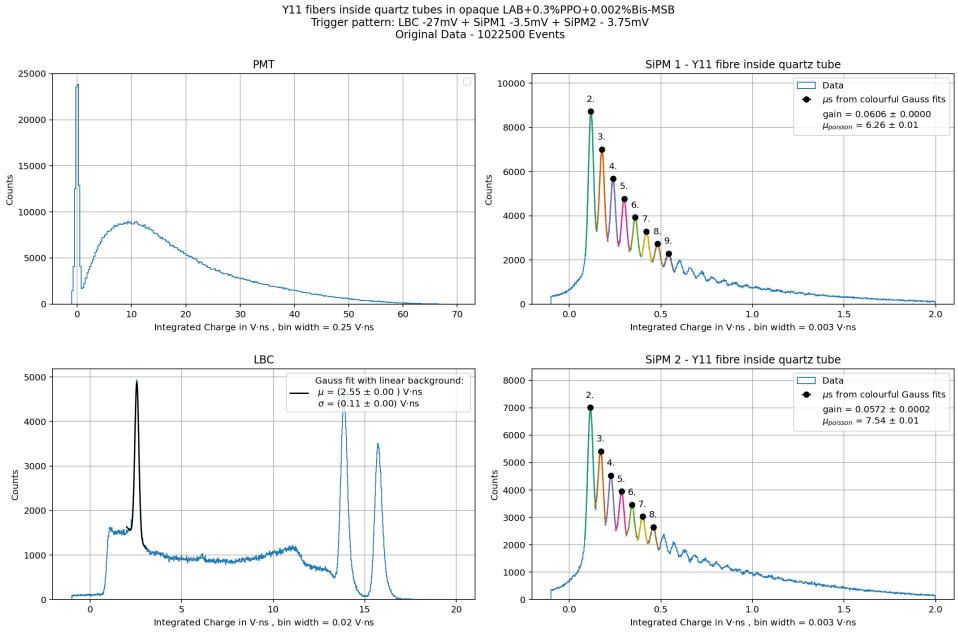

Figure 5.15: Overview of the intergraded charge histograms obtained with the QT enclosed Y11 fibres emersed in opaque LAB + 0.3 % PPO +0.002 % Bis-MSB. The trigger was set on a coincidence pattern, the thresholds for the channels were: LBC -27 mV, SiPM 1 -3.5 mV & SiPM 2. -3.75 mV. In addition a LBC backscatter cut was applied.

one can hardly define a justified PMT triggering threshold.

In the aim of performing a quantitive light yield measurement, another approach in finding the backscatter events was taken: a trigger pattern looking for coincidental exceedance of the following thresholds: LBC -27 mV, Fibre on SiPM 1 – 3.5 mV and SiPM2 -3.75 mV. The SiPM thresholds were chosen such, that each must see more than one photon. The threshold of SiPM2 was purposely set higher, as the gain of this SiPM has been proven to be a bit higher. With the coincidental SiPM signal it should be ensured, to trigger on events that deposited a large amount of energy causing the creation of a large amount of light in between both SiPMs. Figure 5.15 shows the examinatorial histograms obtained with this method. The two photo absorption peaks are nearly as high as the backscatter peak. This shows that this trigger setting is not as effective in filtering for true backscatter events compared to the trigger pattern used in transparent LS. To this data then again the LBC backscatter cut was applied (see figure 5.16).

A drawback of this triggering approach is that the triggering rate was highly dependent on the fibres used. As seen in the previous section, the mean photon count varies strongly between fibres. The measurements were taken over 3.5 days, but the obtained data quantity varies strongly. The individual pairing of the fibres also has an influence as the Bubo pairs do not contain identical fibres. Further, as the finger spectrum does not start by the 0^{th} peak, the method of evaluating the mean photon count $\mu_{poisson}$ does not give the "true" mean as the applied trigger thresholds offsets the finger spectrum. Since the thresholds and SiPM gains are different, one can only compare the offsetted "$\mu_{poisson}$" values for each SiPM separately.

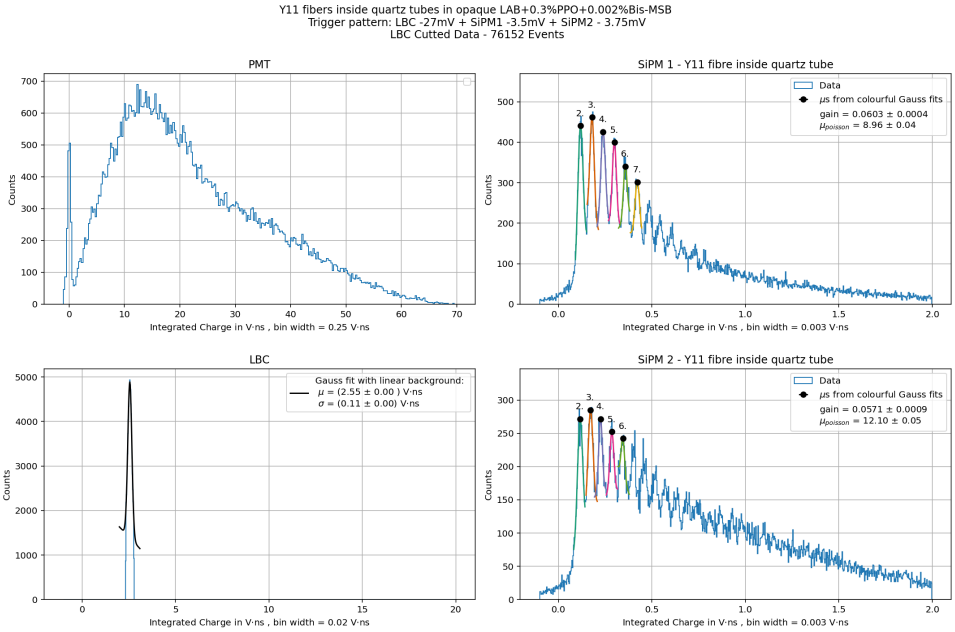

Figure 5.16: Overview of the intergraded charge histograms obtained with the QT enclosed Y11 fibres emersed in opaque LAB + 0.3 % PPO +0.002 % Bis-MSB. The trigger was set on a coincidence pattern, the thresholds for the channels were: LBC -27 mV, SiPM 1 -3.5 mV & SiPM 2. -3.75 mV. In addition a LBC backscatter cut was applied.

5.4.2 Results

Even though no Compton edge is visible, a successful PMT trigger can still be used as an indication that a Compton scatter has occurred inside the LS, allowing one to observe how the different fibres perform. Table 5.7 shows the results. The plots of the other measurement runs can be found in Appendix C.4-C.6.
Firstly, the mean photon count detected by all fibres is higher than in the transparent LS measurement. Due to the opacity of the LS, photons that are not captured on their first approach to the fibre can be scattered and redirected onto the fibre, providing another opportunity for them to be trapped. The Saturn fibre leads again, followed by the Y11 fibres with and without the tube. Interestingly, the difference between the results of the Y11 inside the QT and the Y11 immersed directly inside the LS is smaller in opaque LS. Looking at the values, it seems that the tube housing is beneficial, but as this effect is below the 10 % adjustment error, it may be just by chance. The significant discrepancy between the Bis-MSB Bubos remains. Notably, the thinner BPEA-coated Mars Bubo slightly outperforms its sibling, the Erde.

Fibre on SiPM 1	$\mu_{poisson}$	Fibre on SiPM 2	$\mu_{poisson}$	Averaged $\mu_{poisson}$
Uranus Bubo	3.25 ± 0.01	Saturn Bubo	7.21 ± 0.01	-
Mars Bubo	2.61 ± 0.01	Erde bubo	2.18 ± 0.01	-
Y11 fibre	6.15 ± 0.02	Y11 fibre	6.26 ± 0.02	6.02 ± 0.06
QT enclosed Y11	6.24 ± 0.02	QT enclosed Y11	6.34 ± 0.02	6.29 ± 0.05

Table 5.7: Results of the measurement obtained by applying a PMT trigger threshold of -80 mV. All measurements were performed in opaque LS.

Fibre on SiPM 1	$\mu_{poisson}$	Fibre on SiPM 2	$\mu_{poisson}$
Uranus Bubo	7.47± 0.03	Saturn Bubo	13.73 ± 0.06
Mars Bubo	6.23 ± 0.02	Erde Bubo	5.98 ± 0.02
Y11 fibre	10.80 ± 0.04	Y11 fibre	12.24 ± 0.04
QT enclosed Y11	8.96 ± 0.04	QT enclosed Y11	12.1 ± 0.05

Table 5.8: Results of the measurement obtained with the coincidental triggering pattern (containing the following thresholds: LBC -27 mV, SiPM1 -3.5 mV & SiPM2 - 3.75 mV) when the LBC cut is applied on top. All measurements were performed in opaque LS.

The results of the measurements conducted in pursuit of backscatter events are displayed in table 5.8. As previously discussed, the comparison between the fibres mounted to different SiPMs is not fair. Furthermore, the displayed values of the $\mu_{Poisson}$ distribution are artificially elevated by the application of trigger thresholds to the SiPM signals, rendering them unsuitable for direct comparison with the values obtained in other measurements. This measurement may only be suitable to indicate performance trends between the fibres.
From the fibres that were connected to SiPM 1, the Y11 fibre leads over the QT enclosed Y11 fibre, even after considering a 10 % adjustment error. Slightly worse is the Bis-MSB Bubo Uranus. The BPEA Bubo Mars comes last. Looking at SiPM 2: The Bis-MSB Bubo Saturn leads again. Shortly followed by the Y11 fibres with and without tube, here there is no significant difference visible. The BPEA Bubo only sees less than half the light.

5.5 Conclusion

Overall, the measurements showed that in a relative comparison one Bubo candidate, the Bis-MSB Bubo Saturn, was capable of outperforming the Y11 fibres. However, due to differences in diameter and spectral overlap between the LS and WLS used, this advantage cannot be attributed to an increase in TIR capture efficiency.
The spectral overlap of the LS and WLS used is similar for the Y11 and BPEA Bubos, so a fair comparison is possible between them. Despite their diameter advantage, the BPEA Bubos fall far behind. As expected, the BPEA Bubos performed worse than the Bis-MSB Bubos; however, the Bis-MSB Bubo Uranus falling behind its sibling Saturn is puzzling. This could indicate that the paint thickness evaluation is inaccurate and/or that there are significant fluctuations in paint quality and/or surface homogeneity, which calls the coating method into question.
The opacity of the LS appears to benefit fibre capture. The influence of the quartz tube appears to depend on whether transparent or opaque LS is used. Regarding the latter, opacity suggests a negative effect.

In general, a few trends could be derived from the comparison measurements performed, but it would be wise to manufacture and test more Bubo prototypes of the same type to make more reliable statements.

Chapter 6
Simulations

In order to gain a more nuanced understanding of the capture efficiency in different OWL constellations, Geant4 (version 11.3.2) simulations were implemented. Geant4 is a tool developed at CERN that is designed to simulate the propagation of particles through matter.
In the created simulations, the optical photon's propagation through the different materials is modelled, accounting for Rayleigh scattering and absorption. The optical properties (i.e. refractive index, scattering and absorption length) of the various materials present in the LS-fibre detector were set to constant values that correspond to real-life scenarios. Absorbance and emission measurements of the LSs and WLS paints utilised in the experimental setup (see section 5.2) were employed to specify the scintillating and WLS properties of the equivalents within the simulation.

In one Simulation, the LS-fibre detector was implemented. In order to replicate the measurements, the four OWLs and the two different LS cocktails were implemented. The gammas were shot along the backscatter axis of the real experiment. Another simulation involved a single OWL fibre in air that was shot with photons. A range of combinations of core and paint matrix materials were implemented and then subjected to comparative analysis.

6.1 LS-fibre Detector Simulation

Figure 6.1 shows the visualisation of the implementation of the LS-fibre detector in Geant4. The dimensions of the implemented features correspond to the dimensions of the real setup.
The surface of the reflective foil and the PTFE housing were rendered 100 % diffuse reflective. It was established that all material boundaries were to be set as ideal, perfectly smooth (polished) dielectric–dielectric interface interfaces. The boundary process is governed by the Fresnel equations.
Photons are deleted (i) upon their detection by one of the photon detectors or (ii) upon their departure from the detector over the windowed sides. The following presentation contains detection rates which are not commensurate with real detection rates; they merely resemble the interaction of a photon with the detection area, without accounting for factors such as detection efficiencies or electronic noise.
Gammas were created through the use of a particle gun, with the gun positioned at a fixed point and directed towards the centre of the LS sample. Via fair random sampling an energy of 1173 or 1332 keV was assigned to the gammas, as those values correspond to the Co-60 emitted gamma energies.
In consideration of the minimal probability of 180° backscatter, the implementation of a backscatter sample was deemed unnecessary. Consequently, all events resulting in the detection of more than 15 photons by the PMT were retained for further analysis. This aims to replicate the measurements recorded at low PMT thresholds.

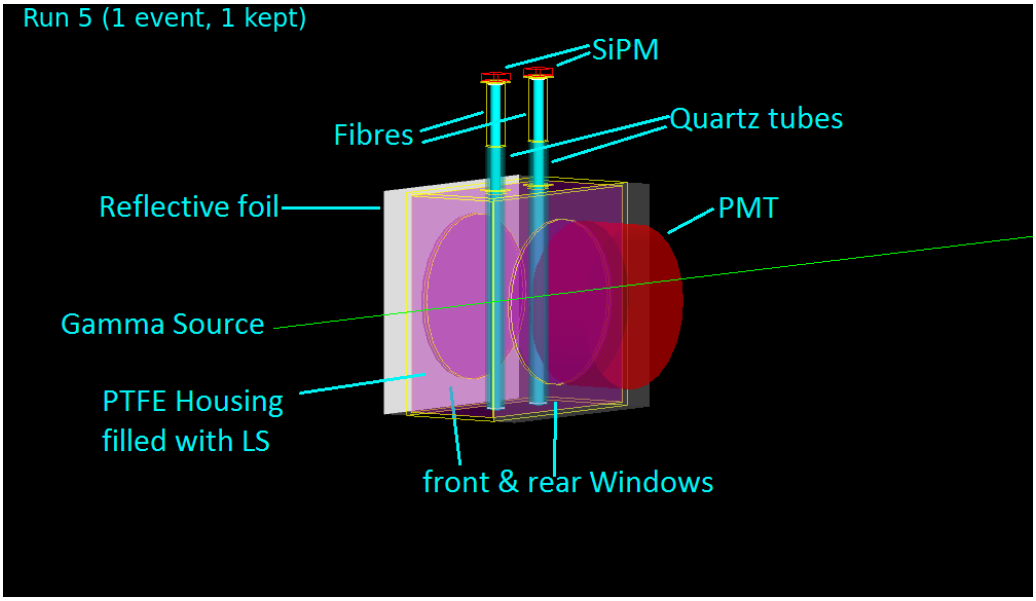

Figure 6.1: Visualisation of the proof of concept detector implemented in the Geant4 Simulation. All parts that have been previously described in chapter 4 and are shown and labeled correspondingly. The left appearing SiPM is numbered by 1, the right one as 2. The simulation of one gamma passing through the LS without interaction is visible.

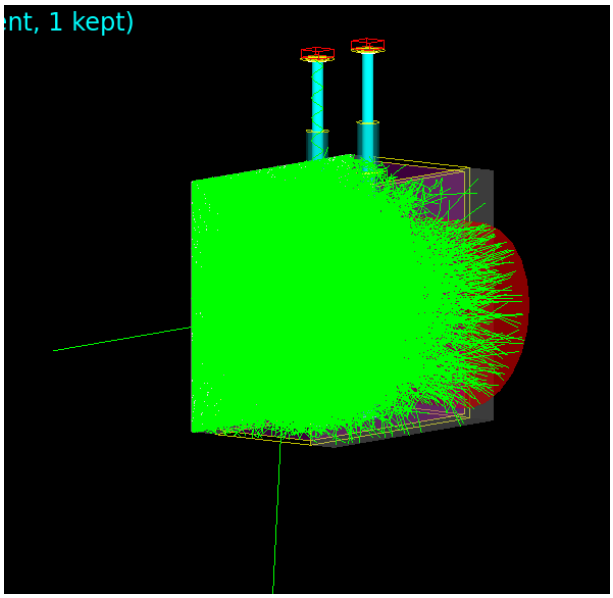

Figure 6.2: Simulation of a gamma interacting inside the LS-fibre detector. The light green lines represent optical photon and gamma tracks. One optical photon reaches the left SiPM.

LS "phase"	Averaged hits on	Uranus Bubo $15\mu m$,Bis-MSB	Saturn Bubo $27\mu m$,Bis-MSB	Mars Bubo $14\mu m$,BPEA	Erde $24\mu m$,BPEA
T	SiPM 1	13.03%	13.00%	7.56%	7.33%
T	SiPM 2	14.53%	14.50%	8.21%	8.18%
O	SiPM 1	0.59%	0.60 %	0.28%	0.27%
O	SiPM 2	0.57%	0.60%	0.28%	0.29%

Table 6.1: Display of the averaged SiPM hit number obtained in the simulations of the different Bubos in different transparent (T) and opaque (O) LS cocktails.

Figure 6.2 shows a Compton scatter event. The high light yield assigned to the LS, which is 9000 photons/MeV, results in the creation of a substantial quantity of scintillation photons. The mean number of scintillation photons and Cherenkov photons created is approximately 6000 and 150 respectively. The majority of gamma interactions take place within the quartz tubes or fibres, given that quartz contains higher-Z atoms in comparison to the LS.

The distinction between the implemented transparent and opaque LSs is realised via the implementation of disparate scattering lengths. The scattering length was set to 1.6 mm for the opaque and 20 m for the transparent LS version. The absorption length was set to 2 m in all cases. In addition, the transparent LS consists entirely of LAB, while the opaque LS contains 98 % LAB and 2 % paraffin wax. As the WLS are only dissolved in sub-percent levels, the mechanical material contributions of these substances were neglected, but not their optical contributions.
The implemented Bubos were composed of quartz tubes with an inner diameter of 5 mm and an outer diameter of 6 mm. The inserted OWLs were composed of quartz tubes with 3 mm diameter coated with PMMA-based paint. Paints containing Bis-MSB or BPEA were implemented and assigned varying thicknesses in order to resemble the prototypes. The Bis-MSB paint utilised in the simulation exhibits slight variations in comparison to the P64 paint, as the P-Terphenyl component was neglected.

The objective of this simulation is to examine the SiPM hits in the same LS-Bubo combinations as were utilised in the actual measurements. In the simulations pertaining to transparent LS, 2 million gammas were created. Conversely, in the simulations concerning opaque LS, only 1 million gammas were created, as the propagation of photons in opaque material is computationally expensive. In approximately 30 % of cases, a gamma interaction was observed within the LS sample. The Bubo pairs of different OWLs being utilised, are not considered in the present simulation. In all runs identical OWLs were put into pairs. The results are summarised in table 6.1. In exceptional cases, up to seven photons have been detected in SiPMs in a single event; however, on average, this number is considerably lower. A preliminary observation reveals that the mean hit numbers are consistently lower than the values documented in the measurements, falling within the percent range. One theoretical explanation for this phenomenon is that the PMT threshold in the simulations was set to a low value. Furthermore, the measurements demonstrate that a significantly lower level of light is recorded when the opaque LS is implemented. The opposit was observed during the measurements. This finding suggests the possibility of erroneous assumptions regarding the values of absorption and scattering length, potentially resulting in an underestimation of the capabilities of opaque LS or an

overestimation of those of transparent LS. Furthermore, it is evident from the simulation that the paint thicknesses applied have a negligible effect. Recalling the spectral overlaps between the emission of the LS cocktails and the absorbance inside the WLS-paint layer at different thicknesses this is not surprising. This further elucidates by the observation that light is detected over the Bis-MSB with noticeably greater frequency than over the BPEA OWLs.

In transparent LS one can note a dependence on the fibre position. The second SiPM detects a greater quantity of light than the first one. This effect is not visible in the opaque LS. The discrepancy may be attributable to the phenomenon of directed Cherenkov light, which possesses the capacity to maintain its directionality in transparent media but not in opaque LS.

Another object of study in this simulation was the illumination of the SiPMs, as the question arose as to whether extend smaller SiPMs were capable of capturing the same amount of light. It is important to note that, due to the minute air gaps between the fibre end and the SiPM and potentially shallow excess angles of the photons, these photons may extend over a more substantial cross-sectional area than that of the fibre itself.
In the course of these simulations, an overestimated air gap of 0.5 mm was implemented. The plots in table 6.2 demonstrate the illuminations that have been accumulated over the entirety of the simulation data. The rectangular diagram illustrates the detection area of a 3 mm $\times$ 3 mm SiPM. In all cases, a 3 $\times$ 3 SiPM would have been adequate. Furthermore, there is evidence of some accumulation of hits in two locations along the x = 0 axis. The present axis corresponds to the line along which the gamma-rays are directed.

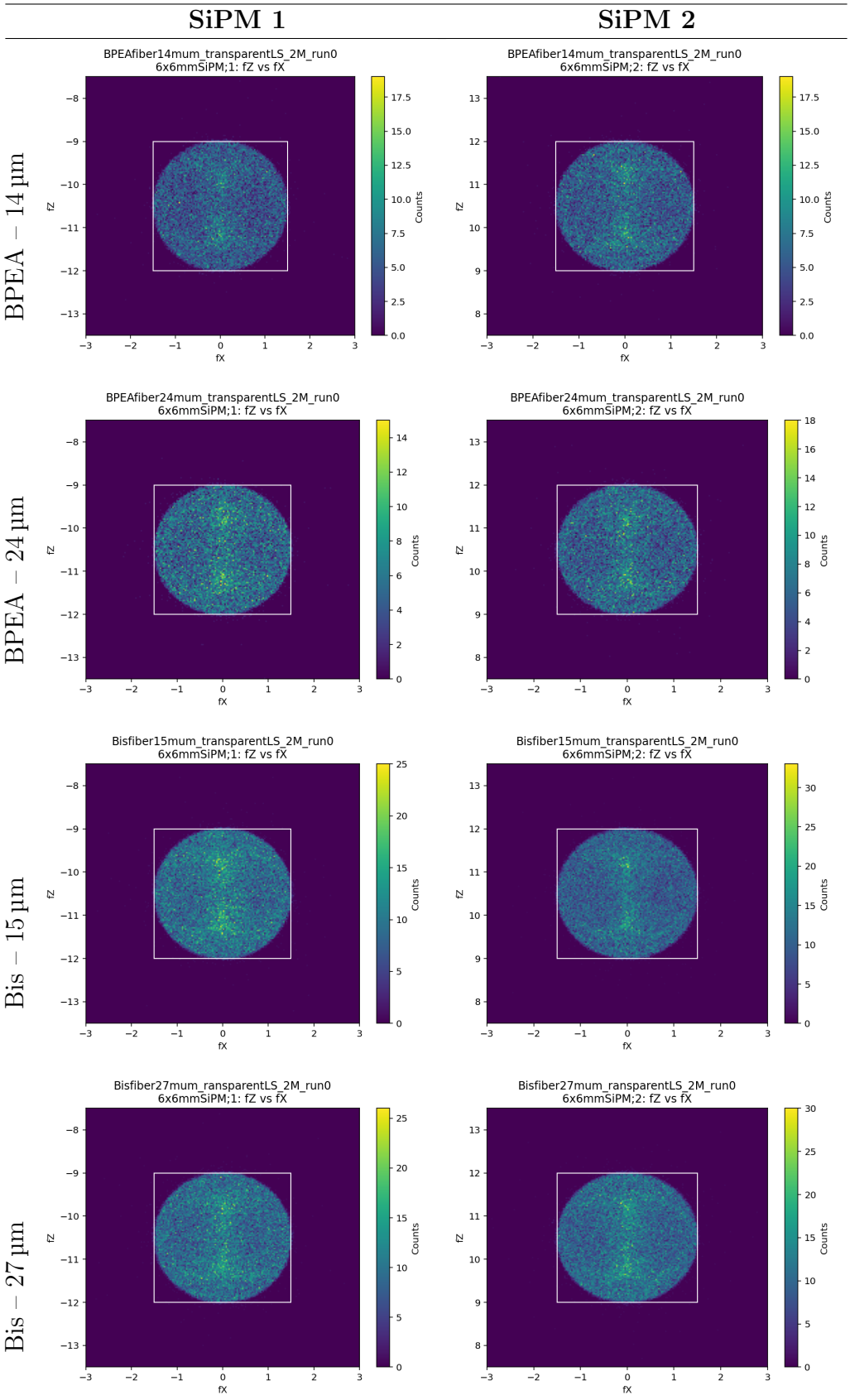

Table 6.2: Simulated SiPM illumination for Bis-MSB and BPEA-fibres with different coating thicknesses in transparent LS. 2 million gamma events were used.

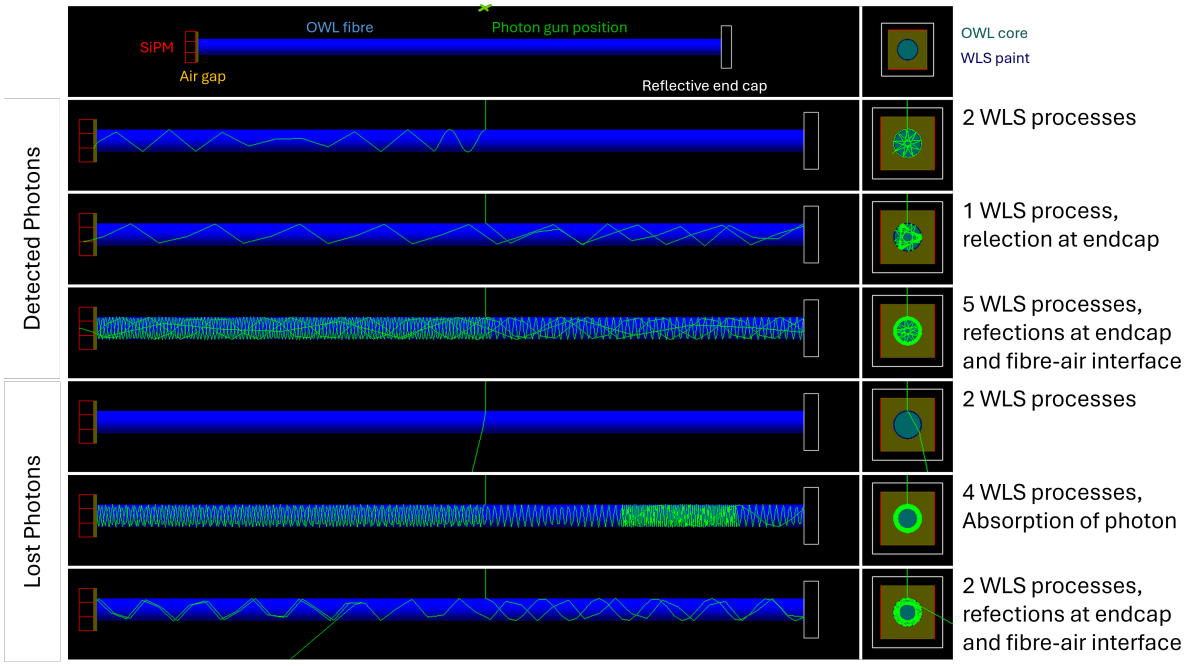

Figure 6.3: Display of various photon tracks inside a OWL made from a Polystyrene core, cladded with 20 μm Bis-MSB paint on PMMA basis. The left picture shows the side view of the fibre, the left the "bottom" view.

6.2 OWL Simulation

The objective of the OWL simulation was to ascertain the influence of different materials on detection performance. The construction of OWLs from diverse combinations of core and paint matrix material was the subject of a series of simulations. It has been established that all OWL cores had a diameter of 3 mm. The application of the paint was conducted in thicknesses ranging from 1 μm to 40 μm. The following points of interest were identified: the SiPM hit rate, the number of WLS re-absorptions, and the frequency of TIR.

The simulation comprised an OWL with a length of 10 cm suspended in air. The core materials utilised in the construction of the OWLs were quartz, PMMA and polystyrene. Paints utilising PMMA and Polysteren as matrix material were implemented. It was determined that PEMA would not be included in this simulation, as its refractive index is comparable to that of PMMA, yielding insufficient new informations. The optical properties were assumed to be flat over the entire optical range. The values of the properties entered into the material property tables of the materials can be viewed in table 6.3. The wavelength shifter employed in the paint was Bis-MSB. Like in the previously presented simulation, all surfaces were assumed to be perfectly polished and behave as dielectric–dielectric interface.

A PFTE sheet was affixed to one fibre extremity, thus forming a bottom cap. The surface of the PFTE sheet was designed to exhibit 100 % diffuse reflectivity. On the opposite fibre rare, a SiPM was positioned with an air gap of 0.5 mm. The air gap was deliberately set to this large value in order to encompass a worst-case scenario. The SiPM was divided into segments so that the detection of a 3 mm $\times$ 3 mm and a 6 mm $\times$ 6 mm SiPM could be simulated simultaneously. The OWL was exposed to photon with a wavelength of 340 nm, which depicts the peak absorption wavelength of Bis-MSB. It should be noted that the term "detected photon" in this context signifies that the SiPM has been struck

Material	Refractive Index	Absorption length
Polystyrene	1.61	3 m
PMMA	1.50	3 m
Quartz	1.46	10 m

Table 6.3: Values of the optical constance specified in the corresponding material property tables. The were assumed to be flat over the entire optical spectrum.

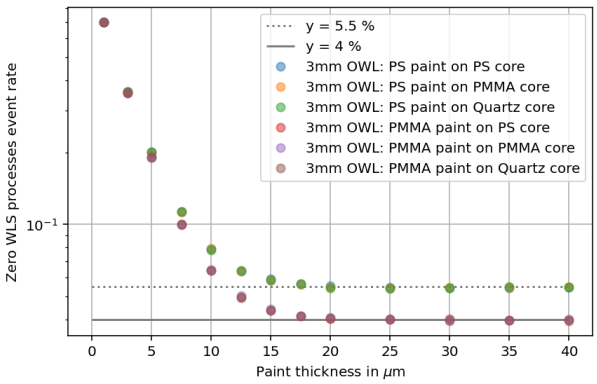

Figure 6.4: Display of the zero WLS process event rate per paint thicknesses for various OWLs.

by a photon. It is important to emphasise that this definition does not take into account the SiPM's detection efficiency.

Prior to delving into the discussion on the outcomes of the simulations, it would be beneficial to consider a series of exemplifications of photon tracks. Figure 6.3 shows different photon paths inside an OWLS with polystyrene core and PMMA paint. Displayed are events when at least one WLS process occured. The spiralling of the photons inside the fibre is clearly visible. WLS re-absorption is visible as change in the spiralling behaviour. The photons are reflected the the bottom cap and in some cases also at the top end, as TIR can also happen at this surface. The presence of several tens to hundreds of TIRs is not an uncommon occurrence.

The results of the simulations are shown in figures 6.4-6.7.
Figure 6.4 presents the rate of events in which the initial photon was not WLS absorbed. It is evident that the rate undergoes a substantial decline with an increase in paint thickness. Furthermore, it is notable that the rate begins to saturate at a paint thickness that exceeds 20 μm. The saturation value is contingent on the paint material and can be elucidated through the medium of Fresnel reflection. In accordance with the Fresnel formula for photon incidence normal to the surface, the reflectance R_0 is equivalent to

$$R = \left(\frac{n_1 - n_2}{n_1 - n_2} \right)^2 \tag{6.1}$$

when a photon travels from medium 1 to 2. In the case of an air - Polystyrene transition $R = 5.5\ \%$, while $R = 4\ \%$ for an transition from air to PMMA.

An inverse trend can be seen when looking at the event rate of SiPM hits, displayed in figure 6.5. Initially, the rate increases with paint thickness as more photons undergo WLS shifting and therefore have a chance of being captured. The 'detection' rate starts to de-

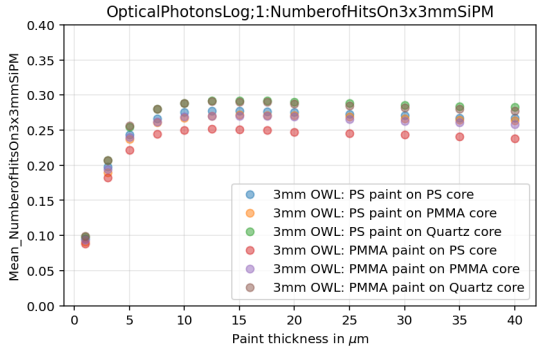

(a) 3 mm × 3 mm SiPM

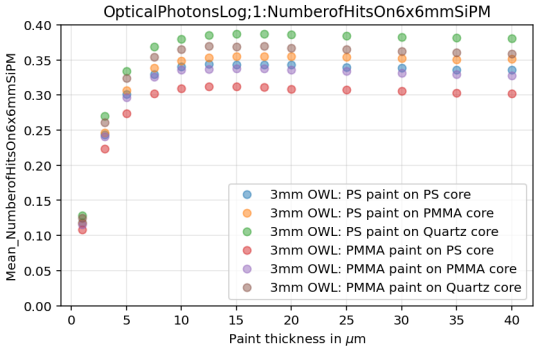

(b) 6 mm × 6 mm SiPM

Figure 6.5: "Detection" rates in terms of SiPM encounters per paint thickness for various OWLs.

crease slightly with paint thicknesses above 20 μm. Due to the thicker paint, longer parts of the photon path are spent in the paint, which increases the chance of re-absorption.
The overall trend is similar for all OWLs, but dependencies on the core and paint material are evident. Quartz core OWLs perform best. This is because quartz has the smallest difference in refractive index compared to air, meaning that fewer angles satisfy the TIR condition at the top end of the fibre. Consequently, more photons can exit the fibre and hit the SiPM. For the same reason, PMMA core OWLs perform better than polystyrene core OWLs. Filling the air gap with an optical pad or grease would therefore improve the 'detection' rate for all fibres.
The type of paint used also has an effect. Polystyrene paint outperforms PMMA paint. Furthermore, the larger SiPM is hit by more photons, the rate is increased about roughly 10 %. This result is surprising considering the illumination of the SiPMs presented in the previous simulation. Some photons exit the fibre at such wide angles that, over the range of the air gap between the fibre end and the SiPM, they miss the smaller SiPM. Setting the air gap to zero would solve this problem.

With the help of figures 6.6 an attempt is made to ascertain any discrepancies in terms of WLS process number between events in which the large SiPM was hit and those in which a photon was lost subsequent to at least one WLS process. The curves demonstrate a high degree of similarity in both cases. In general, the number of WLS processes increases in proportion to the thickness of the paint. It was found that, on average, a greater number of WLS processes occurred when the photon was detected at the end of the process.
The number of WLS processes is contingent on the core-paint material combination, and is closely related to the insights that figure 6.7 provides.
The frequency at which TIR occurs at the paint - air and paint - core interface is of object there. TIR at the paint - core interface is contingent upon the presence of a core that exhibits a lower refractive index in comparison to that of the paint. In such instances, photons can become trapped inside the paint. If the paint is very thin, several hundreds of TIR reflections follow one another. Due to the long path spent inside the paint, WLS re-absorption becomes more likely. It can thus be concluded that the colour order is consistent in figure 6.7 and figure 6.6.
Once more, it is evident that the magnitude of the disparity in refractive index directly

correlates with the intensity of the observed effect. However, it should be noted that the TIR number is already relatively high, in the order of a few hundred, in those fibres where trapping of photons is not feasible. This underscores the significance of surface quality.

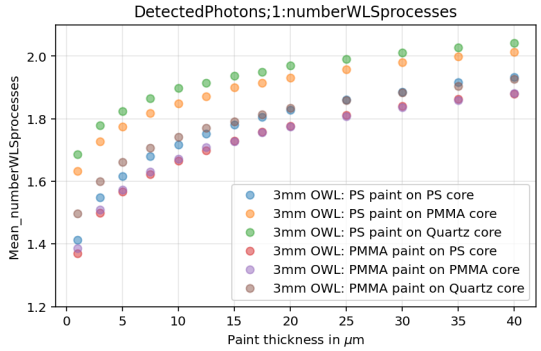

(a) Photons were "detected".

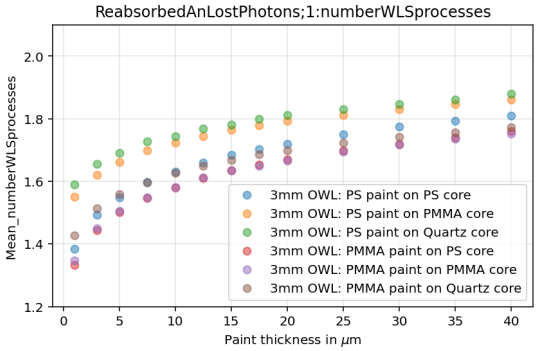

(b) Photons were lost.

Figure 6.6: Display of the mean number of WLS processes for different OWLs. On the left side, only events where a photon made it to the SIPM are displayed. On the left side, the events in which at least one WLS process occurred, but the photon was lost are displayed.

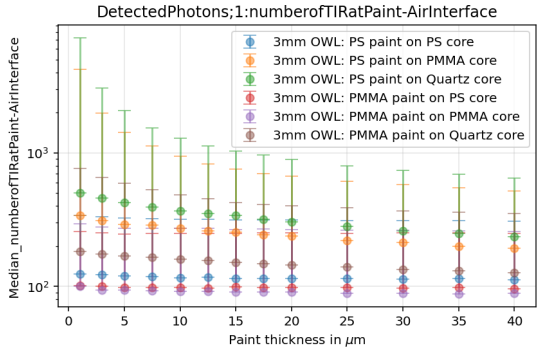

(a) TIR at the paint - air interface

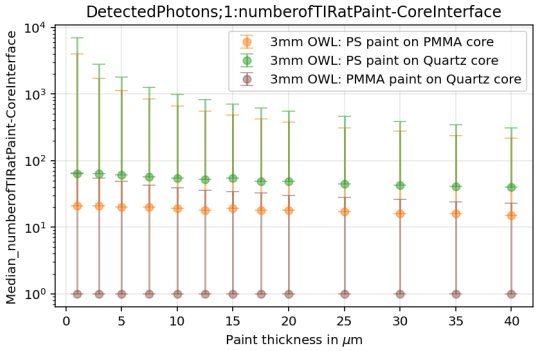

(b) TIR at the paint - core interface

Figure 6.7: Median of TIR at the paint - air (left) and paint - core(right) interface. The error bar shows the 75 % quantile of the data.

With regard to the detection rate, it appeares that an OWL composed of a quartz core and PS paint would demonstrate optimal performance. However, this configuration also exhibited the highest number of TIR. Achieving surfaces of such perfection, as those employed in the simulation, is a challenging prospect in reality. Consequently, the performance of fibre candidates may vary drastically when tested in reality. In order to achieve the optimum outcome, it would be advisable to select an arrangement in which the number of TIR processes is reduced. This can be accomplished by decreasing the refractive index or maintaining it at a constant value as one moves towards the exterior.
In consideration of the thickness of the paint, values between 10 μm to 20 μm appear to be optimal.

Chapter 7
Summary and Outlook

In summary, the present thesis details the implementation and use of a tabletop light yield setup for the purpose of performing relative comparison measurements. In view of unanticipated material issues pertaining to chemical stability in the scintillator LAB, the OWL fibres were advanced to Bubo fibres by enclosing the OWLs inside quartz tubes.
Relative comparison measurements were conducted in transparent and opaque LS cocktails.
The results of the study demonstrated that one Bubo prototype, the one containing a 3 mm quartz core OWL coated with a 27 μm thick layer of PEMA-based paint containing Bis-MSB, exhibited superior performance in comparison to the commercial Y11 fibres. Nevertheless, it is imperative to attribute this lead to a size benefit, as opposed to attributing it to a genuine advancement in capture efficiencies. Moreover, the results of the experimental trials on the Bubos revealed discrepancies. In order to resolve the aforementioned issues, it would be advantageous to produce and measure multiple Bubo prototypes of the same kind. This would facilitate the acquisition of more accurate statistics and, consequently, enable the formulation of statements of higher quality.

The implementation of sufficient triggering for the measurements in opaque LS proved to be a particularly challenging aspect of the study. Figure 7.1, a concept for an enhanced LS-fibre detector design is presented, which may offer a more optimal solution. The foundation of the LS volume is designed to be square in shape. The construction of the walls could be undertaken using an absorbing material. It is possible to mount four fibres in a symmetrical arrangement. The relocation of fibres away from the gamma's backscatter axis offers benefits. Primarily, it ensures that all back-scatter events must occur within the LS, thereby preventing energy deposition in the fibres of quartz tubes. The PMT is able to observe the LS via a window located at the base of the housing.
It is evident that the increased quantity of fibres in the sample results in a greater number of statistical results being obtained within the same amount of measuring time. Additionally, it is proposed that two fibres, designated as 1 and 3, could be utilised as triggering fibres when the volume is filled with opaque LS. Fibres with a documented high efficiency would be the optimal choice. The remaining two spaces can then be occupied by the fibres that will be the subject of measurement. Triggering of diagonal fibres in coincidence ensures that the gamma scatter took place in the middle of the sample.
Under circumstances where it is possible to ensure that there is a negligible gap between the fibre and the SiPM, the utilisation of SiPMs ranging over just the fibre diameter should be adequate. This objective could be accomplished through the attachment of a small spring to the interior of the Bubos end cap, thereby applying pressure to the OWL and exerting an upward force on the SiPM. This approach has been demonstrated by [38]. It is generally accepted that a reduction in the size of the SiPM typically results in a decrease in the number of pixels. This, in turn, leads to a reduction in noise, which consequently results in cleaner finger plots.
The simulations of the LS-fibre detector demonstrated a substantial discrepancy between the predicted and actual light outputs, indicating a significant divergence between the simulated and real measurements. The assumptions underlying the simulations must be

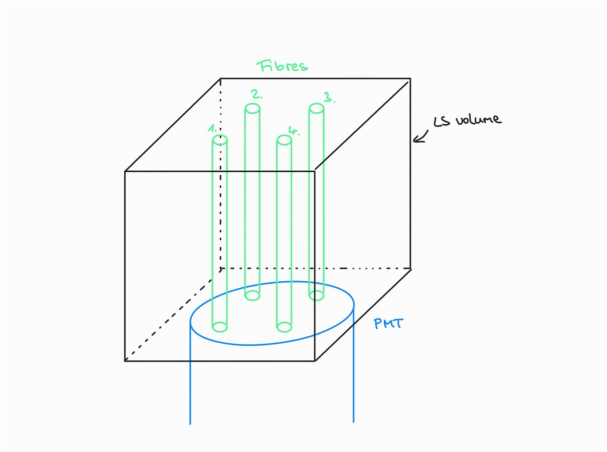

Figure 7.1: Idea for an improved LS-fibre detector. The hosing could again be made from PTFE. The housing has a square base. This volume will be filled with LS. A glass window is implemented as bottom, the PMT will be placed below the housing, facing the LS through the window. Four Fibres can be placed in a symmetric arrangement.

re-examined and recalibrated.
Another simulation investigated OWLs composed of different materials. The findings of this simulation suggest that utilising a low refracting core material, such as quartz, in conjunction with a high refracting paint material, for example polystyrene, is optimal for achieving the desired outcomes. The superiority of this combination is attributable to the fact that, at the fibre ends, TIR can also prohibit the photons from leaving the fibre. As the majority of photons spiral along the fibre, they strike the fibre end at a shallow angle. A decrease in the discrepancy between refractive indices results in a reduction of the tolerable TIR angle, which is actually beneficial on the end of the fibres. It is evident that fibre composed of PS paint and core, which is at the forefront of TIR capture rate on the lateral fibre side, fall behind. Perhaps a concave cut at the end of the fibre could solve this problem.
In addition, the results of the simulation suggest that OWL paint thicknesses ranging between 10 to 20 μm may be optimal.

In the simulation, the assumption was made that perfectly polished interface surfaces would be present. This is a theoretical representation of a perfect scenario. However, the Bubos demonstrated superior performance in actual experiments, which suggests that superficial imperfections, particularly at the fibre ends, may in fact be advantageous. The surface quality of the OWLs should be the focus of further studies.
The synthesis of a further batch of BPEA-30 paint, comprising higher concentrations of BPEA, might be of interest in order to achieve 100 % absorption over the entire BPEA excitation spectra. Furthermore, an additional second cladding layer of low refractive (with respect to the WLS paint material), non-WLS material could be applied in a similar thickness to the WLS paint layer. For instance, the fluorinated polymer utilised as a secondary cladding material in the Y11 fibres would be a suitable option. The establishment of two TIR-capable interfaces has the potential to enhance TIR capture efficiency.

The testing of tubes, manufactured from PMMA instead of PMMA, is a further potential avenue for exploration.

In order to study the influence of the protective tube on the detection efficiency of the OWLs, one could attempt to perform measurements in water-based LS. The OWLs are not anticipated to be adversely affected by the water-based scintillator. Therefore, it is possible to execute measurement runs with Bubos and OWLs put directly into the LS. Given that the refractive index of water is lower than that of LAB, it can be hypothesised that the capture rates will increase. It may become more apparent how the varying fibre performances differ from one another.

Bibliography

[1] M. Böhles et al., "Combining hybrid and opaque scintillator techniques in the search for double beta plus decays: A concept study for the experiment," *The European Physical Journal C*, vol. 85, no. 2, 2025.

[2] F. T. Avignone, S. R. Elliott, and J. Engel, "Double beta decay, majorana neutrinos, and neutrino mass," *Rev. Mod. Phys.*, vol. 80, pp. 481–516, 2008.

[3] M. J. Dolinski, A. W. Poon, and W. Rodejohann, "Neutrinoless double-beta decay: Status and prospects," *Annual Review of Nuclear and Particle Science*, vol. 69, no. Volume 69, 2019, pp. 219–251, 2019.

[4] J. D. Vergados, H. Ejiri, and F. Šimkovic, "Neutrinoless double beta decay and neutrino mass," *International Journal of Modern Physics E*, vol. 25, no. 11, p. 1630007, 2016.

[5] H. T. J. Steiger et al., "Development of a bi-solvent liquid scintillator with slow light emission," *Journal of Instrumentation*, vol. 19, p. P09015, 2024.

[6] J. Caravaca, F. B. Descamps, B. J. Land, M. Yeh, and G. D. OrebiGann, "Cherenkov and scintillation light separation in organic liquid scintillators," *The European Physical Journal C*, vol. 77, no. 12, 2017.

[7] LiquidO Consortium, "Neutrino physics with an opaque detector," *Communications Physics*, vol. 4, 2021.

[8] G. F. Knoll, *Radiation detection and measurement*.
John Wiley and Sons, 1979.

[9] S. Schoppmann, "Review of novel approaches to organic liquid scintillators in neutrino physics," *Symmetry*, vol. 15, no. 1, 2023.

[10] J. Birks, *The Theory and Practice of Scintillation Counting*.
Pergamon Press, 1964.

[11] P. Bougert, *Essai d'optique, sur la gradation de la lumiére*.
1729.

[12] H. Wollersheim (GSI), "Scintillation detectors." https://web-docs.gsi.de/~wolle/TELEKOLLEG/KERN/LECTURE/Wollersheim/2020/93-Scintillation-Detector.pdf.
Accessed: 21.11.24.

[13] CHIM, "The hybridization of orbitals." http://www.chim.lu/ech1002.php.
Accessed: 21.11.24.

[14] S. Gupta and Y. Mao, *Nano Scintillator-Book*.
2020.

[15] C. Buck and M. Yeh, "Metal-loaded organic scintillators for neutrino physics," *Journal of Physics G: Nuclear and Particle Physics*, vol. 43, no. 9, p. 093001, 2016.

[16] Wikipedia, "Cherenkov radiation." https://en.wikipedia.org/wiki/Cherenkov_radiation.
Accessed: 20.11.24.

[17] C. Buck, B. Gramlich, and S. Schoppmann, "Novel opaque scintillator for neutrino detection," *Journal of Instrumentation*, vol. 14, no. 11, 2019.

[18] M. Eisenhuth, "Development of an overpressure test cell and sensitivity study for double beta experiments," Master's thesis, Johannes Gutenberg-University Mainz, 2024.

[19] Hamamatsu Photonics K.K., "Pmt handbook, version 4." https://www.hamamatsu.com/content/dam/hamamatsu-photonics/sites/documents/99_SALES_LIBRARY/etd/PMT_handbook_v4E.pdf.
Accessed: 13.11.24.

[20] A. Ghassemi, K. Sato, and K. Kobayashi, "MPPC - technical guide to silicon photomultipliers (MPPC)," tech. rep., Hamamatsu Photonics K.K., 2022.

[21] B. Lubsandorzhiev, "On the history of photomultiplier tube invention," *Nuclear Instruments and Methods in Physics Research Section A: Accelerators, Spectrometers, Detectors and Associated Equipment*, vol. 567, no. 1, pp. 236–238, 2006.

[22] W. Demtröder, *Experimentalphysik 2 , Elektrizität und Optik*.
Springer - Verlag, 2017.

[23] Mini-Physics, "Total internal reflection." https://www.miniphysics.com/total-internal-reflection-2.html.
Accessed: 19.12.24.

[24] P. Rebourgeard et al., "Fabrication and measurements of plastic scintillating fibers," *Nuclear Instruments and Methods in Physics Research Section A: Accelerators, Spectrometers, Detectors and Associated Equipment*, vol. 427, no. 3, pp. 543–567, 1999.

[25] B. Bastian-Querner et al., "The wavelength-shifting optical module," *Sensors*, vol. 22, no. 4, 2022.

[26] B. Keßler, "Development of wavelength-shifting fiber with high photon capture-rate," Master's thesis, Johannes Gutenberg-University Mainz, 2024.

[27] "Interaction of gamma radiation with matter." https://www.nuclear-power.com/nuclear-power/reactor-physics/interaction-radiation-matter/interaction-gamma-radiation-matter.
Accessed: 20.11.24.

[28] HyperPhysics, "Cobalt-60 decay." http://www.hyperphysics.phy-astr.gsu.edu/hbase/Nuclear/betaex.html.
Accessed: 06.12.24.

[29] A. Bonhomme, C. Buck, B. Gramlich, and M. Raab, "Safe liquid scintillators for large scale detectors," *Journal of Instrumentation*, vol. 17, p. P11025, 2022.

[30] B. Keßler, "Discussion about the materials present in the wls paints.." Personal communication.
January 5, 2026.

[31] "Refractive index database." https://refractiveindex.info/?shelf=main&book=SiO2&page=Malitson.
Accessed: 07.12.24.

[32] H. Z. et all, "Refractive index in the juno liquid scintillator," *Nuclear Instruments and Methods in Physics Research Section A: Accelerators, Spectrometers, Detectors and Associated Equipment*, vol. 1068, p. 169730, 2024.

[33] A. Bonhomme, C. Buck, B. Gramlich, and M. Raab, "Safe liquid scintillators for large scale detectors," *Journal of Instrumentation*, vol. 17, no. 11, 2022.

[34] Kuraray, "Y11 data sheet." http://kuraraypsf.jp/pdf/all.pdf.
Accessed: 13.11.24.

[35] B. Keßler, "Attenuation measurements of WLS paints bpea-30 and p64." Personal transfer.

[36] Hamamatsu, "Sipm s12260-6050ve data sheet." https://www.hamamatsu.com/content/dam/hamamatsu-photonics/sites/documents/99_SALES_LIBRARY/ssd/s13360-2050ve_etc_kapd1053e.pdf.
Accessed: 21.11.24.

[37] S. Vinogradov, "Analytical models of probability distribution and excess noise factor of solid state photomultiplier signals with crosstalk," *Nuclear Instruments and Methods in Physics Research Section A: Accelerators, Spectrometers, Detectors and Associated Equipment*, vol. 695, pp. 247–251, 2012.

[38] J. Pätschke, "Development of a prototype opaque liquid scintillator for use in the darkMESA experiment," Master's thesis, Johannes Gutenberg-University Mainz, about to be pubished in February 2026.

[39] "Photonis pmt xp2020 data sheet." https://datasheet4u.com/pdf-down/X/P/2/XP2020_Photonis.pdf.
Accessed: 14.11.24.

[40] D. Zundel, "Event reconstruction in cherenkov-scintillation detectors," Master's thesis, Johannes Gutenberg-University Mainz, 2025.

Appendix A

Technical Drawings to the Proof Of Concept Detector

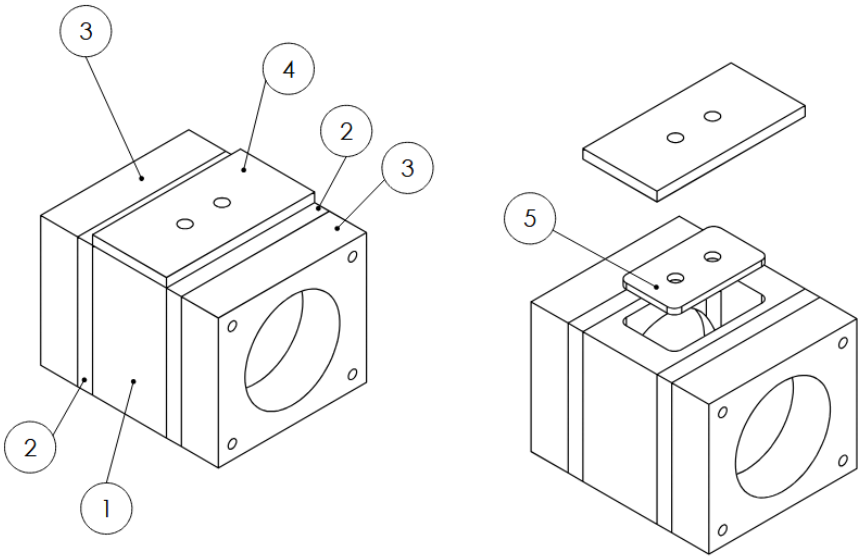

Figure A.1: Technical drawing of the PFTE cavity used in the proof of concept detector. Core piece is the middle piece (1) made from PTFE. The outer dimensions 40 mm x 80 mm x 70 mm. The inner cavity that can be filled with LS measures 30 mm x 51.2 mm x 63.6 mm. The middle piece has a 2" hole centred on either side face. Those side faces are closed of by 8mm thick acrylic glass windows(2). The windows have a notch in which a sealing ring is located to tightly seal the 2" hole. The acrylic glass sheet, is on both sides, followed by a PFTE sheet with again a 2" hole (3). A bottom sheet (5) of 30 mm x 52.2 mm x 2 mm PFTE can be placed into the middle piece. A PTFE lid (4) closes of the middle piece. Bottom sheets and lids with different diameter holes exist. The individual parts are threaded through the holes at each corner in the order shown onto threaded rods and secured with wing nuts on each side.

The key piece of this setup is a small PTFE cavity that can be filled with LS. The technical drawing of this cavity can be found in Figure A.1. This piece will be referred to as LS sample. The lid of the cavity has two holes through that 2 fibres can be introduced into the sample. Exchangeable bottom plates are placed at the bottom of the cavity, as well with 2 holes to secure the fibres position in the LS. Lids and bottom plates with different diameter holes exist, to match the diameter of the used fibres. The PFTE cavity is closed of with plexiglas windows at 2 opposing sides. One window was sealed with Meiler foil to make this side reflective, a 2" PMT from HZC Photonics (XP2020 serieres) is looking into the LS volume from the outer side. The PMT was operated at a voltage of 1800V (negative polarity).

Figure 4.4 gives an example of how the sample looks from the PMTs' side. A 3D-printed structure holds the SiPM board and it can be clipped on top of the lid. The fibres that enter the cavity through the lid holes are fixed to the board as well such that the fibre ends each face a 6mmx6mm SiPMs (Hamamatsu, S13360-6050VE).

Appendix B

Hardware Details and Characterisations

This section is dedicated to the calibrations of the used PMT as well as the SiPMs.

B.1 PMT

The PMT used is from the XP2020 serieres produced by HZC Photonis. It contains a 2 inch round tube with 12 dynode stages that are arranged in linearly focused. The entrance window is made of Borosilicate glass with a reflective index of 1.48 (at 420nm), the photo cathode is made from Bi-alkali metals. The spectral range opens from 270-650 nm with a maximum sensitivity at 420. PMTs from this line feature good linearity within the range of 1800V to 2500V, very low background noise, excellent time characteristics and a good single electron spectrum. The data sheet of this PMT can be found in [39].

The PMT was generously borrowed from Dorina Zundel and also characterised by her before hand as follows. A more detailed description of the characterisation procedure and setup can be found in chapter 3.2 of [40]. Here a brief summary will be presented:

To find the single photon equivalent (SPE) response of the PMT, a picosecond pulsed diode laser (PiLas NPIL1-040-40FC, $\lambda = 405$ nm) was used. Inside an aluminium dark box, the laser was placed some distance away pointing towards the PMT. The laser pulser was operated on low intensities and in addition a filter was placed in front to diffuse the few photons per pulse further. In that manner, it is possible detect single photon. The data acquisition was carried out as well with the Rhode & Schwarz Oscilloscope RTO64. The laser provides further a rectangular trigger pulse as signal output, that falls in coincidence with light emission. It was used as trigger. The PMT was operated at a voltage of 1800 V as in the proof of concept detector.

Figure B.1 shows the histogram of such a measurement. To the data a convolution a sum of five Gaussians was fitted. The fit function is given by

$$f(x) = \sum_{i=0}^{4} A_i \cdot exp(\frac{(\mu_i - x)^2}{2\sigma_i^2}). \tag{B.1}$$

The 0th Gauss represent noise triggers, the following represent the one, two, three and four photon peak components consequently.

Due to this calibration one can now use the linearity between counts of detected photons to signal response to determine how many photons have hit the PMT.

B.2 SiPMs

To determine the SiPM breakdown voltage, a laser pulser was placed a few cm in front of the SiPM. The bias voltage applied to the SiPM was gradually increased. The laser

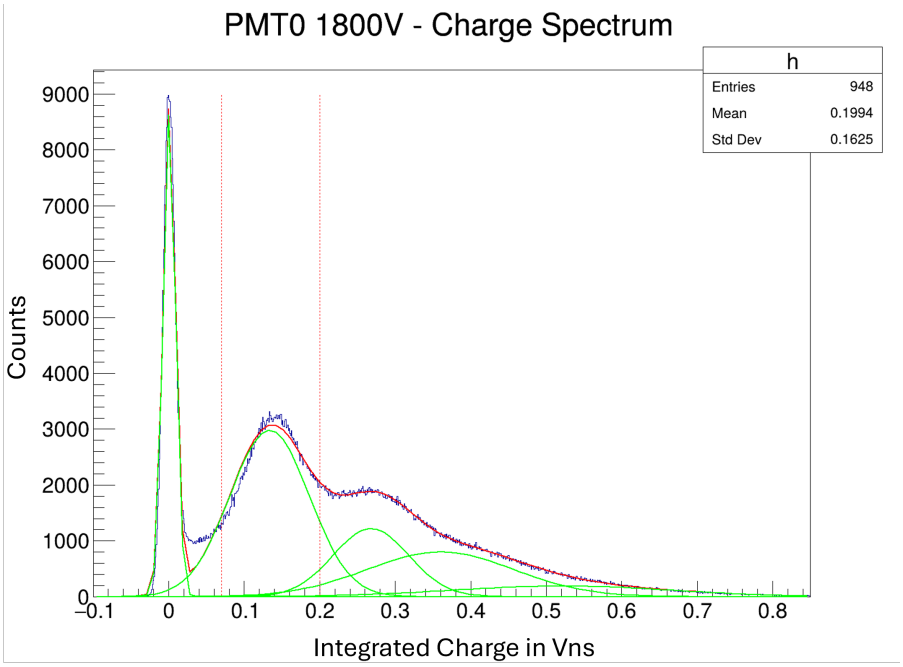

Figure B.1: Histogram of the Characterisation data and fit of Eq.B.1 in red. Further in green individual parts of the fit, i.e. the individual Gaussians, are shown. The fit parameters can be found in table B.1. Plot and fit were created by Dornia Zundel and are used with permission.

i	A_i	μ_i [Vns]	σ_i [vns]
0	8737.24±25.33	0.0011±0.0000	0.0083±0.0000
1	2978.57±9.52	0.1339±0.0003	0.0525±0.0001
2	1219.03±26.02	0.2682±0.0006	0.0499±0.0008
3	797.60±15.95	0.3601±0.0027	0.0972±0.0014
4	190.16±7.29	0.5209±0.0053	0.1429±0.0017

Table B.1: Fit values to the PMT characterisation data presented in Figure B.1. The fit function is Eq. B.1.

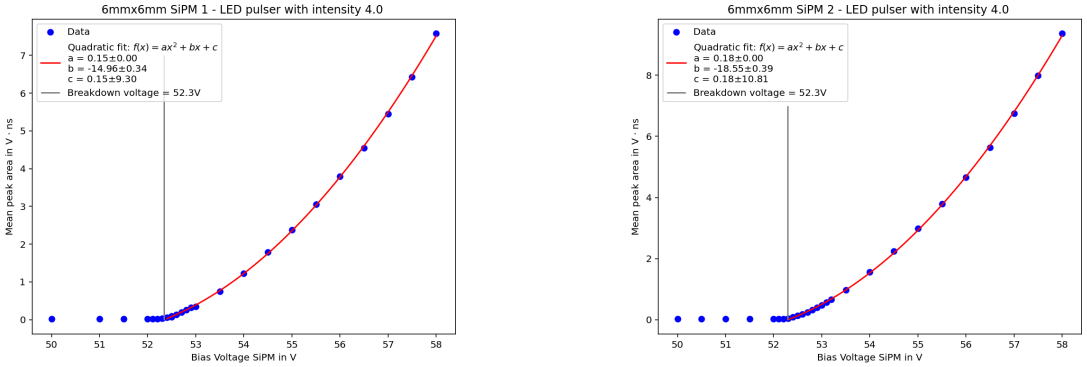

(a) SiPM 1

(b) SiPM 2

Figure B.2: Applied Bais-voltage vs mean peak area for both SiPMs. The vertical lines mark the breakdown voltage.

pulser signal was used to trigger the pulse shape recording. 50000 events were recorded per voltage. The mean peak area was calculated via integration over the pulse.
To evaluate the break-down voltage, the bias-voltage was plotted against the mean peak area. The curves (see figure B.2) show a quadratic display above a certain value, the breakdown voltage. Calculating the zero crossing of the parabola yields the breakdown voltage. The determined break down voltage was 52.3 V for both SiPMs.

Appendix C

Measurement Plots

In the following subchapters, the plots used to evaluate the other measurements are displayed.

C.1 BPEA Bubos in Transparent LS

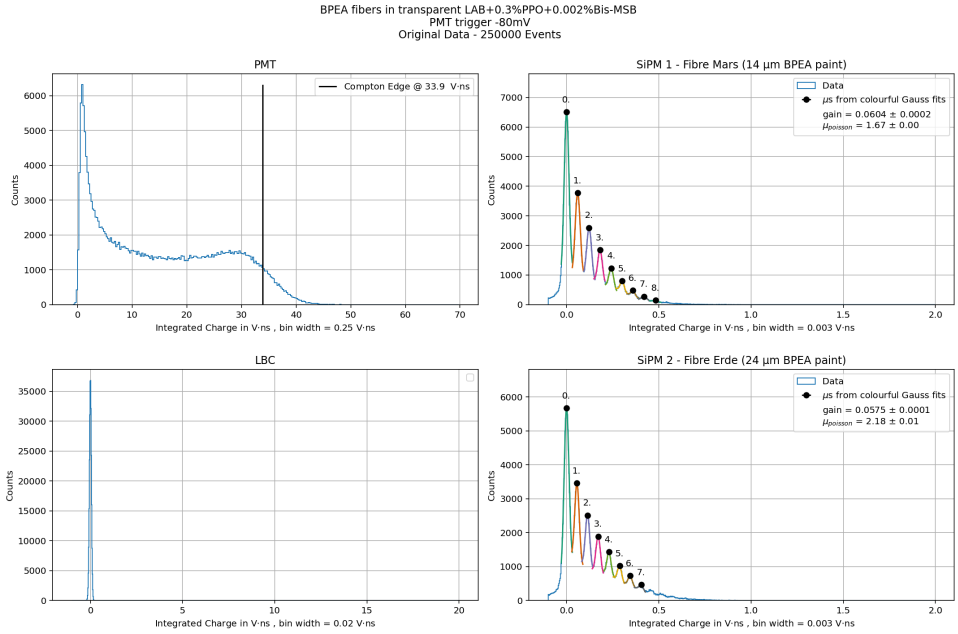

Figure C.1: Overview of the intergraded charge histograms obtained with the BPEA Bubos emersed in transparent LAB + 0.3 %PPO + 0.002 % Bis-MSB. The trigger was set to the PMT signal, the threshold was -80 mV.

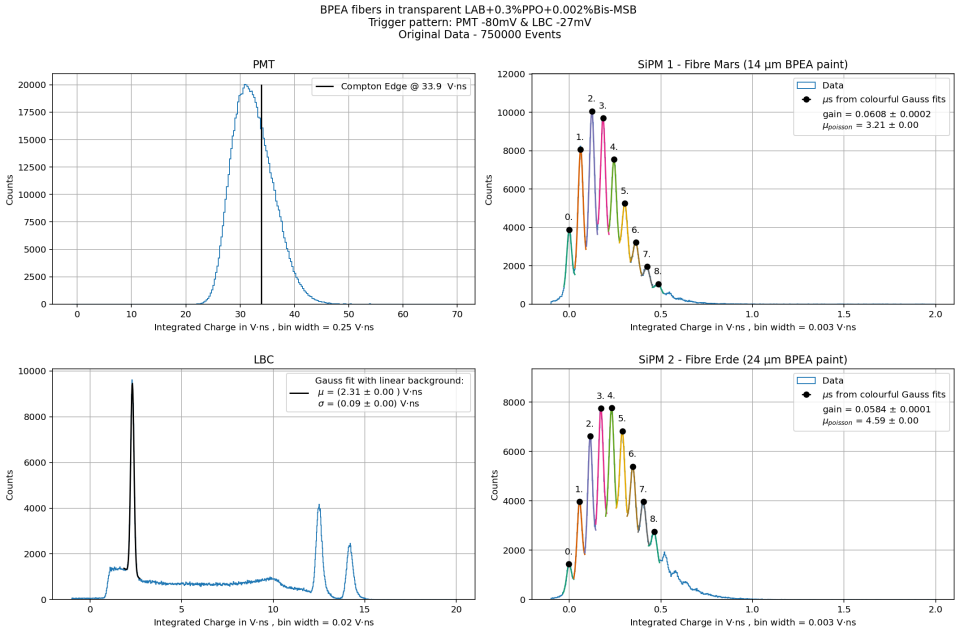

Figure C.2: Overview of the intergraded charge histograms obtained with the BPEA Bubos in transparent LAB + 0.3 %PPO + 0.002 % Bis-MSB. A trigger pattern looking for simultaneously excess of threshold of -2 V in the PMT signal and -27 mV in the LBC signal.

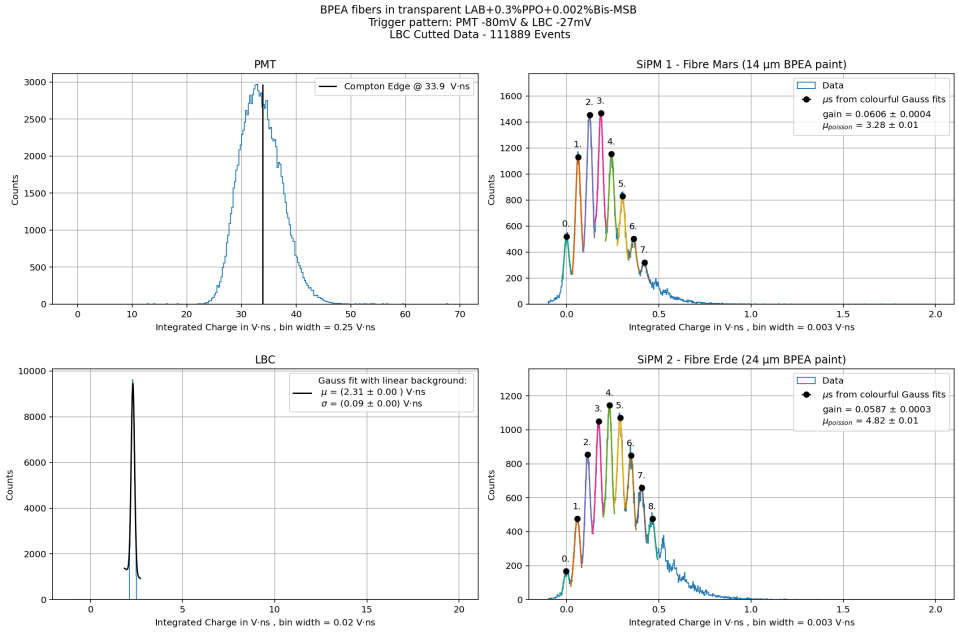

Figure C.3: Overview of the intergraded charge histograms obtained with the BPEA Bubos emersed in transparent LAB + 0.3 %PPO + 0.002 % Bis-MSB. A trigger pattern looking for simultaneously excess of threshold of -2 V in the PMT signal and -27 mV in the LBC signal. In addition an offline cut the the 2σ region of the Gauss fitted to the LBC backscatter peak was applied.

C.2 Y11 in Transparent LS

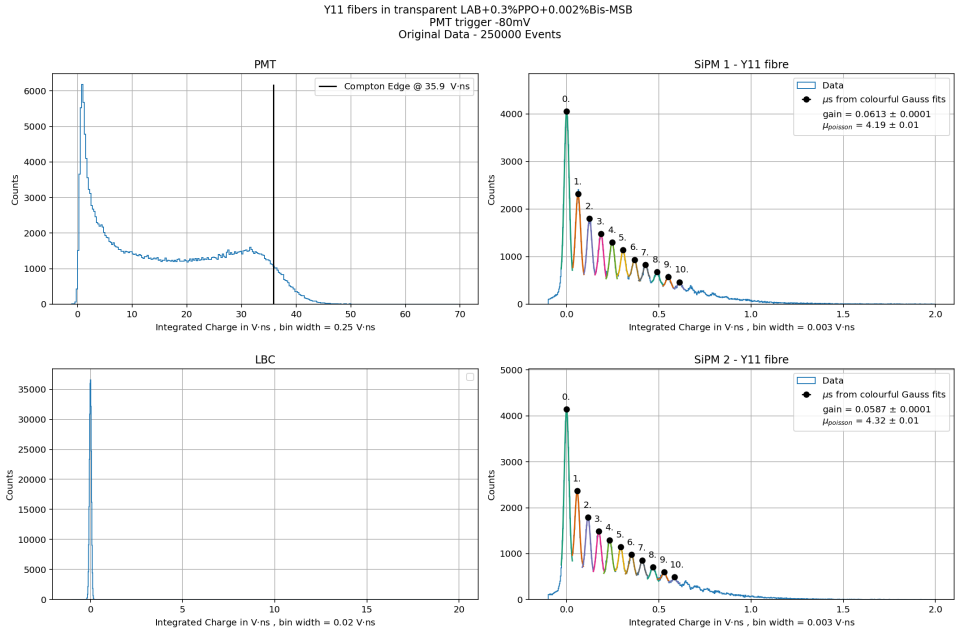

Figure C.4: Overview of the intergraded charge histograms obtained with the Y11 fibres emersed directly in transparent LAB + 0.3 %PPO + 0.002 % Bis-MSB. The trigger was set to the PMT signal, the threshold was -80 mV.

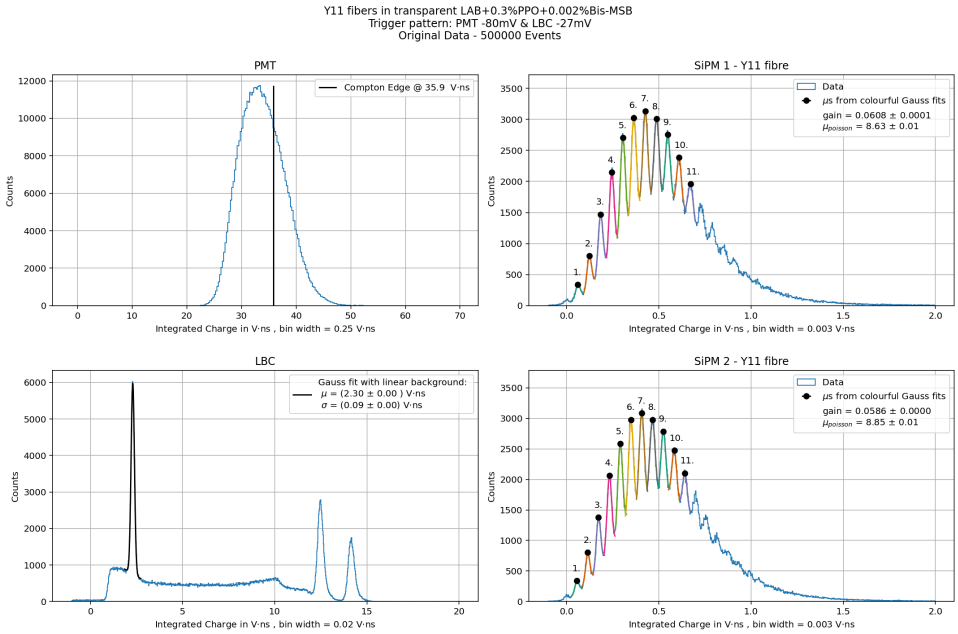

Figure C.5: Overview of the intergraded charge histograms obtained with the Y11 fibres emersed directly emersed in transparent LAB + 0.3 %PPO + 0.002 % Bis-MSB. A trigger pattern looking for simultaneously excess of threshold of -2 V in the PMT signal and -27 mV in the LBC signal.

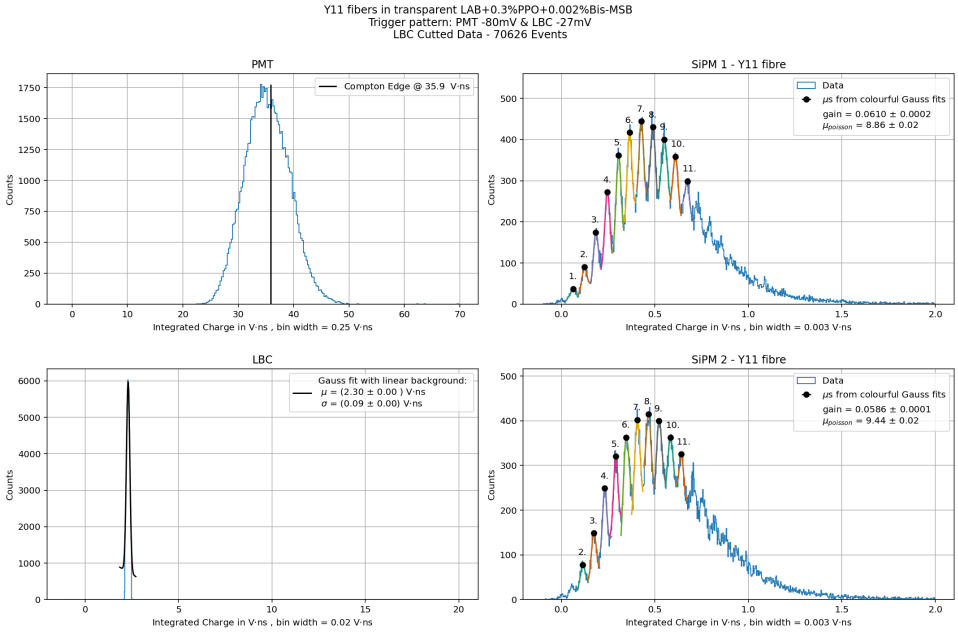

Figure C.6: Overview of the intergraded charge histograms obtained with the Y11 emersed in transparent LAB + 0.3 %PPO + 0.002 % Bis-MSB. A trigger pattern looking for simultaneously excess of threshold of -2 V in the PMT signal and -27 mV in the LBC signal. In addition an offline cut the the 2σ region of the Gauss fitted to the LBC backscatter peak was applied.

C.3 Quartz Tube Enclosed Y11 in Transparent LS

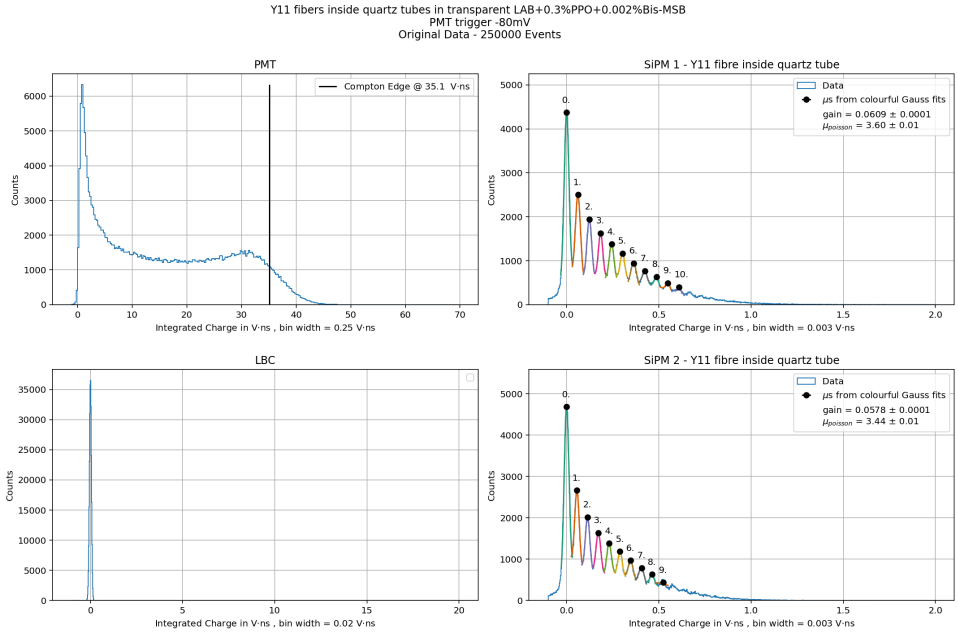

Figure C.7: Overview of the intergraded charge histograms obtained with the Y11 inside the quartz tube in transparent LAB + 0.3 %PPO + 0.002 % Bis-MSB. The trigger was set to the PMT signal, the threshold was -80 mV.

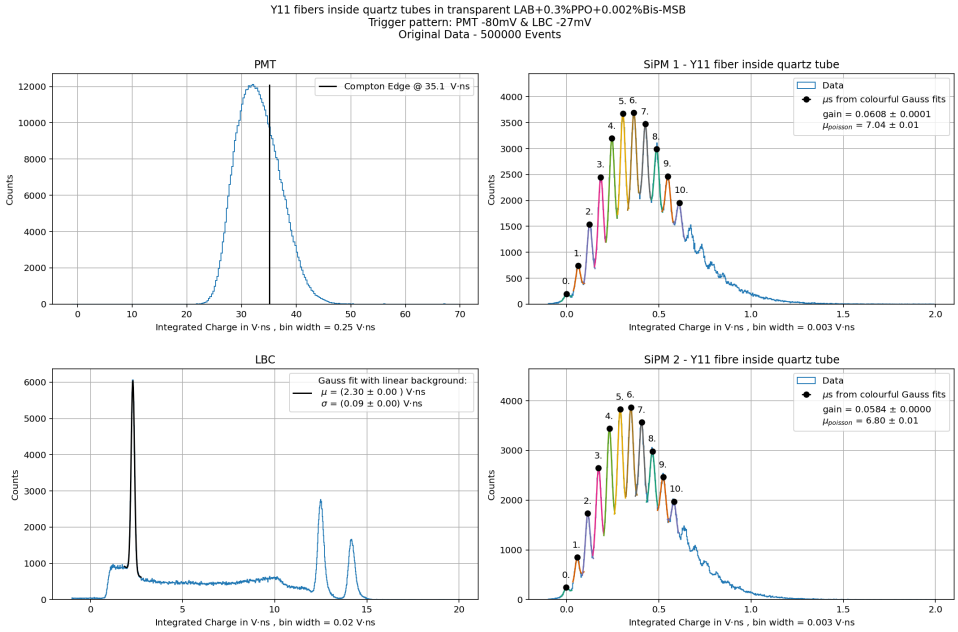

Figure C.8: Overview of the intergraded charge histograms obtained with the Y11 fibres inside the quartz tube in transparent LAB + 0.3 %PPO + 0.002 % Bis-MSB. A trigger pattern looking for simultaneously excess of threshold of -2 V in the PMT signal and -27 mV in the LBC signal.

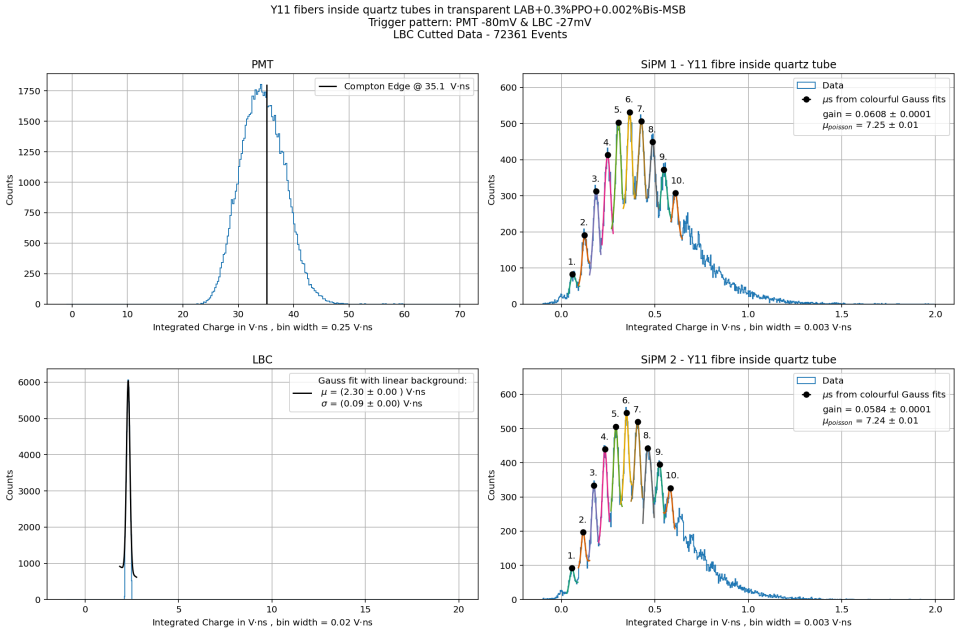

Figure C.9: Overview of the intergraded charge histograms obtained with the Y11 inside the quarzt tubes emersed in transparent LAB + 0.3 %PPO + 0.002 % Bis-MSB. A trigger pattern looking for simultaneously excess of threshold of -2 V in the PMT signal and -27 mV in the LBC signal. In addition an offline cut the the 2σ region of the Gauss fitted to the LBC backscatter peak was applied.

C.4 Bis-MSB Bubos in opaque LS

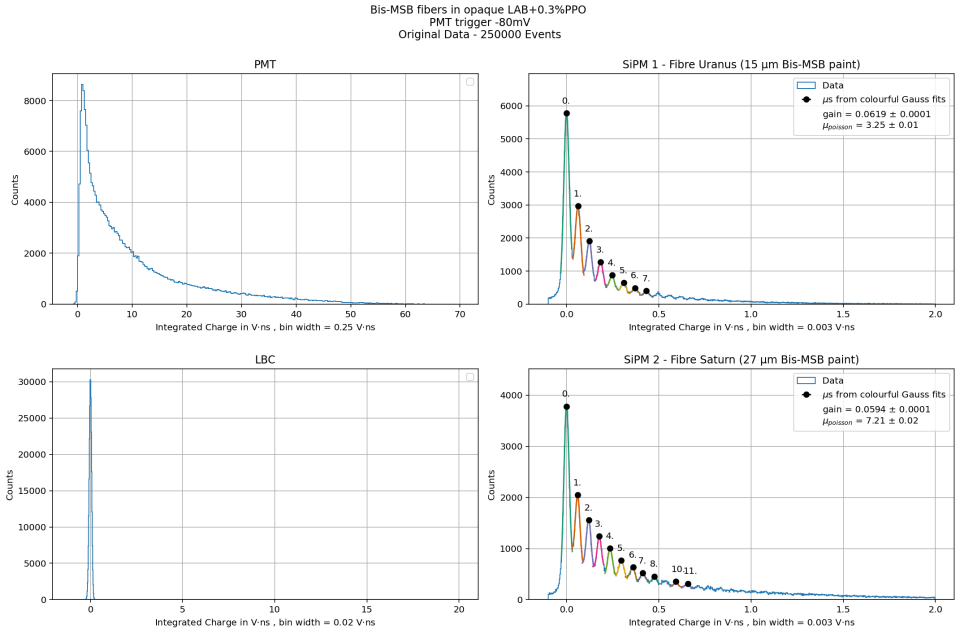

Figure C.10: Overview of the intergraded charge histograms obtained with the Bis-MSB Bubos emersed in opaque LAB + 0.3 %PPO. The trigger was set to the PMT signal, the threshold was -80 mV.

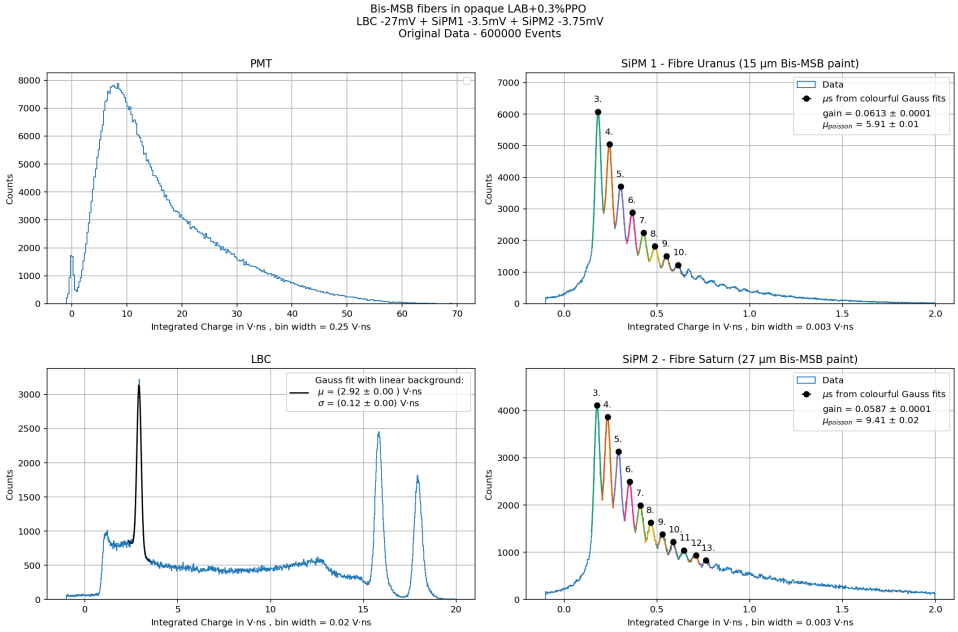

Figure C.11: Overview of the intergraded charge histograms obtained with the Bis-MSB Bubos emersed in opaque LAB + 0.3 %PPO. The trigger was set on a coincidence pattern, the thresholds for the channels were: LBC -27 mV, SiPM 1 -3.5 mV & SiPM 2. -3.75 mV.

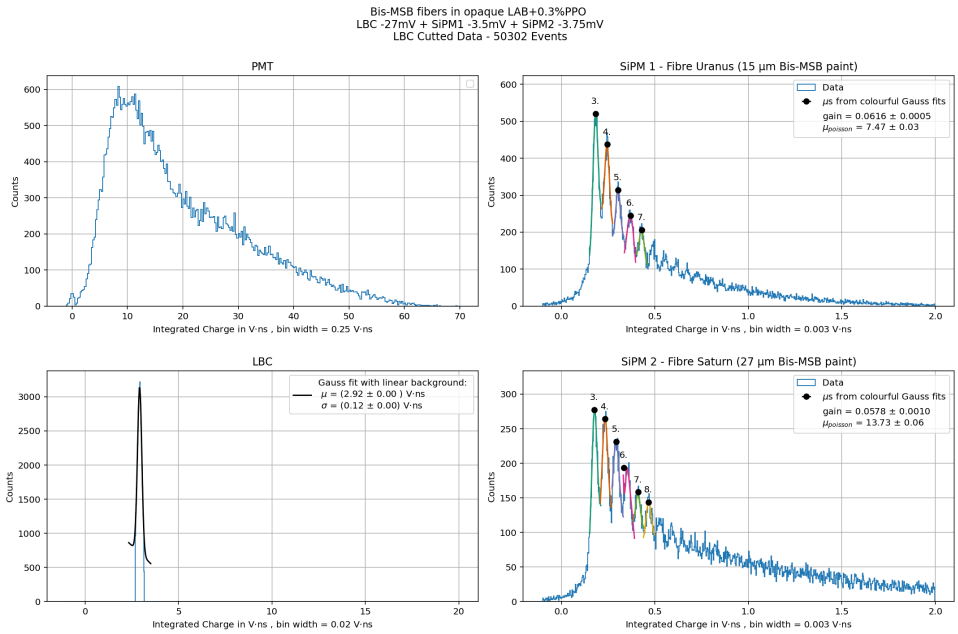

Figure C.12: Overview of the intergraded charge histograms obtained with the Bis-MSB Bubos emersed in opaque LAB + 0.3 %PPO. The trigger was set on a coincidence pattern, the thresholds for the channels were: LBC -27 mV, SiPM 1 -3.5 mV & SiPM 2. -3.75 mV. In addition a LBC backscatter cut was applied.

C.5 BPEA Bubos in opaque LS

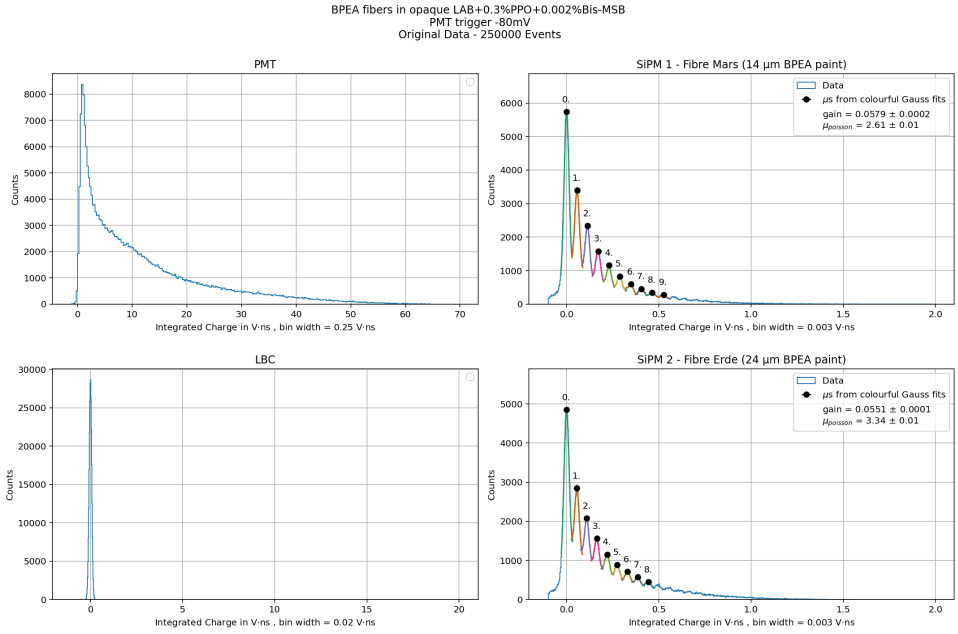

Figure C.13: Overview of the intergraded charge histograms obtained with the BPEA Bubos emersed in opaque LAB + 0.3 %PPO +0.002 % Bis-MSB. The trigger was set to the PMT signal, the threshold was -80 mV.

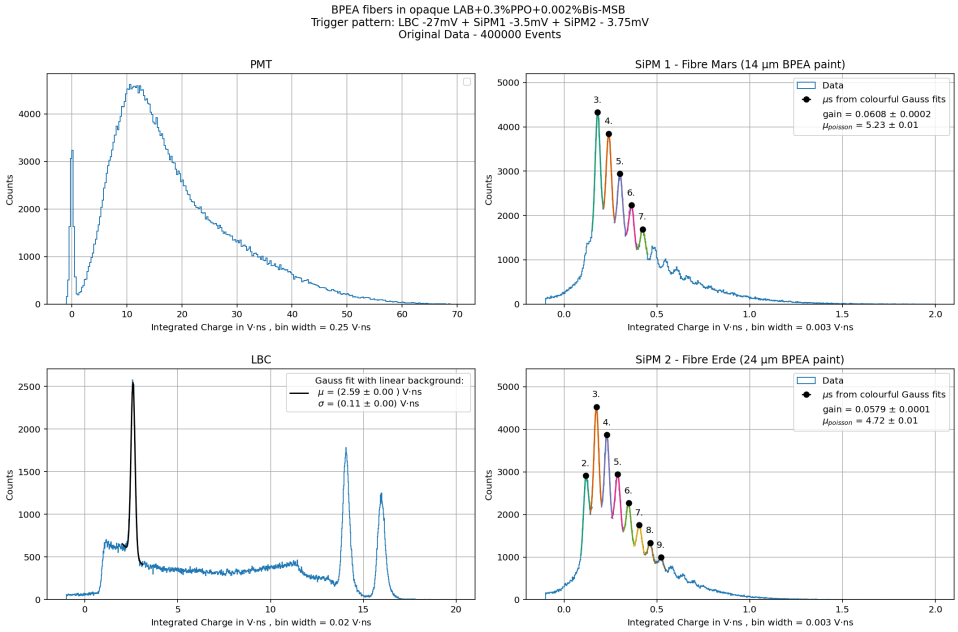

Figure C.14: Overview of the intergraded charge histograms obtained with the BPEA Bubos emersed in opaque LAB + 0.3 %PPO +0.002 % Bis-MSB. The trigger was set on a coincidence pattern, the thresholds for the channels were: LBC -27 mV, SiPM 1 -3.5 mV & SiPM 2. -3.75 mV.

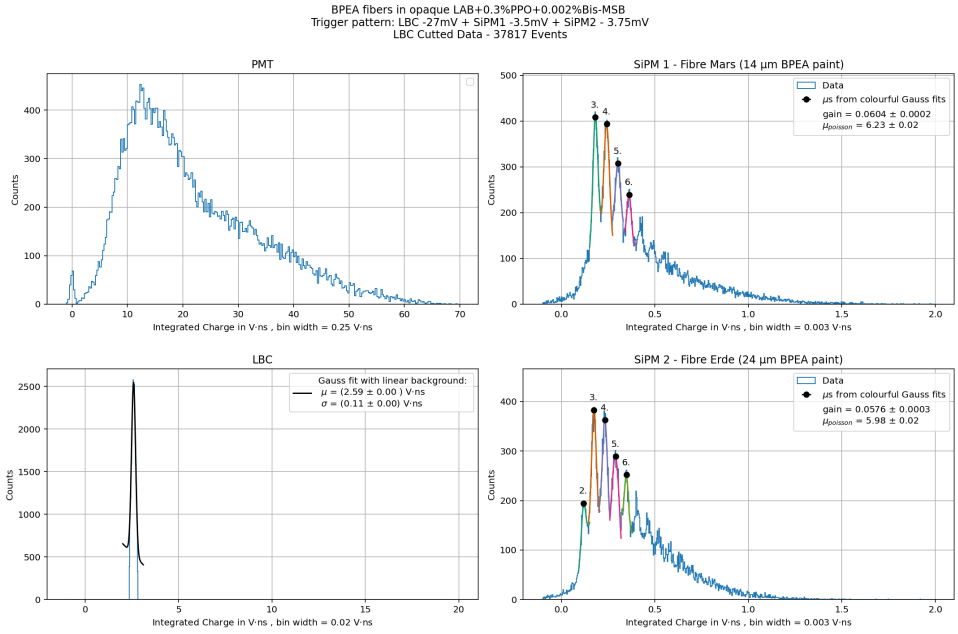

Figure C.15: Overview of the intergraded charge histograms obtained with the BPEA Bubos emersed in opaque LAB + 0.3 %PPO +0.002 % Bis-MSB. The trigger was set on a coincidence pattern, the thresholds for the channels were: LBC -27 mV, SiPM 1 -3.5 mV & SiPM 2. -3.75 mV. In addition a LBC backscatter cut was applied

C.6 Y11 fibre in opaque LS

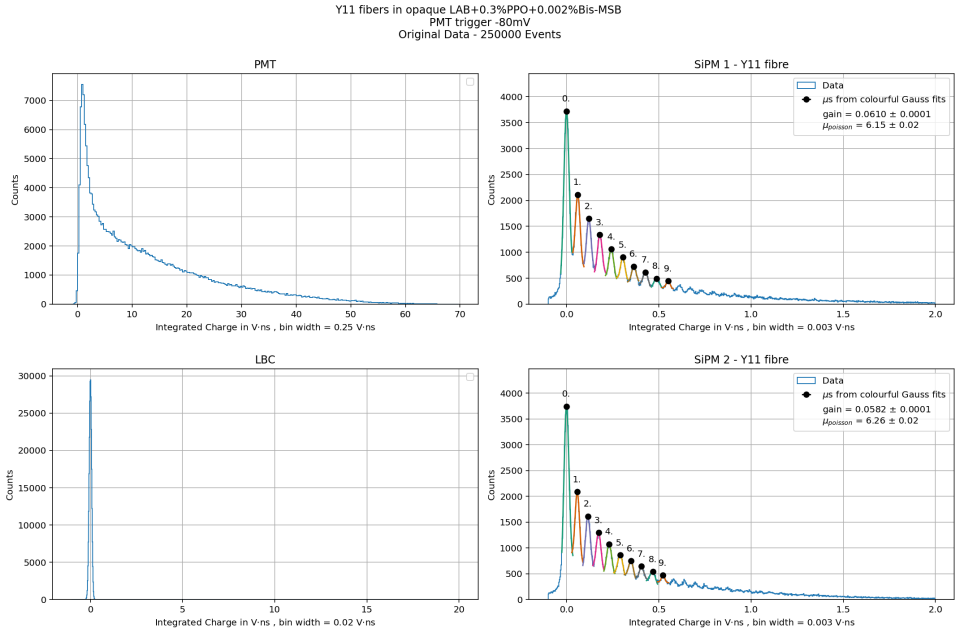

Figure C.16: Overview of the intergraded charge histograms obtained with the Y11 fibre emersed in opaque LAB + 0.3 %PPO +0.002 % Bis-MSB. The trigger was set to the PMT signal, the threshold was -80 mV.

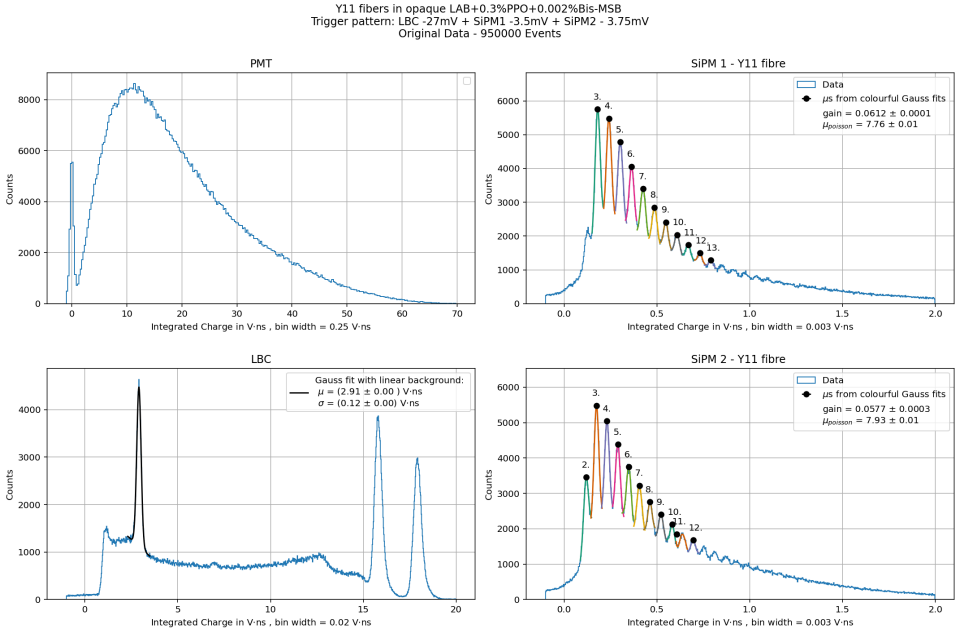

Figure C.17: Overview of the intergraded charge histograms obtained with the Y11 fibre emersed in opaque LAB + 0.3 %PPO +0.002 % Bis-MSB. The trigger was set on a coincidence pattern, the thresholds for the channels were: LBC -27 mV, SiPM 1 -3.5 mV & SiPM 2. -3.75 mV.

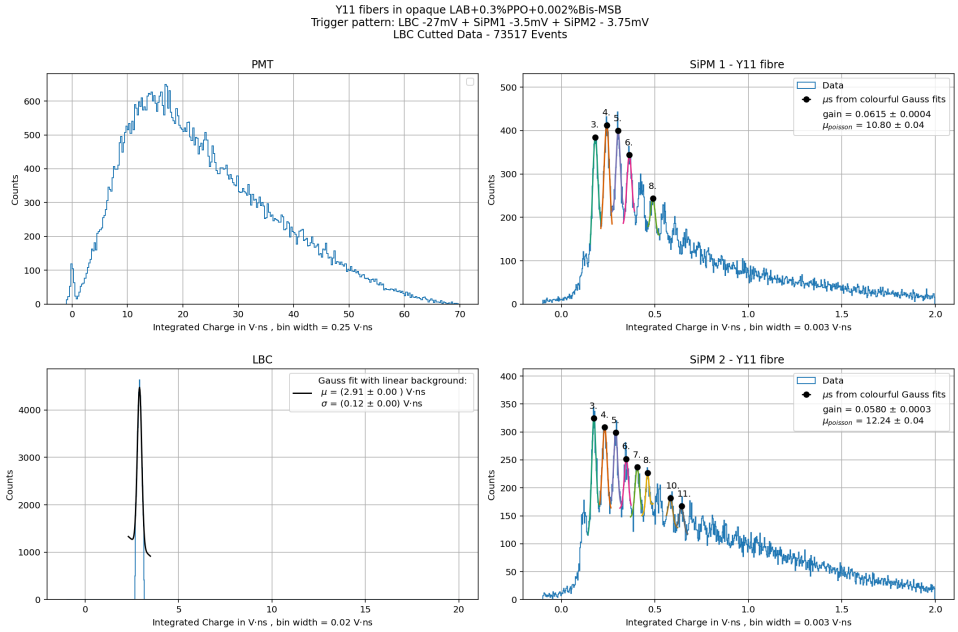

Figure C.18: Overview of the intergraded charge histograms obtained with the Y11 fibre emersed in opaque LAB + 0.3 %PPO +0.002 % Bis-MSB. The trigger was set on a coincidence pattern, the thresholds for the channels were: LBC -27 mV, SiPM 1 -3.5 mV & SiPM 2. -3.75 mV. In addition a LBC backscatter cut was applied